Fast neutron induced reactions leading to activation products: selected cases relevant to development of low activation materials, transmutation and hazard assessment of nuclear wastes

Inaugural-Dissertation

zur
Erlangung des Doktorgrades
der Mathematisch-Naturwissenschaftlichen Fakultät
der Universität zu Köln

vorgelegt von
Peter Reimer
aus Haselünne

Druckerei des Forschungszentrums Jülich GmbH
2002

Berichterstatter: Prof. Dr. Dr. h. c. S. M. Qaim
Prof. Dr. H. Ströher

Tag der mündlichen Prüfung: 5. Februar 2002

Die vorliegende Arbeit wurde in der Zeit von Februar 1998 bis Oktober 2001 am Institut für Nuklearchemie des Forschungszentrums Jülich GmbH und am Joint Research Centre (JRC), Institute for Reference Materials and Measurements (IRMM) in Geel, Belgien, unter Anleitung von Herrn Prof. Dr. Dr. h. c. S. M. Qaim (Abteilung für Nuklearchemie der Universität zu Köln) durchgeführt.

Abstract

Neutron induced cross sections are of interest for practical applications and for testing nuclear models. In this work (n,p), (n,np), (n,α), (n,nα), (n,n'γ), (n,2n) and (n,3n) reactions on vanadium, molybdenum, technetium and lead have been measured in the energy range of 0.5 to 20.6 MeV using the activation technique . The radioactive reaction products with half-lives between 58 seconds and 20300 years have been measured offline via high-resolution γ-ray-spectrometry and Liquid Scintillation Counting, the latter in combination with radiochemical separation.

Irradiations with neutron energies in the range of 0.5 to 6 MeV were done using the ^{3}H(p,n)^{3}He reaction with a solid-state Ti/T target while energies between 7.4 and 12.5 MeV were covered with the ^{2}H(d,n)^{3}He reaction utilizing a D_2 gas target. Irradiations in the energy range from 13.4 to 20.6 MeV were performed using the ^{3}H(d,n)^{4}He reaction, again with a solid Ti/T target. Most of the reactions were investigated using a light mass setup to minimise scattering effects, but for short half-lives a pneumatic sample transport system was used as well. A special sample holder was developed for the measurement of the $^{\mathrm{nat}}$Mo(n,x)^{94}Nb reaction.

All cross sections were measured relative to the ^{27}Al(n,α)^{24}Na standard cross section and all necesarry corrections due to the irradiation process and the measurement of the induced activity have been applied.

Nuclear model calculations were performed for all investigated reactions. For reactions on ^{99}Tc and Pb the original STAPRE code was used, while for reactions on V and Mo a modified version STAPRE-H was employed.

As a result of this thesis work an extended database for neutron induced cross sections on four elements was obtained. It was possible to establish first excitation functions for reactions on a radioactive target nucleus, one very long-lived product and one purely β^- emitting product. It was found that existing evaluations are not always reliable in the prediction of unknown cross sections. Although the experimental results of this work helped to considerably improve the calculations, some deficiencies still exist in case of complex particle emission (like d,t,α) and second chance emission (n,np) or (n,pn) etc.

Contents

Chapter 1

Introduction

The nuclear sciences started with the discovery of radioactivity by Becquerel [1] in 1896. When Rutherford observed the first nuclear reaction in 1919 [2], the history of nuclear reactions itself started. The next important step was the discovery of the neutron by Chadwick in 1932 [3,4]. Due to its electrical neutrality the neutron is able to interact with a nucleus at close distance and at all energies. It is thus well suited for studies of nuclear structure and nuclear reaction meachanisms.

Precise nuclear data are required for applications in many disciplines. The most obvious is the need in the field of nuclear energy, both for future fusion reactors and already existing fission reactors. As an alternative for deep geological storage of long-lived radioactive waste and for reprocessing and reuse of U and Pu the transmutation [5, 6] of long-lived elements into stable or short-lived nuclei is discussed. For this purpose and for energy production, accelerator-driven systems (ADS) have been proposed [7].

Neutron data for structural materials are needed to estimate the gas-production by (n,p) and (n,α) reactions, since gas inclusions negatively influence the mechnical stability and thus the usability time of this materials. The development of low activation materials as well as decay heat calculations are based on a good knowledge of excitation functions. All these demands have resulted in a long list of requests, which are collected in the *NEA high priority request list* for measurements of activation cross sections [8]. In cases, where measurements are very difficult or even impossible to do, model calculations are performed, for which the measured data are important to test the derived parameters.

This thesis deals with the measurement of neutron activation cross sections on the elements V, Mo, Tc and Pb in the energy region from threshold to 20 MeV. This chapter describes the basic properties and concepts of nuclear reactions and the possible measurement techniques. An overview of the existing data is given. Chapter 2 gives a more detailed motivation of the present investigation and Chapter 3 explains the performed experiments, covering the sample preparation, the performed irradiations and chemical separations and finally the data analysis. Chapter 4 briefly outlines the basic concepts of model calculations and in Chapter 5 the experimental results obtained are compared with model calculations and evaluations. Chapter 6 finally gives a summary of this work.

1.1 Basic Properties and Concepts of Nuclear Reactions

1.1.1 Cross Sections and Excitation Functions

A nuclear reaction $A(x,y)B$ occurs, when a projectile x comes sufficiently close to the target nucleus A, i. e. closer than the range of the nuclear forces (10^{-14} m). A particle y is then emitted, leaving a residual nucleus B, which can be either stable, radioactive or an isomer (see next section). The interaction of the projectile with the target nucleus is generally described in terms of the cross section $\sigma_{x,y}$, which is a measure of the probability for a reaction to occur. The cross section is usually given in barns ($1\text{b} = 10^{-28}\text{m}^2$) and is a function of the energy of the incident particle. The plot of $\sigma(E)$ against E is called the excitation function.

1.1.2 Isomeric Cross Sections

The first isomer was $^{234\text{m}}$Pa, dicovered by HAHN in 1921 [9]. Isomers are nuclides with the same mass and proton number, and thus the same chemical properties. They can be distinguished only by their respective radioactive decay, i. e. the decay mode and the half-life. The isomeric state decays either via γ-ray-emission to the groundstate, or via electron capture (EC), β- or α-particle emission to another nuclide. According to VON WEIZSÄCKER [10] the isomeric state is a long-lived excitated state, whose half-life can be explained by the spin of the different states. In case of a large spin difference between ground state and metastable state the isomeric transition (IT) would be forbidden and would result in a measureable half life. The population of the metastable state depends on the momentum and energy of the incident particle, i. e. it increases with increasing energy.

1.1.3 Energetics

The number of nucleons, the charge, energy, momentum, angular momentum, parity and isospin are preserved. The released energy of a nuclear reaction is the so called Q-Value, which can be calculated from the nuclide masses M_i and the speed of light c:

$$Q = (M_A + M_x - M_B - M_y) \cdot c^2. \tag{1-1}$$

A positive Q-Value denotes an exoenergetic reaction, while for endoenergetic reactions the Q-Value is negative. In the latter case the projectile has to deliver the necessary excitation energy. Taking into account also the conservation of momentum, we obtain the minimum energy which is required to initiate the nuclear reaction, the threshold energy:

$$E_{thres} = -Q \cdot \left(1 + \frac{M_x}{M_A}\right), \tag{1-2}$$

Table 1.1: Q-Values and reaction thresholds of the investigated reactions on vanadium, molybdenum, technetium and lead, calculated with QTOOL [11], based on the masses given by AUDI AND WAPSTRA [12]

Nuclear reaction	Q-Value (MeV)	Threshold (MeV)
^{51}V(n,n'α)^{47}Sc	-10.291	10.495
^{50}V(n,α)^{47}Sc	0.761	0.0
^{51}V(n,α)^{48}Sc	-2.058	2.099
^{51}V(n,p)^{51}Ti	-1.688	1.722
^{99}Tc(n,n'γ)$^{99\mathrm{m}}$Tc	0.0	0.143
^{99}Tc(n,p)^{99}Mo	-0.575	0.581
^{99}Tc(n,α)^{96}Nb	3.927	0.0
^{204}Pb(n,p)^{204}Tl	0.019	0.0
^{204}Pb(n,2n)$^{203\mathrm{g}}$Pb	-8.394	8.436
^{204}Pb(n,3n)$^{202\mathrm{m}}$Pb	-15.318	17.564
^{206}Pb(n,3n)$^{204\mathrm{m}}$Pb	-14.820	17.078
^{206}Pb(n,α)^{203}Hg	7.129	0.0
^{92}Mo(n,2n)$^{91\mathrm{m}}$Mo	-12.673	13.407
^{94}Mo(n,2n)$^{93\mathrm{m}}$Mo	-9.678	12.260
^{100}Mo(n,2n)^{99}Mo	-8.290	8.373
^{92}Mo(n,α)$^{89\mathrm{m}}$Zr	3.710	0.588
^{100}Mo(n,α)^{97}Zr	2.410	0.0
^{92}Mo(n,p)$^{92\mathrm{m}}$Nb	0.426	0.0
^{94}Mo(n,p)^{94}Nb	-1.263	1.277
^{95}Mo(n,p)$^{95\mathrm{m}}$Nb	-0.143	0.384
^{96}Mo(n,p)^{96}Nb	-2.404	2.430
^{97}Mo(n,p)$^{97\mathrm{m}}$Nb	-1.151	1.907
^{97}Mo(n,p)$^{97\mathrm{g}}$Nb	-1.151	1.164
^{98}Mo(n,p)$^{98\mathrm{m}}$Nb	-3.803	3.304
^{95}Mo(n,np)^{94}Nb	-8.632	8.724
^{96}Mo(n,np)$^{95\mathrm{m}}$Nb	-9.298	9.631
^{97}Mo(n,np)^{96}Nb	-9.226	9.322
^{98}Mo(n,np)$^{97\mathrm{m}}$Nb	-9.794	10.643
^{98}Mo(n,np)$^{97\mathrm{g}}$Nb	-9.794	9.900

where M_x and M_A are the masses of the projectile and target nucleus, respectively. The calculated Q-values and reaction thresholds for the investigated reactions are shown in table 1.1.

1.1.4 Reaction Channels

For a given particle energy different reactions are possible depending on the Q-Values. In the investigated energy range up to about 21 MeV, these so called reaction channels are, for example, elastic and inelastic scattering, neutron capture, charged particle emission and multiple neutron emission. The sum of these partial cross sections is called the total cross section σ_T, which can be determined directly via transmission measurements. The shape of some excitation functions can be explained with these competing reaction channels: a steep rise near the threshold followed by a plateau and then a decrease at energies, where other reactions become energetically possible. The contributions of different channels to the total cross section depend also on the mass region. For heavier nuclei and thus higher nuclear charge, for example, the emission of charged particles is increasingly suppressed due to the increasing Coulomb barrier.

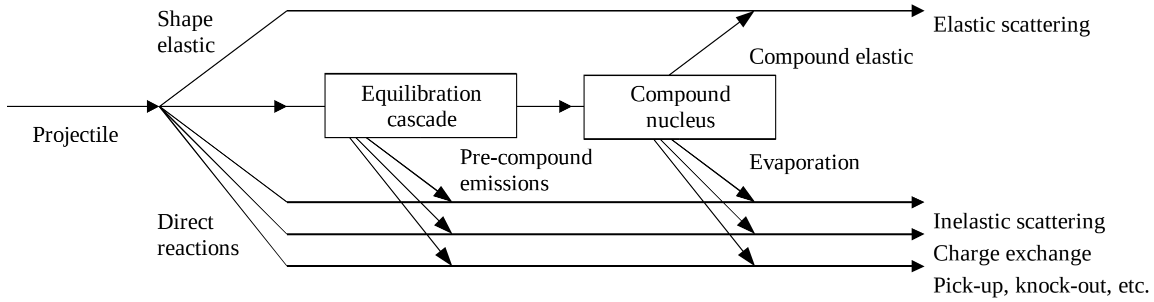

Figure 1.1: Direct, pre-compound and compound nucleus processes in nuclear reactions, taken from [13]

1.1.5 Reaction Mechanisms

Nuclear reactions may entail three types of reaction mechanisms: direct, compound nucleus and preequilibrium effects. The contribution of these processes depends on the given reaction and the energy of the incident particle. The three types can be distinguished by their angular distributions and time scales (Fig. 1.1).

Direct Reactions For projectile energies above 50 MeV and for light target nuclei (A<30) a direct transition from the entrance to the exit channel occurs within a very short timescale of about 10^{-22} seconds, which is roughly the time it takes to traverse the nuclear field. There is no creation and subsequent decay of a highly excited intermediate state, which results in an anisotropic and forward-peaked angular distribution. Typical examples of direct reactions are elastic and inelastic scattering, charge transfer, stripping, pick-up, and knock-on processes.

Compound Nucleus Reactions Most of the low energy nuclear reactions follow this mechanism, which was first described by Bohr [14]. The incident particle is captured to form a highly excited intermediate state C^*, whereby the energy of the projectile is distributed over all nucleons.

$$A + x \rightarrow C^* \rightarrow B + y \tag{1-3}$$

The compound nucleus decays by evaporation of nucleons with a Maxwellian energy distribution. The emission is symmetric to 90° and the interaction time is about 10^{-14} to 10^{-18} seconds.

Precompound or pre-equilibrium Reactions On a time scale this process lies between the direct and the compound nucleus reactions. The particle is emitted before the energy is evenly distributed over all nucleons, thus giving a smooth forward-peaked angular distribution. Another characteristic is a pronounced high-energy tail in the excitation function.

Table 1.2: Characteristics of the online and offline methods for cross section measurements

Spectroscopic method	Activation method
online	offline
double differential cross sections	integral cross sections
particle selective	product selective
thin sample required	thick sample is possible
product may be stable or radioactive	product must be radioactive

1.2 Experimental Techniques

The main subject of this work is the examination of nuclear reactions of the type $A(n, x)B$, where B is the reaction product, which can be either stable or radioactive. Two standard methods commonly used for neutron induced reaction cross section measurements involve direct (*online*) detection of the emitted particles x, also known as spectroscopic method or *offline* identification of the activation products B, which can take place long after the actual irradiation experiment. In case of a radioactive product the activation method is applied, which was the main technique used in this work. An other method is based on the determination of mass of the reaction product via mass spectrometry (MS) or accelerator mass spectrometry (AMS), suitable for stable or sufficiently long-lived isotopes. Table 1.2 shows a comparison of the spectroscopic method and the activation method.

1.2.1 Detection of Emitted Particle

This online method involves the measurement of the energy and angular distribution of the emitted particle, thus resulting in double differential cross section data. A thin sample is required for measurements of (n,charged particle) reactions, since the ranges of the emitted particles are rather short. Another drawback is the particle selectivity of this method. It is not easy to distinguish whether, for example, an emitted proton originates from an (n,p) or from an (n,np) reaction.

1.2.2 Activation Method

Since the activation method involves the measurement of the radioactive product, it is not possible to distinguish an (n,np) reaction from an (n,d) reaction, or if it was produced via several production routes, e. g. ^{100}Mo(n,2n)^{99}Mo or ^{98}Mo(n,γ)^{99}Mo. But in contrast to the online methods it is possible to use a large sample, which may require further radiochemical processing of the irradiated sample material.

The yield of a nuclear reaction can be calculated, when the cross section σ and the neutron flux Φ are known. On the other side, the cross section can be deterimened when the flux and the yield are measured. The production rate of the nuclide B is given by:

$$\frac{dN_B}{dt} = \sigma \cdot \Phi \cdot N_A, \tag{1-4}$$

where N_A is the number of target nuclei. It is assumed that this number does not change during the irradiation and that the flux is constant over time and is the same everywhere in the sample (thin target). For a radioactive product nucleus N_B, also its decay has to be taken into account, which is given by

$$-\frac{dN_B}{dt} = \lambda \cdot N_B. \tag{1-5}$$

Combining equations 1-4 and 1-5 we obtain:

$$\frac{dN_B}{dt} = \sigma \cdot \Phi \cdot N_A - \lambda \cdot N_B. \tag{1-6}$$

The number of product nuclei after an activation or exposure time t_e is obtained by integration of the above equation between the boundaries $t = 0$ und t_e:

$$N_B(t_e) = \frac{\sigma \cdot \Phi \cdot N_A}{\lambda}\big(1 - e^{-\lambda t_e}\big). \tag{1-7}$$

After a cooling time t_c, which is the elapsed time from end of the activation, the induced activity is given by:

$$A = -\frac{dN_B(t_e)}{dt} = \lambda N_B(t_e) = \sigma \cdot \Phi \cdot N_A\big(1 - e^{-\lambda t_e}\big)e^{-\lambda t_c}, \tag{1-8}$$

which is the so called activation formula. Considering a nuclear reaction of the type

$$A(n,x)B \xrightarrow{\beta^-,\ \beta^+ \text{ or } EC} C \tag{1-9}$$

the cross section is determined by measuring the induced activity of the activation product B. This is most conveniently done by measuring the γ-rays, following the β decay, via γ-ray-spectroscopy using HPGe or NaI detectors. In cases were no γ-rays are emitted the activity has to be determined by β-counting or X-ray spectroscopy. This usually requires some radiochemical processing of the irradiated sample material, which will be explained in the next section. If a metastable state is populated, the isomeric cross section can either be determined by measuring the γ-rays of the internal transition (IT) leading to the ground state or the γ-rays succeeding the β-decay of the metastable state.

The determination of the cross section for the complex particle emission reactions like (n,t) or (n,^{7}Be) denote a special case since here the emitted particle is radioactive and can be measured *offline*. The radioactive tritium is accumulated and measured via β-counting after chemical separation [15]. In cases of (n,α)or (n,^{3}He) reactions the accumulated gas is measured via mass spectrometry [16].

1.2.3 Radiochemical Separations

Occasionally a radiochemical separation of the activation product from the irradiated sample is required. This can be the case when nuclear reactions with low yields are studied and thus a large sample has to be irradiated. This would result in a bad counting geometry and the count rate would be reduced due to self-absorption effects. This is especially a problem when the activation product does not emit γ-rays, but only β particles or X-rays. The preparation of a thin sample is mandatory in those cases. Sometimes a short-lived product has to be separated from a longer-lived matrix activity, which can cause a too high background, overlapping γ-rays or a too high detector dead time.

The radiochemical separation should have a high chemical yield, provide a good decontamination from radioactive impurities and should be reproducible, and fast in case of a short-lived activation product.

Commonly used radiochemical methods are for example precipitation and crystallization, co-precipitation by adsorption, electroplating, solventextraction, ion-exchange, HPLC (high performance liquid chromatography) or thermochromatography.

Some of the techniques are briefly outlined below.

1.2.3.1 Co-precipitation and Adsorption

Co-precipitation is based on adsorption of the radionuclide on gelatinous or colloidal precipitates, which offer a large surface, e. g. $Fe(OH)_3$, $Al(OH)_3$, MnO_2, AgBr, $BaSO_4$ or aluminium silicates. After the precipitation process the precipitate is filtered or centrifuged off, and again disolved. The radionuclide is thereafter separated from the carrier with one of the above mentioned methods. Co-precipitation is the method of choice when no carrier added (n.c.a) radionuclides have to be separated from the bulk of target material. This is for example the case when a low concentration of a radionuclide has to be separated from strong matrix activities with a subsequent preparation of a thin sample for β or X-ray counting.

1.2.3.2 Solvent Extraction

The basic reaction underlying liquid-liquid extraction is the following:

$$M_{aq}^{n+} + nHL_{org} \Longleftrightarrow ML_{n,org} + nH_{org}^{+}, \tag{1-10}$$

where M_{aq}^{n+} is a metal ion in aqueous solution and HL_{org} the reagent initially dissolved in the organic phase or the organic phase itself. During the extraction process a product $ML_{n,org}$ is formed, that is better soluble in the organic phase than in the aqueous phase. The extraction equilibrium can be described with the following constant:

$$K_{eq} = \frac{[ML_n]_{org}[H^+]_{aq}^n}{[M^{n+}]_{aq}[HL]_{org}^n} \tag{1-11}$$

The three necessary steps for a liquid-liquid extraction are extraction, scrubbing and stripping. In the first extraction step the main solute is transfered from the aqueous to the organic phase, often together with some of the impurities. The impurities are removed from the organic phase in the scrubbing step, which involves washing of the organic phase with a new immiscible (aqueous) phase. In the last step the main solute is back extracted from the organic phase into an aqueos solution.

1.2.3.3 Ion Exchange

Ion-exchange methods can be treated similar to the extraction method. The ions of an aqueous solution interact with the active groups of an ion exchange resin. Depending of the charge of these active groups they can pick up either cations or anions. Thus we distinguish between cation exchangers with active groups like (-SO_3)$^-$ or (-COO)$^-$ and anion exchangers with groups like (-NR_3)$^+$. For a typical cation exchange equilibrium, the reaction can be written as:

$$nR(SO_3)H + M^{n+} \Longleftrightarrow nH^+ + R(SO_3)_nM, \tag{1-12}$$

where R is the resin to which the active groups are attached. M is the metal which has to be exchanged against hydrogen H. The eqation represents a chemical equilibrium and can be shifted to the left or to the right by choosing the appropriate conditions, e. g. the molarity of the acid which is used as eluent. The equilibrium constant is given by an equation similar to eq. 1-11:

$$K_{eq} = \frac{[R(SO_3M][H^+]^n}{[R(SO_3H]^n[M^{n+}]}. \tag{1-13}$$

The exchange procedure consists again of three steps: loading, washing and elution. The conditioned ion exchange resin is first loaded with the desired metal ion and in a second step the depleted solution is washed from the resin. In the final elution step the metal ion is transfered back to the aqueous solution.

1.3 Neutron Sources

Neutrons are available in large amounts in nuclear reactors, since they are emitted during the fission process. Also the spontanously fissioning nuclide ^{252}Cf can be used as a neutron source. Another production route involves the interaction of radioactive radiation with suitable nuclides. A mixture of beryllium and an α- or γ-source of high enough energy delivers neutrons via the ^{9}Be(α,n)^{12}C or the ^{9}Be(γ,n)2α reaction. Suitable α-emitters are, for example, the long-lived radionuclides ^{226}Ra or ^{210}Po. We speak then about a radium-beryllium- or polonium-beryllium-neutron source. These methods produce neutrons with a continous energy distribution. A continuum or white spectrum neutron source can also be obtained using an electron accelerator. In this photon neutron source the energy is continous, since the incident photons are produced through the bremsstrahlung from the converter. Neutrons with well-defined energies can be identified and selected from the spectrum by the time-of-flight (TOF) method.

For excitation function measurements monoenergetic neutrons are required. For this purpose mainly accelerator based monoenergetic neutron sources are employed, which will be discussed in more detail below.

1.3.1 Monoenergtic Neutron Source Reactions

A neutron is considered monoenergetic when the energy spectrum consists of a single line with an energy width that is much less than the energy itself. Most measurements to date have been done using the “big four” reactions ^{3}H(p,n)^{3}He, ^{7}Li(p,n)^{7}Be, ^{2}H(d,n)^{3}He, and ^{3}H(d,n)^{4}He utilizing cyclotrons or electrostatic accelerators (Van de Graaff accelerators). Some of the properties of these reactions are summarised in table 1.3. In the case of D-D and D-T reactions, the large positive Q-values and the low atomic numbers make it possible to produce high yields of fast neutrons even at low incident deuteron energies. Another requirement for the high yield is a small energy loss of the projectile in the target and a high neutron production cross section. Since the ^{3}H(d,n)^{4}He reaction shows a broad resonance with a maximum value of 5 barns at $E_d = 107$ keV (cf. figure 1.2) this reaction allows the production of fast neutrons with energies around 14 MeV already with small accelerators.

Table 1.3: Comparison of monoenergetic neutron sources, taken from [17]

Reaction	Q-value (MeV)	Break up reaction	Threshold (MeV)	Monoenergetic neutron energy range (MeV)
^{7}Li(p,n)^{7}Be	-1.644	^{7}Li(p,n)^{7}Be*	2.37	0.12−0.6
^{3}H(p,n)^{3}He	-0.763	T(p,np)D	8.35	0.3−7.6
^{2}H(d,n)^{3}He	$+3.270$	D(d,np)D	4.45	1.64−7.75
^{3}H(d,n)^{4}He	$+17.590$	T(d,np)T	3.71	11.74−20.5
		T(d,2n)^{3}He	4.92	

Usually the desired neutron energy determines which reaction should be chosen. The last column in table 1.3 shows the range of the monoenergetic neutrons for the four most commonly used reactions. All these reactions do not strictly produce only monoenergetic neutrons. Secondary neutrons due to breakup of the projectile or the target nucleus contaminate the neutron spectrum and can thus lead to too high cross sections. Other background neutrons are produced by interaction of the incident charged particle with structural material of the setup, like the beamstop or the target backing. In case of a D_2-gas cell the contributions from these background neutrons can relatively easily be determined via with gas-in / gas-out measurements. For solid tritium targets a blank measurement using a non tritium containing dummy target can be performed, but this is a somewhat more demanding task.

From table 1.3 it can be seen that none of the reactions behave in a monoenergetic way in the neutron energy range of about 8 to 12 MeV. However, with the precise measurement of the breakup reaction D(d,np)D by CABRAL *et al.* [18] the usable energy range for the DD reaction could be extended to 12 MeV. A careful choice of the construction material, especially of the beam stop [19] helps considerably to further suppress background neutrons.

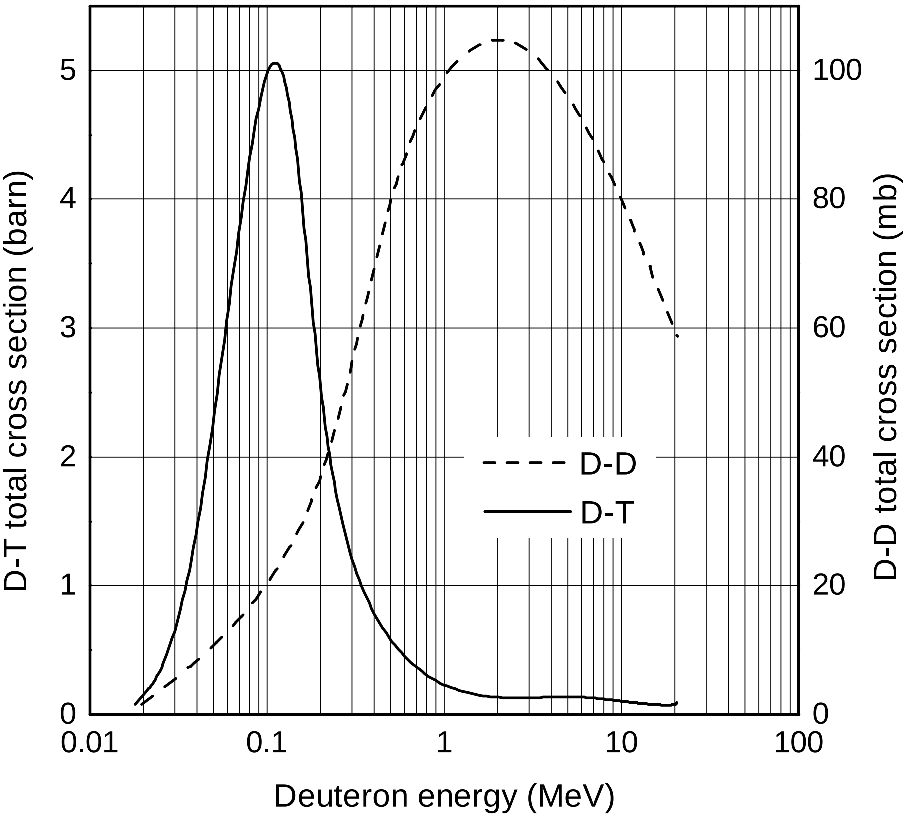

Figure 1.2: Energy dependence of the total cross section for the ^{2}H(d,n)^{3}He and ^{3}H(d,n)^{4}He reactions, taken from [17]

1.3.2 Neutron Spectrum and Flux

1.3.2.1 Neutron Spectrum

Neutrons can be detected indirectly by scattering and absorptive studies. In scattering reaction, the neutron is determined by using time-of-flight (TOF) techniques. In this method the time T which the neutron needs to traverse a flight path of length L is determined. The velocity L/T and thus the kinetic energy of the neutron is given by the equation:

$$E_n = \frac{1}{2} m_n \left(\frac{L}{T} \right)^2 . \qquad (1\text{-}14)$$

Since these measurements are rather time consuming, it is not practical to perform TOF measurements for each activation experiment. A more popular method is based on the measurement of the activity induced in several activated foils. Using different standard reactions with different excitation functions and, in particular different thresholds, it is possible to unfold the spectrum. An overview of suitable excitation functions is shown in figure 1.4. A good knowledge of the excitation functions and the decay characteristics of the activation products is essential. This solution depends on a once measured neutron spectrum, which is changing with time due to consumption of tritium and buildup of

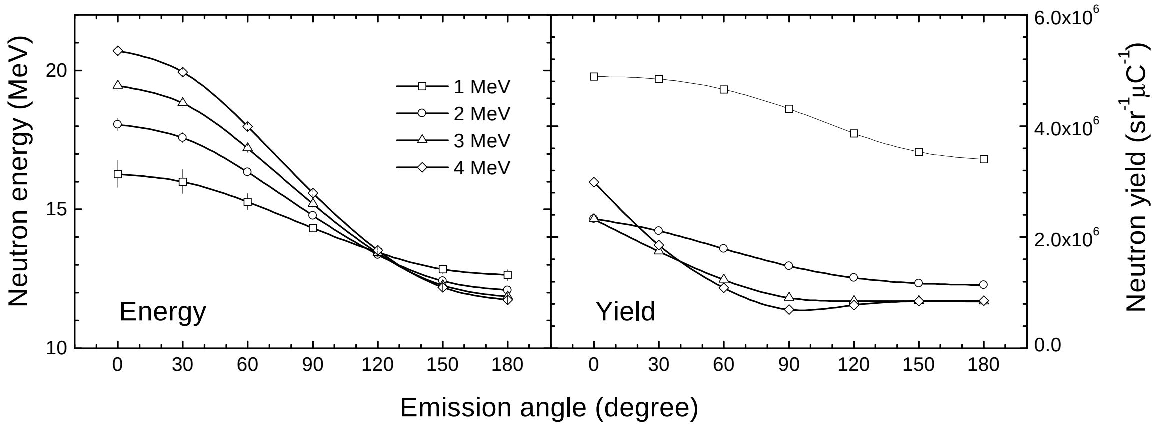

Figure 1.3: Angular distribution of neutron energy and neutron yield for the ^{3}H(d,n)^{4}He reaction. The calculations were done for four different incident deuteron energies using the program KINEMA (cf. section 3.3.2)

deuterium (in case of a solid TiT target). These changes in different energy regions are monitored with the different activation foils and the the actual spectrum can be adjusted.

1.3.2.2 Neutron Flux

The direct measurement of an activation cross section requires a knowledge of the neutron flux Φ according to equation 1-8. Measurement of the flux for DD and DT reactions on an absolute scale is possible by means of the associated particle technique [21] to an accuracy of about 1%. The method makes use of the fact that each neutron produced via the ^{2}H(d,n)^{3}He or ^{3}H(d,n)^{4}He reaction is accompanied by a ^{3}He or ^{4}He particle, respectively. Their kinetic properties can be measured by the interaction energy and the emission angle of the neutron. The neutron flux in the respective solid angle can be calculated by detecting the associated particle within a well defined recoil solid angle in a surface barrier detector [22–24] In order to take advantage of the high accuracy of this method, the geometry has to be defined with at least the same precision, which makes this technique difficult to use.

Therefore, most nuclear reaction cross section measurements are done relative to a standard cross section [20], that means using a material and a specific reaction on it, whose cross section is well established. The cross section is then derived from the ratio of the measured reaction rate in the sample material and to that in the reference material. In addition to a good knowledge of the cross section the reference reaction should meet the following requirements:

- ⇨ a flat response, that means the excitation function does not vary rapidly with energy and is thus is less sensitive to the correct energy scale,
- ⇨ a proper reaction threshold, i. e. not too close to the energy region where it is used and sufficiently high to be not too sensitive to contamiations with low energy neutrons,
- ⇨ sufficiently long half-life compared to the irradiation time in order to enable proper integration over a time-dependent neutron flux.

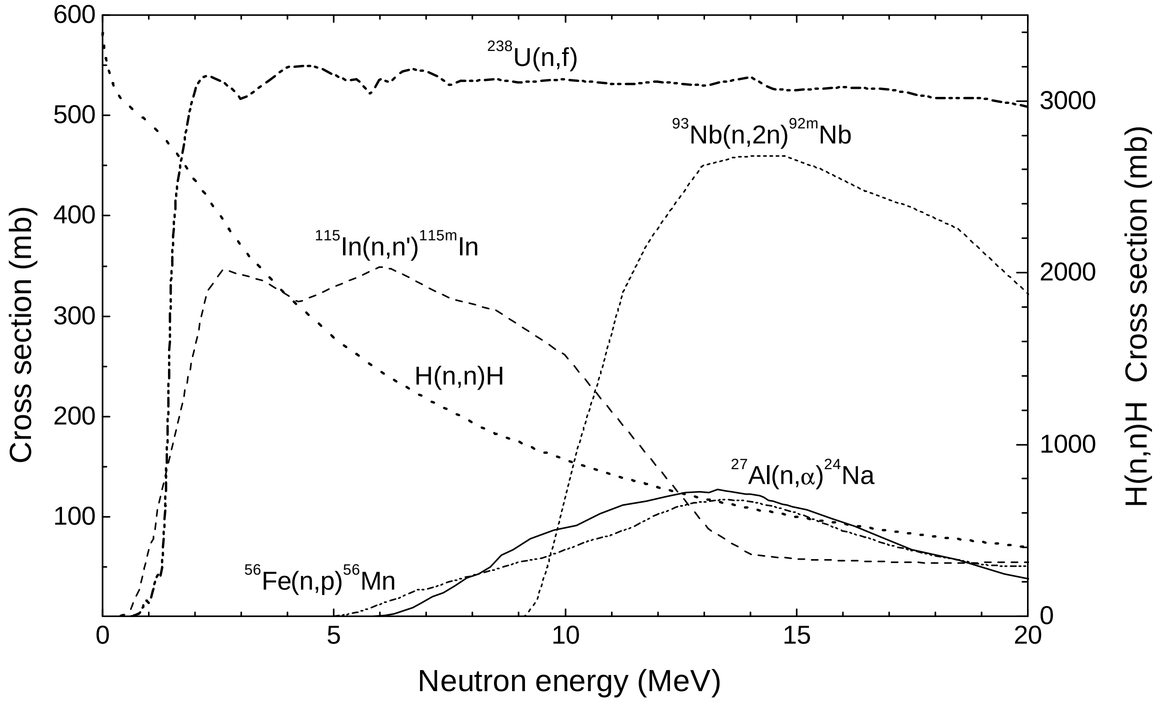

Figure 1.4: Some evaluated cross sections for the reference reactions frequently used in activation experiments [20]

The most fundamental reference is certainly the hydrogen elastic scattering cross section, which is the best known cross section over a wide energy range, at least for $E_n < 10$ MeV. But not only the uncertainty of the cross section plays a role, also its implementation. Due to uncertainties in the efficiency of the counter (telescope) employed to detect the proton recoils and in the density of the hydrogen atoms in the radiator foil the overall uncertainty is about 2.5 %.

The neutron flux of fast neutrons can also be determined by the fission reaction ^{238}U(n,f), which is well evaluated up to 20 MeV [20]. The method is implemented by using a well defined fission deposit and prompt detection of fission fragments by means of a low-mass ionization chamber [25,26]. Due to its quasithreshold behaviour, the ^{238}U(n,f) reaction is most useful as a reference in the fast-neutron region ($\leq$ 2 MeV, when the excitation function reaches its first plateau) being less sensitive to parasitic low energy neutrons. The main sources of uncertainty involved in this method are the properties of the thin uranium deposit (mass, thickness, isotopic purity) and the fission fragment detection efficiency.

The most convenient method to monitor the neutron flux is thus the use of chemically stable metal monitor foils that can be obtained with sufficient purity and where the induced radioactivity is easily measured. This method was also employed in this work by using In, Ni, Nb, Co and Al foils in a sandwich geometry. The evaluated cross sections used are shown in figure 1.4 and the origin is given in table 3.5, page 28. Evaluated data sets are produced through the process of critical comparison, selection, renormalization and averaging of the available experimental data, normally complemented by nuclear model calculations. Many different evaluations exist for all types of nuclear reactions, some of which are EAF-99[1], JENDL-3.2[2], JEF[3] and ENDF/B-VI[4].

1.4 Status of available Cross Section Data for V, Mo, Tc and Pb Isotopes

A survey of the available cross section data for neutron induced reactions on Tc, Pb, Mo, and V isotopes showed that most measurements were done in the 14 MeV region. For some cases no data were available and in other cases the existing data are rather discrepant. Each element is reviewed below.

1.4.1 Vanadium

The main purpose of the activation studies on vanadium is the determination of the reaction cross section for the production of ^{47}Sc. A few datasets can be found in the literature [31–35], since vanadium alloys have long been considered by the reactor comunity for their low-activation properties. Recent comparisons and experiments in various neutron fields [36–39] pointed out the existing discrepancies.

1.4.2 Molybdenum

Due to the inconvenient half-life of 20300 years of the product ^{94}Nb only two cross section measurements exist for the ^{94}Mo(n,p)^{94}Nb reaction, both between 14 and 15 MeV neutron energy. Both Greenwood *et al.* [40] and Ikeda and Konno [41] used enriched ^{94}Mo and ^{95}Mo samples and could thus subtract contributions from the ^{95}Mo(n,np)^{94}Nb reaction. However, due to the limited energy range, both measurements could only give a trend; a full excitation function is not established. For the other reactions to be studied (cf. table 1.1) in general more data are available, especially in the 14 MeV region. However, above 15 MeV only a single dataset exists [42].

1.4.3 Technetium

For the ^{99}Tc(n,n'γ)$^{99\mathrm{m}}$Tc, ^{99}Tc(n,p)^{99}Mo and ^{99}Tc(n,α)^{96}Nb reactions four experimental data sets can be found in the literature. All measurements were done in the 14 MeV region and show some discrepancies. The measurements by Golchert *et al.* [43] and Qaim [44] involved a radiochemical separation of the activation product from the radioactive target material and subsequent β^-- or γ-ray counting. The old measurement of Goldstein [45] and the recent measurement of Ikeda *et al.* [46] were done in a non-destructive way with standard γ-ray-spectroscopy.

---

[1] European Activation File [27]

[2] Japanese Evaluated Nuclear Data Library [28]

[3] Joint European File [29]

[4] Evaluated Nuclear Data File [30]

1.4.4 Lead

The main goal in this work is the determination of the reaction cross section for the formation of ^{204}Tl from natural lead. No experimental data exist for the $^{\text{nat}}$Pb(n,x)^{204}Tl reaction except for a single measurement done with a fission neutron spectrum [47]. While there are no data for the ^{204}Pb(n,3n)$^{202\text{m}}$Pb reaction and only one dataset above 20 MeV for the ^{206}Pb(n,3n)$^{204\text{m}}$Pb reaction [48], an extensive dataset exists for the ^{204}Pb(n,2n)^{203}Pb reaction. However, above 15 MeV only two datasets exist [49,50], which show rather large uncertainties of 30-50%.

Chapter 2

Aims and Scope

Most of the reactions to be investigated in this work are listed in the *High Priority Request List* of the OECD-NEA Nuclear Science Commitee, together with the demanded accuracies. All the reactions lead to radioactive products and are thus measureable with the activation technique using high resolution γ-ray spectrometry and low-level beta counting in combination with radiochemical separation. Particular focus should be on V, Mo, ^{99}Tc and Pb.

As already outlined in the introduction, vanadium is considered as a candidate low-activation structural material in devices with a hard neutron spectrum, like fusion reactors and Accelerator Driven Systems (ADS). In ADS systems with an energy range up to a few GeV, neutrons with energies up to 20 MeV play a significant role with regard to helium and hydrogen gas production. A good experimental database exists for the ^{51}V(n,α)^{48}Sc reaction, but not for the $^{\mathrm{nat}}$V(n,xα)^{47}Sc reaction. A few datasets exist around 14 MeV, but for higher energies the experimental results are scarce and discrepant. Recent Benchmark irradiations with a hard neutron spectrum for the production of ^{47}Sc showed large deviations from the values calculated using the EAF-97 library. Calculated/Experimental (C/E) values of 1.5 or more were obtained depending on the neutron spectrum used. The aim of this work is to resolve the discrepancies in the data for the $^{\mathrm{nat}}$V(n,xα)^{47}Sc reaction above 14 MeV and to extend the excitation function to lower energies, where no data exist. As a consistency check the cross section for the ^{51}V(n,α)^{48}Sc and ^{51}V(n,p)^{51}Ti reactions should also be measured.

Of special interest concerning long-lived radioactive waste is the production cross section for the nuclide ^{94}Nb from the structural material molybdenum. It is formed via the reactions ^{94}Mo(n,p)^{94}Nb and ^{95}Mo(n,np)^{94}Nb. Since the half-life of this isotope is 20300 years, standard irradiation conditions and counting methods can not be used. A special irradiation setup needs to be developed that would allow the use of as much material as possible and which would ideally cover several energies in one single long irradiation. The induced activity could be measured via nondestructive γ-ray spectrometry using the low-level counting facility in the underground laboratory HADES. In addition a radiochemical method should be used to separate radioactive Nb from the bulk of Mo in order to reduce the background activities and to improve the counting geometry. In this case only molybdenum of natural isotopic composition can be used, due to the large amount of needed sample material. On the other hand, an almost complete set of enriched Mo isotopes is available on loan from JAERI, which could be used to measure the competing (n,p) and (n,np) reactions on neighbouring isotopes leading to the same endproduct. These are the reactions ^{95}Mo(n,p)^{95m}Nb and ^{96}Mo(n,np)^{95m}Nb, ^{96}Mo(n,p)^{96}Nb and ^{97}Mo(n,np)^{96}Nb, and ^{97}Mo(n,p)^{97}Nb and ^{98}Mo(n,np)^{97}Nb. In the latter case both the isomeric state and the ground state could be measured. Special emphasis should be on those energy regions, where no or only a few datasets exist.

Among the target materials to be be used in this project, technetium denotes a special case. It has no stable isotope, but is available in large quantities in reactor waste. The half-life of ^{99}Tc is $2.1 \cdot 10^5$ years. Neutron induced cross sections on ^{99}Tc are of applied interest for an understanding of neutron transport and gas production in fission fragments in conventional reactors and ADS. The reactions ^{99}Tc(n,n'γ)^{99m}Tc, ^{99}Tc(n,p)^{99}Mo and ^{99}Tc(n,α)^{96}Nb should be studied with the activation technique using nondestructive γ-ray spectrometry. The reaction ^{99}Tc(n,n'γ)^{99m}Tc is difficult to measure due to its very low threshold und thus high sensitivity to background neutrons. Since the necessary correction would require a good knowledge of the excitation function, this reaction should be measured from 0.5 to 20.6 MeV. Special attention needs to be paid to the preparation and handling of the radioactive target material and to the emitted Bremsstrahlung, which would cause a high background in the measurement of the induced activities.

The reaction ^{204}Pb(n,p)^{204}Tl is of relevance to gas production and decay heat calculations in ADS and can only be measured via beta counting, since ^{204}Tl does not emit any γ-rays. Therefore a method has to be developed to separate the induced Tl activity from the bulk of target material, which should be high purity lead without or only negligible amounts of Tl impurities. In addition some (n,xn) reactions on ^{204}Pb and ^{206}Pb relevant for neutron transport and the ^{206}Pb(n,α)^{203}Hg reaction relevant again for gas production should be measured via standard γ-ray spectrometry.

All measured excitation functions should be compared with existing evaluations and nuclear model calculation performed with the code STAPRE for reactions on technetium and lead and with a modified version STAPRE-H95 for reactions on vanadium and molybdenum.

Chapter 3

Experimental Methods

3.1 Samples

3.1.1 Vanadium

Samples consisted of natural vanadium with an isotopic composition of 0.250(4) % ^{50}V and 99.750(4) % ^{51}V [51]. The samples were prepared by punching discs of 10 and 13 mm diameter and 350-450 μm thickness from metallic vanadium sheets. One to four of those were sandwiched between two monitor foils.

3.1.2 Molybdenum

Due to the very long half-life of ^{94}Nb ($T_{1/2}$ = 20300 y) a fairly large sample and a long irradiation time were needed to produce enough ^{94}Nb-activity. The thickness of the sample was chosen as a compromise between maximum sample mass and minimum self-absorption expected in a non-destructive γ-ray-spectrometric measurement. For a thickness of 14 mm about 50% absorption is estimated. The sample material, supplied by Advent[1], was arranged around the neutron source in a special geometry, which allows a simultaneous irradiation with three different neutron energies, thus considerably reducing the necessary beam time. The complete sample was subdivided into three parts: the first one contained 7 disks of 5 cm diameter and 2 mm thickness, which were irradiated under 0°. The rest was arranged in a 2-ring-geometry, each ring containing 49 squares of 24 mm side-length and 2 mm thickness, 7 stacked together at a time. The total mass of the sample was 1488.2 g. A detailed view of the irradiation and counting geometry is given in Figure 3.1. Al, Nb, Ni and Co monitor foils were inserted in two stacks of each ring and in the front disk in order to monitor the intensity of the neutron flux and its gradient within the sample. The position of the beam was checked by attaching small Co foils of 10 mm diameter to each stack of the first ring and measuring the activity distribution.

In addition to the natural samples, a set of enriched isotopes was also irradiated. They were borrowed from JAERI-Tokai-mura[2] and made by wrapping about 50 mg of the enriched metal in small paper envelopes of 1 cm^2 size. The isotopic composition of

---

[1] Advent Research Materials Ltd., Oakfield Industrial Estate, Eynsham·Oxon, England OX8 1JA

[2] Japanese Atomic Energy Research Institute, Tokai-mura, Japan

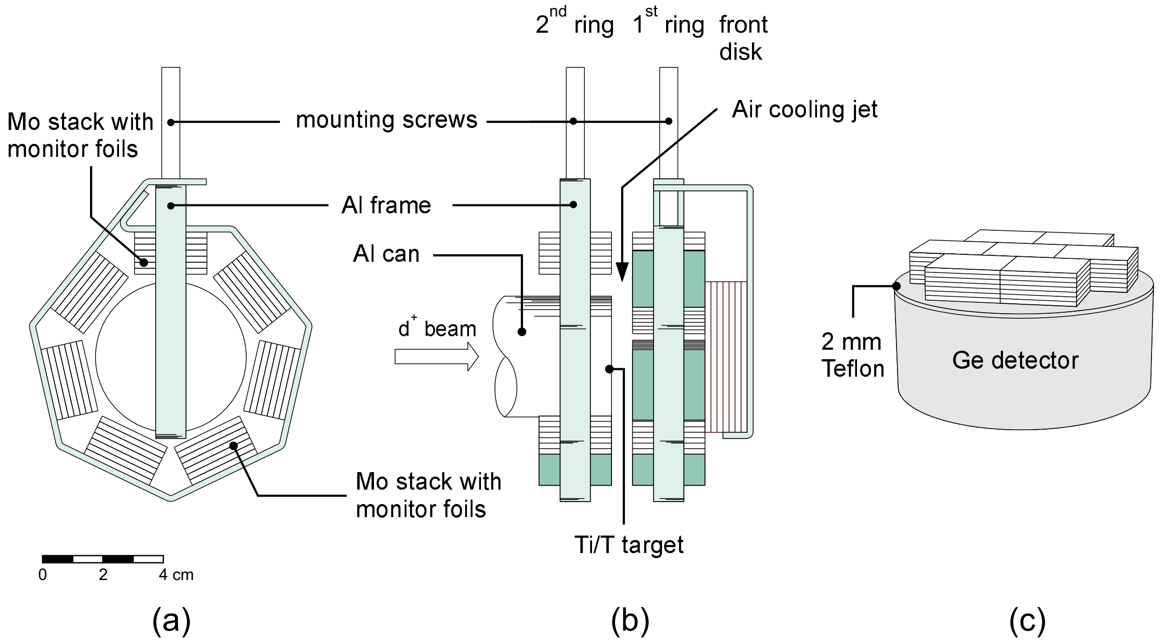

Figure 3.1: Sketch of the used Mo-target: (a) the front view shows the front disc and the first ring (b) a part of the second ring is not shown in order to allow a view on the beam line (c) counting geometry for the 1st and 2nd ring

the used samples is shown in Table 3.1.

Table 3.1: Isotopic composition of enriched and natural Mo samples

sample	^{92}Mo	^{94}Mo	^{95}Mo	^{96}Mo	^{97}Mo	^{98}Mo	^{100}Mo
natural sample[a]							
^{nat}Mo	14.84(35)	9.25(12)	15.92(13)	16.68(2)	9.55(8)	24.13(31)	9.63(23)
enriched samples[b]							
^{92}Mo	97.37(10)	0.68(5)	0.52(5)	0.37(5)	0.18(5)	0.40(5)	0.50(5)
^{94}Mo	0.71(5)	92.03(10)	5.18(10)	0.83(5)	0.40(5)	0.67(5)	0.19(5)
^{95}Mo			no enriched sample available				
^{96}Mo	0.18(3)	0.20(5)	0.93(5)	96.76(10)	0.96(5)	0.80(5)	0.17(3)
^{97}Mo	0.22(5)	0.24(5)	0.59(5)	1.34(5)	94.25(10)	3.07(10)	0.30(5)
^{98}Mo	0.32(2)	0.22(2)	0.45(2)	0.59(2)	0.69(2)	97.18(10)	0.55(2)
^{100}Mo	0.53(3)	0.18(3)	0.29(3)	0.34(3)	0.28(3)	0.96(5)	97.42(5)

[a] isotopic composition taken from [51]

[b] isotopic composition taken from datasheet received from JAERI

3.1.3 Technetium

Thin ^{99}Tc-samples were prepared at the Institute für Nuklearchemie, Forschungszentrum Jülich, by pressing about 0.5 g of the metal to disks of 13 mm diameter. The purity of the material was checked by γ-ray-spectroscopy, which showed a negligible impurity of ^{98}Tc ($T_{1/2} = 4.2 \cdot 10^6$ y) at the ppm level. Aluminium containers with a wall thickness of 0.2 mm (0.4 mm on the cylindrical side) were used to guarantee mechanical stability of the samples and to prevent contamination of the environment with the radioactive material. The capsules were further sealed in polyethylene bags (0.2 mm thick).

3.1.4 Lead

The reactions on Pb isotopes were studied using both lead of natural isotopic composition and enriched ^{206}Pb as sample material. Since the isotopic composition of natural Lead varies over quite a large range [51], depending on age and origin [52], an isotopic analysis of the sample was performed by the IRMM Isotopic Measurement Unit. A comparison of the obtained results is shown in Table 3.2 together with the representative values. Special attention had to be paid also to the Tl-impurity of the sample, since the product of interest ^{204}Tl can not be formed only via the (n,p)-reaction on ^{204}Pb but also via the ^{205}Tl(n,2n)-reaction. Assuming a cross section of 2000 mb for the latter and about 50 mb for the desired reaction, already a Tl-content of 10 ppm would contribute 50 % to the produced ^{204}Tl-activity. The natural lead was supplied as metal rods by Advent[3] with a certified Tl impurity below the detection limit of 0.1 ppm. The rods were rolled down to about 0.5 mm and then punched to disks of 13 mm diameter.

The enriched ^{206}Pb was supplied by Chemotrade[4]. About 100 mg metal was centered in a cardboard ring of 13 mm outer diameter and 5 mm inner diameter and fixed with adhesive tape.

Table 3.2: Isotopic composition of different lead samples

	^{204}Pb	^{206}Pb	^{207}Pb	^{208}Pb
natural range^a	1.65-1.04	27.48-20.84	23.65-17.62	56.21-51.28
representative^a	1.4(1)	24.1(1)	22.1(1)	52.4(1)
our sample^b	1.284(20)	27.12(26)	20.49(17)	51.11(24)
enriched ^{206}Pb^c	-	94.00	4.04	1.96

^{a}taken from [51]

^{b}measured with ICP-MS by IRMM, Isotopic Measurement Unit

^{c}given by the supplier

3.1.5 Monitor Foils

In, Ni, Al, Fe, Co, and Nb foils of 50-250 μm thickness and 13 mm diameter were used as reference samples (supplied by Goodfellow and Advent) and attached to the front and the back of the samples in a symmetric fashion. In cases of somewhat larger samples, additional monitor foils were inserted in the stack to monitor the flux gradient in the sample

---

[3] Advent Research Materials Ltd., Oakfield Industrial Estate, Eynsham·Oxon, England OX8 1JA

[4] Chemotrade Chemiehandelsgesellschaft mbH, 40239 Düsseldorf, Germany

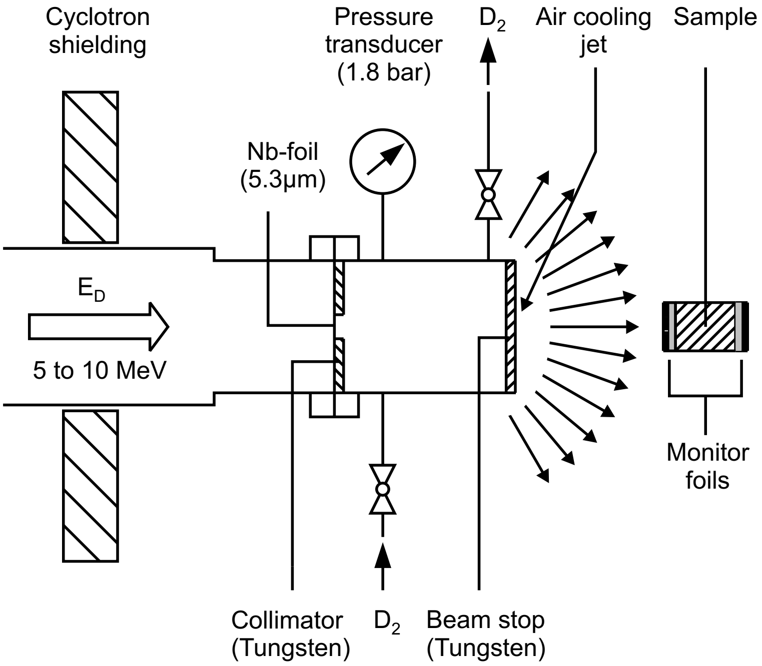

Figure 3.2: Sketch of deuterium gas target used at the CV-28 Cyclotron in Jülich, taken from [53]

3.2 Irradiations

Depending on the desired neutron energy three different neutron producing reactions and experimental setups were used.

Irradiations with neutron energies in the range of 0.5 to 6 MeV were done using the ^{3}H(p,n)^{3}He reaction (Q=-0.764 MeV, PT neutron field) with a solid-state Ti/T target while energies between 7.4 and 12.5 MeV were covered with the ^{2}H(d,n)^{3}He reaction (Q=3.269 MeV, DD neutron field) utilizing a D_2 gas target. Irradiations in the energy range from 13.4 to 20.5 MeV were performed using the ^{3}H(d,n)^{4}He reaction (Q=17.59 MeV, DT neutron field), again with a solid Ti/T target. A detailed description of the different setups is given below.

3.2.1 DD Neutron Field: D_2 Gas Target

At the Forschungszentrum Jülich, the variable energy Compact Cyclotron CV 28 was used to produce quasi-monoenergetic neutrons in the above mentioned energy range. A detailed description of the system, which is shown in Fig. 3.2, is given by Qaim *et al.* [53]. A collimated deuteron beam with energies between 5 and 10 MeV and a current of 4μA enters the gas cell via the 5.3 μm niobium foil, loses energy in this window and the deuterum gas and is finally stopped in the air cooled beam stop, made of tungsten [19]. The cell is made of 1 mm thick brass and has the dimensions of 3.7 cm in length and 4 cm diameter, filled with deuterium gas of 1.8 bar pressure. The target is insulated against the beam line and the integrated charge is recorded for each individual irradiation. Since the gas pressure and the current were largly stable during the irradiation, a constant neutron flux was assumed. The deuteron energy was measured by a time-of flight technique [54].

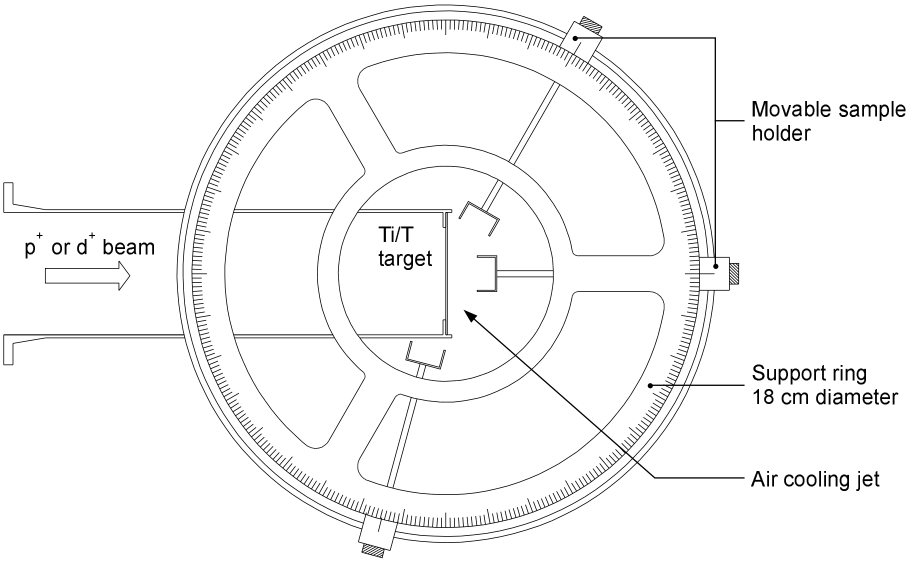

Figure 3.3: Sketch of the light mass setup target used at the Van de Graaff accelerator in Geel. A long counter is positioned at a distance of 6 m under an angle of 45°.

The samples were mounted together with the reference foils at 1 cm distance from the back of the beam stop using a scaled sample holder, which garanteed reproducible positioning of the sample. All irradiations were done at 0° direction relative to the incident beam. In order to be able to correct for background neutrons from the interaction of the deuterons with structural materials (entrance window, beam stop, cell, wall, etc.), two irradiations were necessary for each energy. One was performed with a filled cell (gas in) and one with an empty cell (gas out), but otherwise exactly the same geometry and beam conditions. A detailed description of this method can be found in [55].

3.2.2 PT and DT Neutron Field: Solid State Ti/T target

3.2.2.1 Setups

Depending on the half-life of the activation product under consideration, two different setups were used. Short irradiations involving half-lives between 1 and 5 minutes were done with a pneumatic sample transport system (“rabbit system”). For longer half-lives a light mass setup was used, that allows to place the samples at various angles and distances

The light mass setup Irradiations were performend at beam line L3 of the 7 MeV Van de Graff accelerator in Geel using a solid state Ti/T target. The target consists of a 1.923 mg/cm^2 Ti layer which is deposited on a 0.5 mm silver backing for good heat conduction. Tritium is diffused into the Ti layer at high temperatures until it is saturated at a value of 1.7 T atoms per Ti atom. This target is wobbled and cooled with a jet of compressed air to further aid in the dissipation of heat (<50 W). The energy scale is calibrated with an uncertainty of ±5 keV via a nuclear magnetic resonance system inserted in a 90° bending magnet, using well-known reaction thresholds and resonances.

For most irradiations a special designed light mass setup was used, which is shown in Figure 3.3. It consists of an Al ring of 18 cm diameter, which was mounted with it's center 10 cm above the nominal neutron source [56]. The samples were suspended from this ring using small Al sample holders. This setup allowed simultanous irradiations of several samples under different angles with respect to the incident deuteron or proton beam. Typical beam currents for all irradiations varied between 5 and 20 μA. For the determination of the production cross section for ^{94}Nb a special sample holder was constructed, which is shown in Fig. 3.1 (a) and (b). The fluctuations in the neutron flux were always monitord with a long counter operated in multichannel scaling mode (MCS). In addition to that the integrated beam current was recorded with a charge integrator.

The Pneumatic Tube System This setup uses the same neutron producing target system as the light mass setup described before, but on beam line R3 of the accelerator. A schematic diagram of the entire setup is shown in Fig. 3.4. The samples are placed in a small PVC container (the “rabbit”) using a lucite disk on the front side and a styrofoam plug on the back side (see Fig. 3.5). This ensures reproducible and secure positioning of the sample in the container. This container is then propelled through a stiff but flexible polyethylene tube (20 m long, 4 cm diameter) towards the target using compressed air and stopped by two steel wires. A commercial vacuum cleaner is used to retrieve the rabbit from the target. The last part of the tube is made of transparent lucite to permit a check of the sample-target distance with a video cammera. Either a Bonner sphere or a portable long counter was placed near the target and operated in multichannel scaling mode (MCS). One purpose was the monitoring of the neutron flux fluctuations during the irradiation. It also served as a reference fluence monitor, since the irradiation times were usually too short to build up enough activity in any monitor foil. For each given incident deuteron energy a longer irradiation of Al, Fe, and Nb foils was performed to calibrate the neutron detector.

PT Source Reaction For measurements in the threshold region of the ^{99}Tc(n,n'γ)$^{99\mathrm{m}}$Tc reaction the ^{3}H(p,n)^{3}He reaction was used to produce neutrons with energies between 0.5 and 6 MeV. The samples were mounted together with indium monitor foils under 0° at a distance of 20-30 mm. Incident proton energies varied between 1.5 and 6.8 MeV. Above 5 MeV a significant increase in background neutrons was observed. This is most likely due to proton-induced reactions on the backing material, e. g. ^{48}Ti(p,n)^{48}V ($Q = -4.795$ MeV). Therefore, for proton energies of 5.8, 6.3, and 6.9 MeV a second irradiation was performed with a similar target that did not contain any tritium. The recorded beam current served for normalization of the runs with and without tritium in the neutron producing target. A long-counter was used to monitor the fluctuations of the neutron flux.

DT Source Reaction The majority of the irradiations was done with incident deuteron energies of 1, 2, 3, and 4 MeV under 0° and a sample-target distance of 1 to 2 cm. This results in neutron energies ranging from 16.3 to 20.6 MeV. For energies between 13.4 and 16.3 MeV the angular distribution of the DT neutron source [58] was used with 1 MeV incident deuterons. The samples were mounted at angles between 60 and 120°

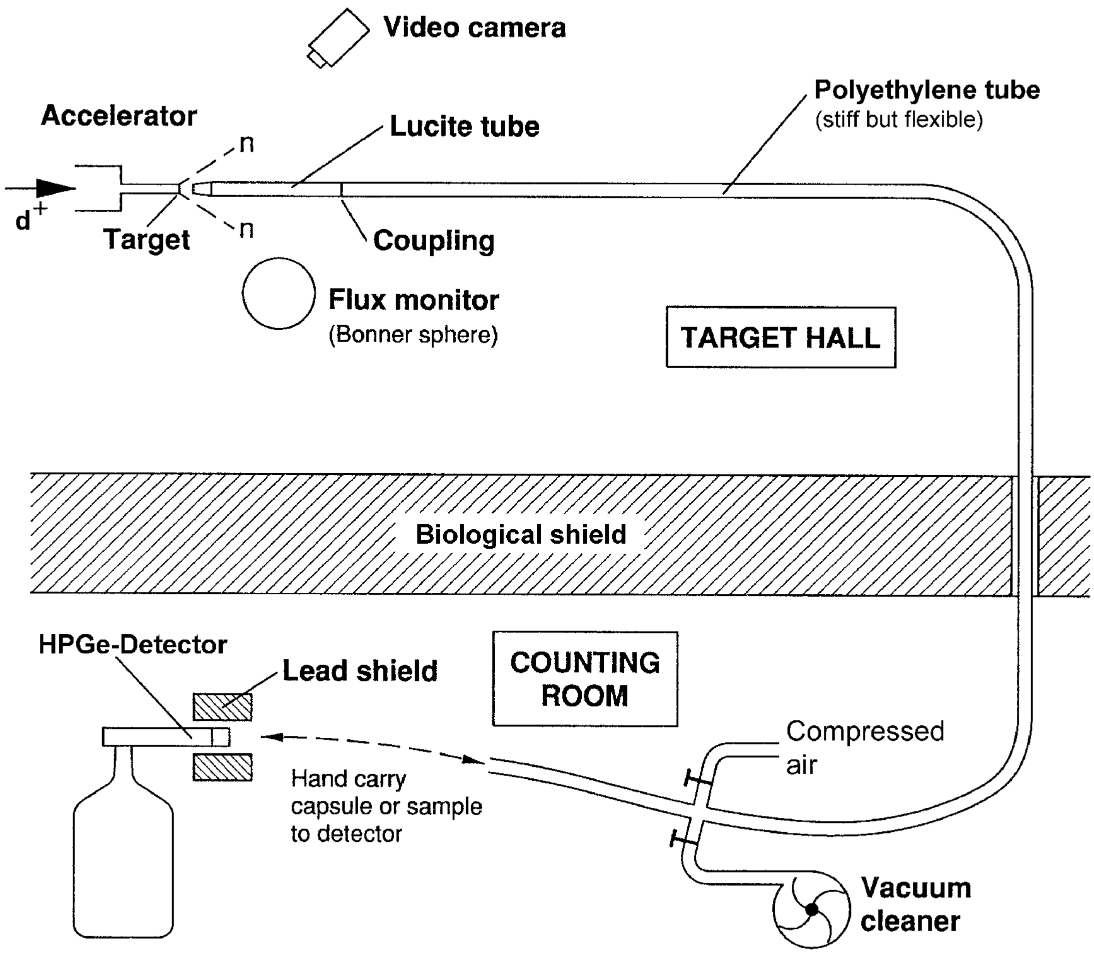

Figure 3.4: Schematic drawing of the pneumatic sample-transport system, taken from [57].

and a distance of 3.5 cm to the center of the target. The larger distance was due to the wobbling of the target can.

3.3 Neutron Fields

3.3.1 DD Neutron Field

Neutron Spectra The Monte Carlo program NEUT_HAV [59,60] was used to calculate the average neutron energy and the neutron spectrum for each sample in the DD neutron field. This code takes into account the energy loss, energy spread, and angular straggling of the deuterons in the entrance window of the cell, the neutron production within the volume of the gas cell, the angular distribution of the ^{2}H(d,n)^{3}He reaction [58], the breakup of the deuterons in the D_2 gas according to the results from [18], and the activation geometry.

The code calculates the average neutron energy and its uncertainty for each sample in the neutron field as well as the neutron spectrum for both the monoenergetic part and the breakup part of the spectrum. The spectra for the used incident deuteron energies are shown in part (b) of Figure 3.6.

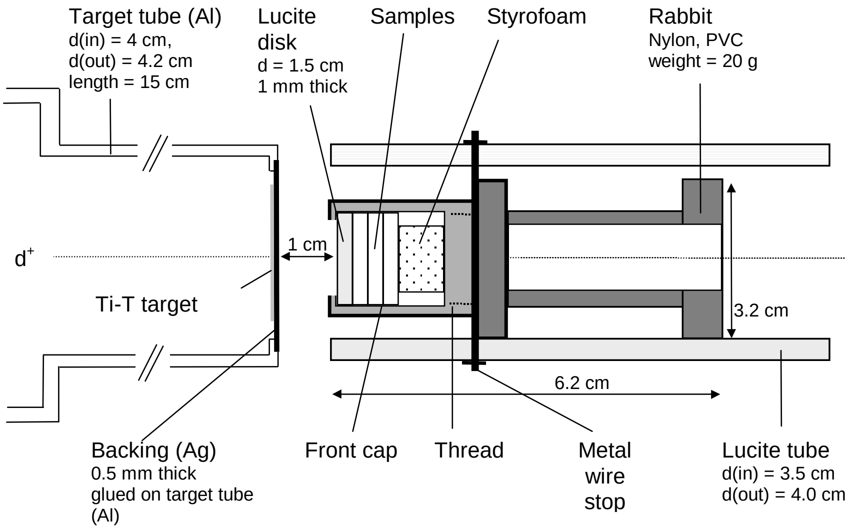

Figure 3.5: Schematic drawing of the transport-capsule (rabbit) in irradiation position.

Background Subtraction The advantage of a gas-target is the possibility to perform irradiations with or without gas filling. This allows to subtract the contributions to the neutron flux which stem from interactions of the incident deuteron beam with structural material. The correction factor c_{back} is given by

$$c_{back} = 1 - \frac{F_{out} \cdot q_{in}}{F_{in} \cdot q_{out}}. \tag{3-1}$$

Here q is the beam current integrated over the irradiation time and F is the molar reaction rate, which will be explained later (see Eq. 3-25, page 44). The indices refer to the gas-in or gas-out runs, respectively. Depending on the threshold and the shape of the excitation function the corrections could be rather substantial (cf. Table 3.3)

Breakup Correction While a proper choice of the structural materials for the entrance window and the beam stop as well as the quality of the deuterium gas help to obtain a

Table 3.3: Correction factors for background neutrons

Reaction	Incident Deuteron Energy (MeV)					
	9.91	9.04	8.10	6.90	5.94	4.81
Monitor reactions:						
^{115}In(n,n'γ)^{115m}In	0.70(2)	0.71(2)	–	–	–	–
^{58}Ni(n,p)^{58}Co	0.83(1)	0.83(1)	–	–	–	–
^{27}Al(n,p)^{27}Mg	0.78(1)	0.88(1)	0.92(1)	0.91(1)	0.94(1)	1
^{27}Al(n,α)^{24}Na	0.90(1)	0.97(1)	0.97(1)	0.96(1)	0.99(1)	1
other:						
^{99}Tc(n,n'γ)^{99m}Tc	0.47(3)	–	0.73(2)	0.71(2)	0.86(1)	0.93(1)
^{99}Tc(n,p)^{99}Mo	0.94(2)	0.97(1)	–	–	–	–
^{99}Tc(n,α)^{96}Nb	0.95(1)	0.98(1)	–	–	–	–

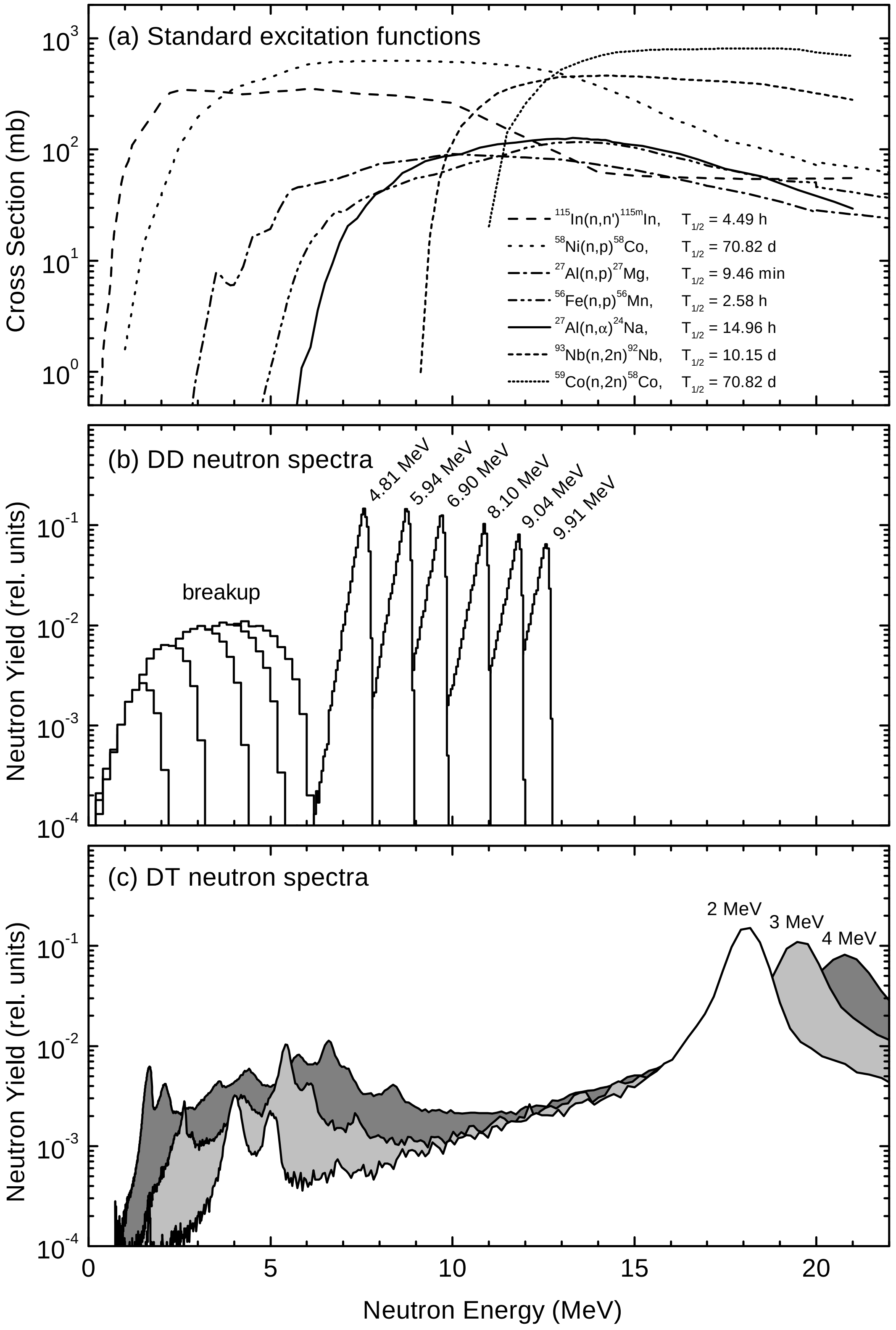

Figure 3.6: (a) Evaluated standard cross sections for the used reference reactions, taken from Refs. [61,62] (b) Neutron spectra calculated with the code NEUT_HAV [59] for incident deuteron energies between 5 and 10 MeV on the D$_2$ gas target at the Compact Cyclotron CV 28 at FZ Jülich (c) Neutron spectra for the Ti/T target at the Van De Graaff accelerator in Geel. The spectra were measured via TOF for 2, 3, and 4 MeV deuteron energy

Table 3.4: Correction factors for low-energy neutrons from the deuteron breakup

Reaction	Incident Deuteron Energy (MeV)					
	9.91	9.04	8.10	6.90	5.94	4.81
Monitor reactions:						
^{115}In(n,n'γ)^{115m}In	0.246(12)	0.371(15)	0.557(16)	0.782(10)	0.964(4)	1
^{58}Ni(n,p)^{58}Co	0.564(20)	0.701(18)	0.856(11)	0.965(4)	1	1
^{27}Al(n,p)^{27}Mg	0.844(13)	0.936(7)	0.984(2)	1	1	1
^{27}Al(n,α)^{24}Na	0.9995(1)	1	1	1	1	1
other:						
^{99}Tc(n,n'γ)^{99m}Tc	0.26(4)	–	0.54(5)	0.76(4)	0.97(1)	1

clean neutron spectrum, background of the breakup reaction D(d,pn)D (Q=-2.224 MeV) is unavoidable [63].

The necessary correction factor $c_{breakup}$ can be calculated using the simulated neutron spectrum and the shape of the excitation function:

$$c_{breakup} = 1 - \frac{A_{breakup}}{A_{total}} = 1 - \frac{\int_0^{E_{max}^{breakup}} \sigma(E) \cdot Y(E) \cdot dE}{\int_0^{E_{max}} \sigma(E) \cdot Y(E) \cdot dE}, \tag{3-2}$$

where $Y(E)$ is the relative yield of neutrons with the energy E and $\sigma(E)$ the cross section at this energy for the reaction under consideration. For the standard reaction the cross sections were taken from evaluations and for the cross section to be determined either from model calculations or estimated from measured data in energy regions where the breakup was still neglegible. The integrals were solved numerically by interpolating the neutron spectrum and the excitation function to the same energy grid. And as for the background subtraction, depending on the threshold and the shape of the excitation function the corrections could be rather substantial (cf. Table 3.4).

3.3.2 PT and DT Neutron Fields

Neutron spectra For both the PT and the DT neutron fields the program KINEMA was used to calculate the neutron energy $E(\theta)$ and yield $Y(\theta)$ at a given nominal angle θ. This program uses the cross section evaluation of LISKIEN *et al.* [58] and the stopping powers of ANDERSEN and ZIEGLER [64]. The mean energy $\overline{E}$ of a sample is calculated in the following way:

$$\overline{E} = \frac{\int_0^{\theta_{max}} E(\theta) Y(\theta) \theta d\theta}{\int_0^{\theta_{max}} Y(\theta) \theta d\theta}, \tag{3-3}$$

where θ_{max} denotes the maximum angle under which the neutrons strike the sample. For this angle and for 0° the energy and yield are calculated with the code KINEMA. Based on these values the angular dependence of neutron energy and yield were approximated with quadratic equations:

$$E(\theta) = E(0)(1 + a\theta^2) \quad \text{and} \quad Y(\theta) = Y(0)(1 + b\theta^2), \tag{3-4}$$

respectively. From this the two unknowns a and b can easily be derived and one finally obtains the mean energy:

$$\overline{E} = E(0)\frac{1 + \frac{1}{2}(a + b)\theta_{max}^2 + \frac{1}{3}ab\theta_{max}^4}{1 + \frac{1}{2}a\theta_{max}^2}. \tag{3-5}$$

For the uncertainty calculation the following expression was used:

$$< \overline{E} >^2 = \frac{\int_0^{\theta_{max}}(E(\theta) - \overline{E})^2 Y(\theta)\theta d\theta}{\int_0^{\theta_{max}} Y(\theta)\theta d\theta}. \tag{3-6}$$

For samples which were irradiated under an angle, like Tc and V, and for the massive Mo sample the Monte-Carlo Code MCNP [65] was used to calculate the spectra and thus the mean energy of the neutron impinging the sample. It takes into account the proper source description, the target can and the sample geometry including the holder. Taking into account the shape of the excitation function in a similar way as decribed for the breakup correction (cf. eq. 3-2) the multiple scattering corrections are obtained. They are only significant for low threshold reactions like ^{99}Tc(n,n'γ)^{99m}Tc, ^{115}In(n,n'γ)^{115m}In, and ^{58}Ni(n,p)^{58}Co, for which the correction factor $c_{scattering}$ can be up to 0.86 for incident deuteron energies of 4 MeV. For reactions with higher thresholds the corrections are negligible.

Figure 3.7 shows the distribution of the neutron flux as calculated for the large Mo sample. For each part of the sample three curves are shown, each representing the flux at the monitor position. The positions for the front disk are indicated in Figure 3.12. The neutron flux for the Mo samples was also obtained from the calculation, but is not shown in the plot to keep it more clear. It anyway coincides with the results for the center monitor. It can be seen that the flux decreases with distance from the neutron target. Since the mean angle is different for the monitor foils inserted in the rings, also an energy shift can be observed. The mean energy in the monitor foils of the front disk depends on the opening angle: for the outer monitor, which is farthest away the opening angle is the smallest and thus the mean neutron energy is the highest. The structure seen for the 2nd ring is not physical, but a result of the description of the neutron source. The neutron yield was calculated for a limited number of angles. Calculations for more angles would have given a smoother curve.

Background Subtraction For the DT neutrons time-of-flight (TOF) measurements of the neutron spectrum were performed for incident deuteron energies of 2, 3, and 4 MeV (see Fig. 3.6) to study the contribution of low-energy neutrons in detail. Earlier Measurements showed that contributions of low energy neutrons could be neglected for 1 MeV deuterons (See also [57]). A comparison of various spectra showed that the neutron spectrum changes from target to target and that the contributions from background

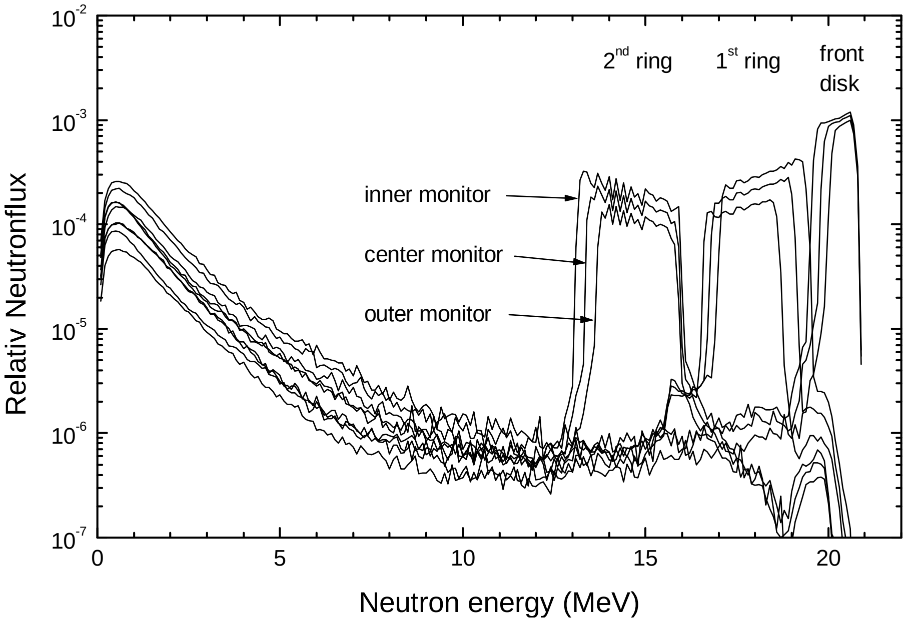

Figure 3.7: Neutron flux distribution in the large Mo sample, calculated with MCNP.

Table 3.5: Decay data (taken from [67]) and references of the used standard reactions

Nuclear Reaction	Half life of Product	Q-Value (MeV)	E_γ (keV)	Intensity (%)	Reference to Excitation Function
^{115}In(n,n'γ)^{115m}In	4.486(4) h	0	336.24	45.8(22)	SMITH *et al.* [61]
^{58}Ni(n,p)^{58}Co	70.86(7) d	0.401	810.78	99.45(1)	ENDF/B-VI.6 [30]
^{27}Al(n,p)^{27}Mg	9.458(12) m	−1.818	843.76	71.8(4)	ENDF/B-VI.6 [30]
^{56}Fe(n,p)^{56}Mn	2.5749(1) h	−2.913	846.75	98.9(3)	ENDF/B-VI.6 [30]
^{27}Al(n,α)^{24}Na	14.9590(12) h	−3.133	1369	100	WAGNER *et al.* [62]
^{93}Nb(n,2n)^{92m}Nb	10.15(2) d	−8.831	934.44	99.07(4)	WAGNER *et al.* [68]
^{59}Co(n,2n)^{58}Co	70.86(7) d	−10.453	810.78	99.45(1)	ENDF/B-VI.1 [30]

neutrons increase with time, due to tritium consumption and deuterium buildup. Since it is not practical to perform TOF measurements for every new experiment, a spectral index method was employed. This constitutes the use of a set of standard reactions with different excitation curves and, in particular, sufficiently different thresholds in order to help fix the actual low-energy neutron contributions. Figure 3.6 shows that the neutron flux may be divided in different groups according to their energy. The contributions of these different groups to the total observed flux were adjusted for each irradiation using the observed total molar reaction rates of the standard reactions. Since often the number of groups exceeds the number of useful monitor foils, a generalized least squares method [66] was employed that takes the results of the TOF measurements as the so-called prior values. The applied method guarantees that the peak-flux obtained from different monitor foils agrees within the uncertainties.

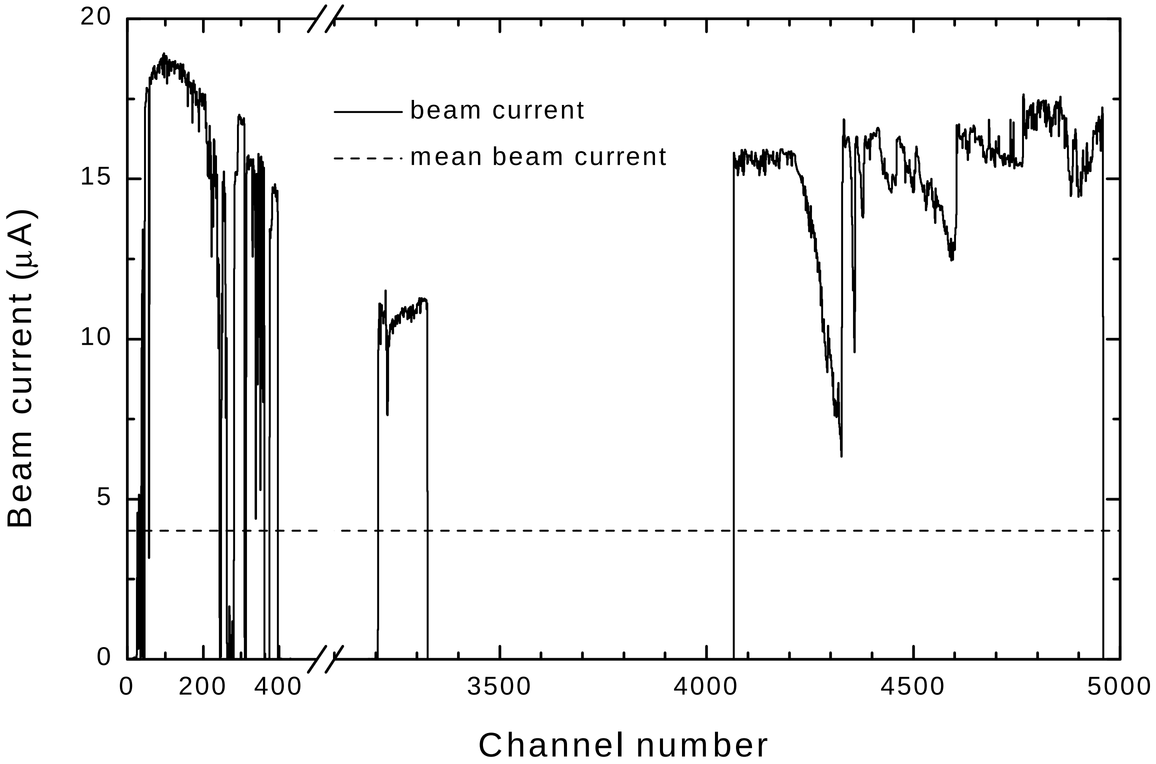

Figure 3.8: Neutron flux of the irradiation performed for the ^{nat}Mo(n,x)^{94}Nb cross section measurement. The total irradiation time was 410 h with an average beam current of 4 μA. Taking into account the interruptions and maintenance breaks, an effective irradiation time of 110 h with a mean beam current of 15 μA is obtained.

3.3.3 Fluctuations in the Neutron Flux

The basic activation formula (Eq. 1-8, page 6) assumes a constant neutron flux during the time of irradiation. Due to fluctuations in the proton or deuteron beam intensity it is not always the case. Depending on the time profile of the flux fluctuations and the half-life compared to the irradiation time, the corrections can be rather substantial. For the irradiations in Geel the neutron flux was monitored directly using either a long counter or a Bonner sphere, operated in multichannel-scaling acquisition mode (MCS). The dwell time Δt was set according to the planned irradiation time and varied between 1 sec and 5 min. Figure 3.8 shows an example of a recorded MCS spectrum. Additionally the beam current was recorded using a charge integrator, which was the only possibility in Jülich.

The correction factor c_{flux} for flux fluctuations can be calculated from the ratio

$$c_{flux} = \frac{\overline{\Phi} \cdot (1 - e^{-\lambda t_i})}{\sum_{i=1}^{n} \Phi_i \cdot (1 - e^{-\lambda \Delta t}) \cdot e^{-\lambda (n-i) \Delta t}}, \tag{3-7}$$

where $\overline{\Phi}$ is the mean flux of the irradiation, Φ_i the flux at the time bin i, n the number of total time bins, t_i the irradiation time and Δt the dwell time of the MCS.

3.4 γ-Ray Spectroscopy

Standard γ-ray spectroscopy was employed for the measurement of the radioactivity. Due to its very low count rate the ^{94}Nb activity was measured in the underground laboratory HADES, which will be explained in section 3.4.6, page 38.

3.4.1 Data Acquisition

In total five lead-shielded HPGe detectors were used for the off-line measurement of the radioactivity, two (No. 6 and 8) in Jülich, and three (No. 1, 2, and 4) in Geel. They were connected to personal computer data aquisition systems via separate analog-to-digital converters (ADC). The detectors in Jülich were controlled with the program GAMMAVISION (EG&G Ortec), whereas in Geel the S100 software (Canberra) and the MAESTRO software (EG&G Ortec) were used.

In order to obtain maximum count rates and thereby reasonable counting statistics, the monitor foils were placed directly on the detector cap and fixed with adhesive tape. Most of the samples were counted in the same way, but for the Pb and Tc samples special geometries were chosen.

In the case of Pb this was not always possible, since the self-absorbtion was too high for some γ-rays, e.g. the 279 keV line from $^{203\mathrm{g}}$Pb (cf. Table 3.6). For irradiation 12 disks of 10 mm diameter or 7 disks of 13 mm were used in a stack, but for the γ-ray spectroscopy they were placed in one layer next to each other on the detector cap.

The Tc samples could not be counted directly on the detector cap, since the Bremsstrahlung caused high dead time of the detector. Measurements of the ^{99}Mo yield via the 739.5 keV γ-ray and ^{96}Nb yield via the 569.9 keV γ-ray were possible by inserting a 2 mm Pb sheet between the sample and the detector. The lead sheet suppressed the Bremsstrahlung sufficiently without a substantial reduction of the detection efficiency. The strongest γ-ray line of ^{96}Nb (778.2 keV, see Table 3.6) was not used, since it overlaps with the 777.9 keV γ-ray of ^{99}Mo. The yield of $^{99\mathrm{m}}$Tc was measured via the 140.5 keV γ-ray at 20 or 30 cm distance without lead absorber (Jülich) or at 7.5 cm with only 1 mm of lead to shield the detector (Geel). This activity was measured directly after end of irradiation to avoid buildup of additional activity via the decay of ^{99}Mo.

3.4.2 Spectrum Analysis

The spectra recorded with the MAESTRO and GAMMAVISION software were in both cases analysed with GAMMAVISION. The peaks are marked with a region of interest (ROI), including a few channels to the left and the right of the peak. The program calculates the background based on the first and last three channels of the ROI and substracts it from the gross count rate to obtain the net peak area. The program GAMMA-W[5] [69] was used to analyse the γ-spectra measured in Geel. The program calculates the background in a marked region. The peaks on top of this background are then fitted with a Gaussian function by a least-squares method.

---

[5] Dr. Westmeier, Gesellschaft für Kernspektrometrie mbH, Ebersdorfergrund-Mölln, Germany

Table 3.6: Decay properties (taken from [67]) and summing correction factors of the studied activation products. The summing correction factors are calculated for the used detectors as described in section 3.4.5, page 36, if not indicated differently

Nucleus	Half-life	Decay mode	γ-ray (keV)	Intensity (%)	Summing Geel-1	Summing Geel-2	Summing Geel-4
^{47}Sc	3.3492(6) d	100% β^-	159.4	68.3(4)	1	1	1
^{48}Sc	43.67(9) h	100% β^-	983.5	100.1(6)	N/A	N/A	1.56(11)^a
^{51}Ti	5.76(1) min	100% β^-	320.1	93.1(4)	1.002^d	N/A	N/A
^{99m}Tc	6.01(1) h	99.996% IT, 0.004% β^-	139.5	89.06(24)	N/A	N/A	1
^{91m}Mo	64.6(6) s	49.9% β^++EC, 50.1% IT	652.9	48.2(22)	1	1	1
^{93m}Mo	6.85(7) h	99.88% IT, 0.21% β^+	684.7	99.7(20)	1.38(5)	1.43(6)	1.34(7)^a
^{99}Mo	65.94(1) h	100% β^-	739.5	12.13(22)	1.13(1)	1.13(1)	1.14(8)^a/1.00(6)^{a,c}
^{92m}Nb	10.15(2) d	100% β^++EC	934.4	99.07(4)	1	1	1
^{94g}Nb	20.3(16)$\cdot 10^3$ a	100% β^-	871.1	99.9	N/A	N/A	1.2^b
^{95m}Nb	86.6(8) h	94.4% IT, 5.6% β^-	235.9	24.9(8)	1	1	1
^{95g}Nb	34.975(7) d	100% β^-	765.8	99.81(3)	1	1	1
^{96}Nb	23.35(5) h	100% β^-	568.9	58.0(3)			1.66^a/1.55^{a,c}
^{97m}Nb	58.7(18) s	100% IT	743.4	97.90(6)	1	1	1
^{97g}Nb	72.1(7) min	100% β^-	657.9	98.23(8)	1	1	1
^{98m}Nb	51.3(4) min	99.9% β^-, <0.2% IT	787.4	93.4(2)	1.34(9)	1.42(12)	1.58(8)^a
^{89m}Zr	4.161(17) min	6.23% EC+β^+, 93.77% IT	587.8	89.64(19)	1	1	1
^{95}Zr	64.02(5) d	100% β^-	756.7	54.46(10)	1	1	1
^{97}Zr	16.744(11) h	100% β^-	743.4	93.06(16)	1	1	1
^{202m}Pb	3.53(1) h	90.5% IT, 9.5% EC	960.7	92.(8)	1.21(8)		1.39(9)^a
^{203g}Pb	51.873(9) h	100% EC	279.2	80.80(20)	1.10(5)		1.20(6)^a
^{204m}Pb	67.2(3) min	100% IT	899.2	99.17(2)	1.40(6)		1.44(6)^a
^{204}Tl	3.78(2) a	97.1% β^-, 2.9% EC+β^+		no γ-rays, $E_{\beta^-}^{max}$=764 keV			
^{203}Hg	46.612(18) d	100% β^-	279.2	81.46(13)			1
Monitor reactions							
^{24}Na	14.9590(12)h	100% β^-	1368.6	100.0	1.07(3)^d		1.25(4)^a
^{27}Mg	9.458(12) min	100% β^-	843.7	71.8(4)	1	1	1
^{58}Co	70.86(7) d	100% EC+β^+	810.8	99.45(1)	1.08		1.03(4)^a
^{56}Mn	2.5785(2)h	100% β^-	846.8	98.9(3)	1.04(3)^d		1.12(5)
^{115m}In	4.486(4) h	95% IT, 5% β^-	336.2	45.8(22)	1	1	1

[a] experimentally determined, [b] total efficiency calculated with MCNP, [c] with 2 mm Pb absorber, [d] taken from [57]

Table 3.7: Decay properties of the γ-ray standard sources, taken from [67]

Nuclide	$T_{1/2}$	E_γ (keV)	Intensity (%)
^{241}Am	432.2(7) a	59.54	35.9(6)
^{109}Cd	461.4(12) d	88.03	3.7(1)
^{57}Co	271.74(6) d	122.06	85.60(17)
		136.47	10.68(8)
^{139}Ce	137.640(23) d	165.85	79.886(15)
^{113}Sn	115.09(03) d	391.70	64.97(17)
^{85}Sr	64.83(4) d	514.01	96.(4.)
^{137}Cs	30.07(3) a	661.66	85.1(2)
^{54}Mn	312.11(5) d	834.85	99.976(1)
^{65}Zn	244.26(26) d	1115.55	50.60(24)
^{60}Co	5.2714(5) a	1173.24	99.9736(7)
		1332.50	99.9856(4)

3.4.3 Detector Efficiency and Energy Calibration

Peak Efficiency Since the peak count rate in the the γ-ray spectrum is used to determine the activity of the sample, the photopeak detection efficiency for the same counting geometry is required. For this purpose and for the energy calibration of the detector several calibrated single and multi γ-ray point sources supplied by PTB[6] and DAMRI[7] were used. In the case of ^{60}Co where two photons are emitted in cascade, summing out corrections were applied (see section 3.4.5). The decay properties of the used sources are summarized in Table 3.7.

For each γ-ray energy E_γ and source-detector distance x the photopeak efficiency ϵ_{ph} was calculated using the following equation:

$$\epsilon_{ph}(x, E_\gamma) = \frac{Y_{ph}(x, E_\gamma)}{A_0 \cdot b_\gamma \cdot e^{-\lambda t}}, \tag{3-8}$$

where $Y(x, E_\gamma)$ is the number of measured γ-rays with the energy E_γ at the given distance, A_0 is the activity of the source at time of standardization, b_γ is the γ-ray branching factor, λ the decay constant and t the elapsed time since standardization.

The following analytical function, proposed by Jäckel *et al.* [70] was used to fit the energy dependence of the photopeak efficiency for each used measurement distance:

$$\ln \epsilon(E_\gamma) = \left(a_1 + a_2 \ln E_\gamma + a_3 \ln E_\gamma^2\right) \cdot \tfrac{2}{\pi} \cdot \arctan\left(\exp\left\{a_4 + a_5 \ln E_\gamma + a_6 \ln E_\gamma^2\right\}\right) - 25. \tag{3-9}$$

Total Efficiency The total efficiency ϵ_t is defined as the ratio of the number of pulses recorded in the entire spectrum to the number of photons emitted from a source [71].

---

[6] Physikalisch Technische Bundesanstalt, Braunschweig, Germany

[7] Departement des Application et de la Metrology des Rayonnements Ionisant, 91193 Gif-sur-Yvette

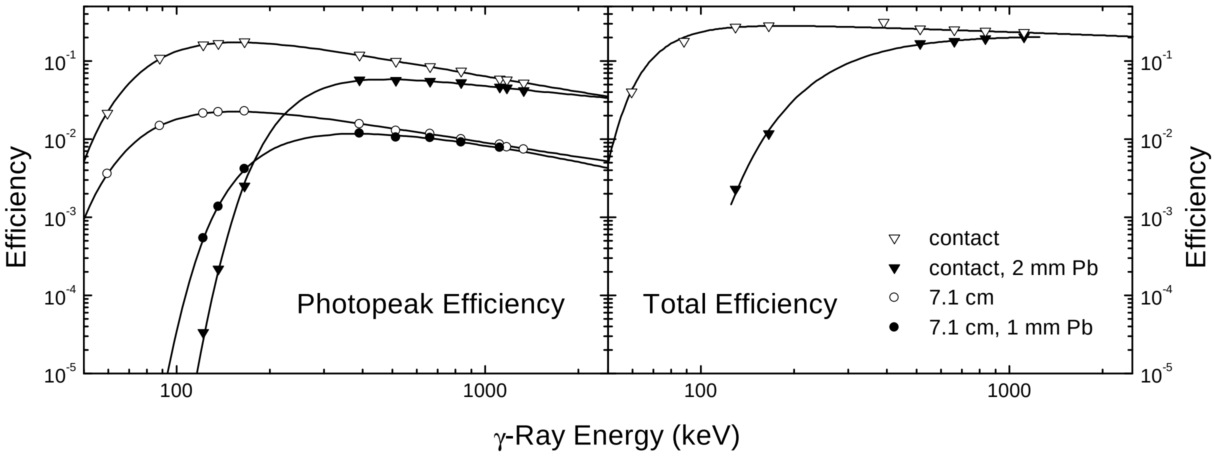

Figure 3.9: Photopeak and total efficiency of detector Geel-4 for the contact position and for position 5 (7.1 cm source-detector distance). Also shown is the effect of inserting Pb sheets of 1 or 2 mm thickness between source and detector, which was necessary for the Tc measurements. The solid lines represent a fit to the measured data, calculated with Eq. 3-9.

The calculation of the total efficiency can be done similar to the peak efficiency:

$$\epsilon_t(x, E_\gamma) = \frac{Y_t(x, E_\gamma)}{A_0 \cdot b_\gamma \cdot e^{-\lambda t}}, \tag{3-10}$$

but this time using the total count rate Y_t in the spectrum, which has to be extrapolated to zero keV γ-ray energy and corrected for natural background. The single γ-ray emitters listed in Table 3.7 were used for this calibration. ^{57}Co, which emits two photons with energies close to each other, was also used, but the sum of the individual emission probabilities was inserted in equation 3-10 and ϵ_t was assigned to the mean energy, i. e. 129.3 keV. The obtained data were fitted with the same analytical function as the peak efficiency (3-9).

Radial Efficiency The correction for extended sources (see next section) also requires the knowledge of the radial efficiency of the Ge detector. It was determined by measuring a standard point source at an off center distance r and calculating the peak efficiency $\epsilon_{ph}(r)$ for this position. Figure 3.10 shows the ratio of the measured efficiencies for a ^{54}Mn point source. The data were fitted with a 4th order polynominal function.

3.4.4 Efficiency Corrections for Extended Sources

Since the above efficiency calibration was done with point sources, corrections are needed for the extended samples used in the irradiations. These corrections include self-absorption in the sample, inhomogeneity of the activity due to the neutron flux gradient and both the distance and the radial dependence of the efficiency.

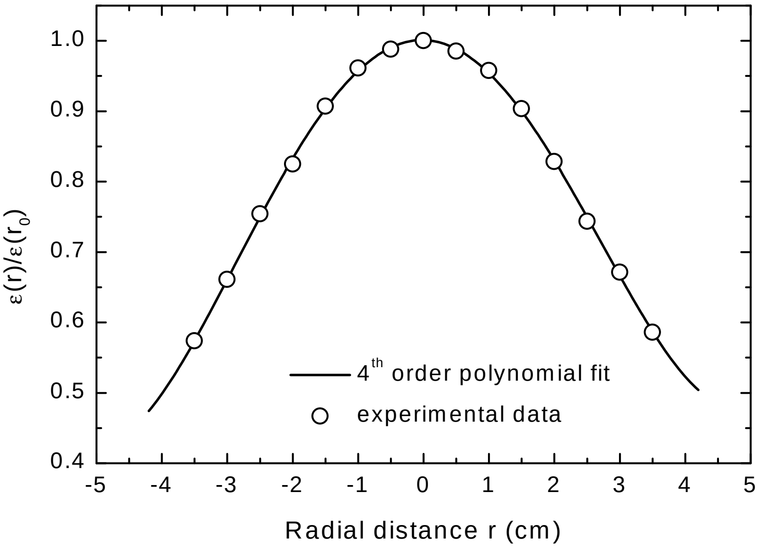

Figure 3.10: Radial dependence of the detector efficiency (Geel-4), measured with a ^{54}Mn standard source (834.9 keV) at contact position.

Photon Absorption Assuming a homogeneous distribution of both the attenuating material and the activity, the transmission T through a sample of a thickness X (cm) and density ρ (g/cm^3) is given by

$$T = e^{-\mu\rho X}. \tag{3-11}$$

The absorption coefficient μ, given in cm^2/g was calculated with the program XCOM [72]. The mean transmission $\overline{T}$ results in:

$$\overline{T} = \frac{1}{x}\int_0^X e^{-\mu\rho x}dx = \frac{1}{\mu\rho X}(1 - e^{-\mu\rho X}) \tag{3-12}$$

The correction factor for self absorption is finally defined as

$$c_{abs} = \overline{T}^{-1} = \mu\rho X(1 - e^{-\mu\rho X})^{-1}. \tag{3-13}$$

For the molybdenum measurements, where a 1.4 cm thick sample was used, the attenuation was checked experimentally. For this purpose a ^{152}Eu standard source was mounted at a fixed distance from the detector cap and 0 to 8 Mo sheets of 2 mm thickness were inserted between source and detector. The transmission T is then obtained as the ratio of the measurements with absorber to the one without. The results of these measurements and a comparision with the values calculated with the program XCOM are given in Figure 3.11. The measurement and calculation agreed within 3%.

Disk Sources Most irradiations were done using samples with a diameter of 10 or 13 mm. For those small samples a homogenous activity distribution was assumed. Taking

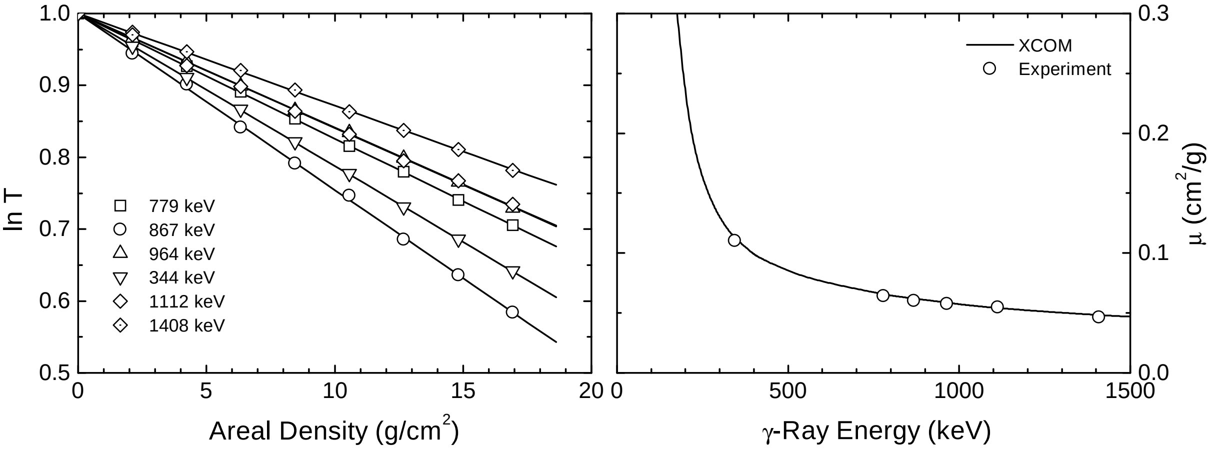

Figure 3.11: The left part of the figure shows the transmission of several γ-ray lines of ^{152}Eu through metallic molybdenum. A comparison of the experimentally determined attenuation coefficients μ with the XCOM results is shown in the right part.

into account only the radial efficiency dependence and neglecting self absorption, the correction factor can be calculated as follows:

$$c_{disk} = \frac{\int_0^R \epsilon(r) 2\pi r dr}{\int_0^R \epsilon(0) 2\pi r dr} = \frac{\int_0^R \frac{\epsilon(r)}{\epsilon(0)} r dr}{\int_0^R r dr} = \frac{2}{R^2} \int\limits_0^R \frac{\epsilon_{ph}(r)}{\epsilon_{ph}(0)} r dr. \tag{3-14}$$

Since the neutron energy and yield of the ^{3}H(d,n)^{4}He reaction are angular dependent, the assumption of a homogeneous activity distribution in the sample is not valid for large disk sources. For the efficiency correction of a disk source both the radial dependence of the efficiency $\epsilon(r)$ and the activity distribution $a(r)$ is needed.

$$c_{disk} = \frac{\int_0^R \epsilon(r) a(r) 2\pi r dr}{\int_0^R \epsilon(0) a(r) 2\pi r dr} = \frac{\int_0^R \frac{\epsilon(r)}{\epsilon(0)} \sigma(r) \Phi(r) r dr}{\int_0^R \sigma(r) \Phi(r) r dr}. \tag{3-15}$$

The integral is solved numerically by subdividing the circular sample in concentric rings of width Δr. For each ring and its respective angle the energy and neutron yield Y were calculated with the code Kinema. In order to get the neutron flux in the ring under consideration, it's actual distance from the neutron source has to be taken into account:

$$\Phi(r) = \frac{Y(r)}{d^2 + r^2}, \tag{3-16}$$

where d is the distance between target and sample under 0°.

Volume Sources For not too thick sources the activity gradient in x direction can be neglected and one obtains the correction factor as a simple product of equations 3-13 and 3-14 or 3-15, respectivly, depending on the diameter..

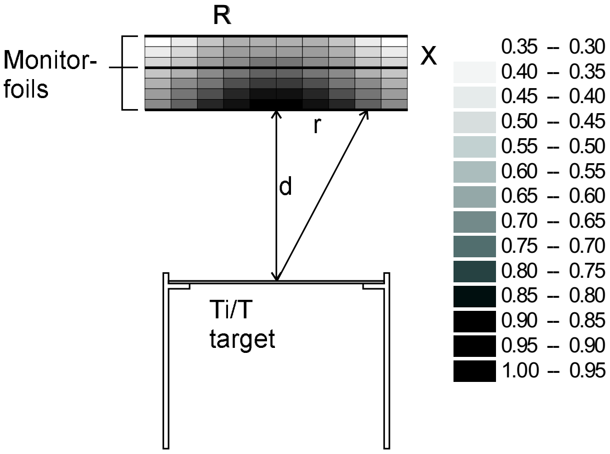

Figure 3.12: A section through the 5 cm diameter and 1.4 cm thick Mo sample, showing the calculated activity distribution. The sample was irradiated under 0° and at 31 mm distance from the Ti/T target

$$c_{vol} = c_{abs} \cdot c_{disk} \tag{3-17}$$

A thicker volume source can be treated as a multi layered disk source, with the additional complication due to self absorption in the sample and an activity gradient in the x direction.

$$c_{vol} = \frac{\int_0^X \int_0^R e^{-\mu\rho x}\epsilon(x,r)a(x,r)drdx}{\epsilon(0)\int_0^X \int_0^R a(x,r)drdx} \tag{3-18}$$

The integrals are again solved numerically by subdividing the cylindrical source in several layers of thickness Δx containing rings with a width of Δr. For each ring the activity is calculated as described for the disk sources but taking into account the activity gradient in the x direction, which was obtained from monitor foils inserted in the stack. Figure 3.12 shows the activity distribution calculated for the front disk in the molybdenum experiment. The efficiency $\epsilon(x,r)$ can be expressed as $\epsilon(x) \cdot f(r)$, whereby it is assumed that $f(r) = \frac{\epsilon(r)}{\epsilon(0)}$ is independent of x.

3.4.5 Coincidence Summing

Coincidence summing corrections can be necessary when a radionuclide emits two or more photons within the resolving time of the detector [73]. When the first photon γ_1 with the energy E_{γ_1} deposits all its energy in the Ge crystal and if a second photon γ_2 with E_{γ_2} is also detected, a sum pulse is recorded at the energy $E_{sum} = E_{\gamma_2} + E_{\gamma_2}$. Since in this scenario some count rate is lost for the first peak, one speaks of a summing out effect.

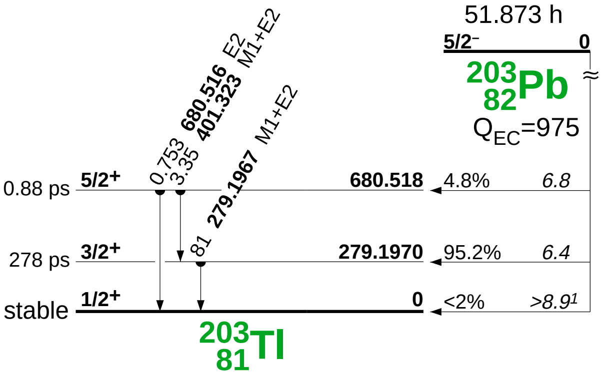

Figure 3.13: Decay scheme of ^{203g}Pb to illustrate the summing coincidence corrections, taken from [74]

The magnitude of the corrections depends on the probability with which the second photon is also detected, i. e. it's total efficiency ϵ_T. That means that the correction depends on the source-detector distance but is independent of the count rate.

If there happens to exist a transition with the same energy as the summing peak, the observed count rate for this photon is too high and one speaks of a summing in effect. The summing in corrections are generally much smaller than the summing out corrections since they depend on the peak efficiencies of the two photons.

The preferred way to determine the summing correction factors would be experimentally. The radioactive sample is counted once in the usual counting geometry, which is directly on the detector cap, and for a second time at a far distance, where summing effects are negligible.

In the majority of the cases it is not possible to measure the correction factors, since the activity of the source is not strong enough to give good count rates at the far position. Due to this most of the corrections were calculated, which will be explained using the simple decay scheme of ^{203g}Pb, Figure 3.13.

Summing out The count rate of peak 1 without summing effects is given by $n_1 = Ap_1\epsilon_1$, where A is the source activity, p_1 the emission probability for γ_1 and ϵ_1 the peak efficiency for γ_1. Since each γ_1 is followed by a γ_2 in coincidence, the observed count rate n_1' is then given by

$$n_1' = Ap_1\epsilon_1 - Ap_1\epsilon_1\epsilon_{t_2}, \tag{3-19}$$

since the probability of counting γ_2 is equal to its total efficiency ϵ_{t_2}. Taking into account equation 3-8 we derive the correction factor:

$$c_{in}^{\gamma_1} = (1 - \epsilon_{t_2})^{-1}. \tag{3-20}$$

The situation for peak 2 is different, since a fraction of γ_2 is not preceded by γ_1. Here we get:

$$c_{in}^{\gamma_2} = \left(1 - \frac{p_{\gamma_1}}{p_{\gamma_2}} \epsilon_{t_1}\right)^{-1}. \tag{3-21}$$

Summing in Summing of γ_1 and γ_2 leads to additional events in peak 3, which occurs with the probability $p_{\gamma_1}\epsilon_{ph_1}\epsilon_{ph_2}$. The correction factor is then given by

$$c_{out}^{\gamma_3} = \left(1 + \frac{p_{\gamma_1}\epsilon_{ph_1}\epsilon_{ph_2}}{p_{\gamma_3}\epsilon_{ph_3}}\right)^{-1}. \tag{3-22}$$

In cases where more γ-rays are emitted in cascade, the calculation becomes more complicated, but the principle is the same. Coincidences with 511 keV annihilation γ-rays are taken into account using the following equation:

$$c_{annihilation} = \left(1 - 2 \cdot \epsilon_T^{511}\right)^{-1}. \tag{3-23}$$

3.4.6 Ultra Low-level γ-ray Spectroscopy at HADES

The Mo samples irradiated in the two-ring geometry, described in section 3.1.2, were first measured with the conventional, but well shielded Ge detector system, which was used for all other measurements done during this work. Since the combination of bad counting statistics and high background gave a result with an unsatisfying uncertainty, a new measurement was done in the underground laboratory HADES. It is operated by the Radionuclides Group of IRMM in the Belgian national underground research facility at SCK/CEN, Mol. The laboratry is situated at 223 m under ground and thus practically free of cosmic rays.

The samples were all measured on the same well characterised coaxial high purity Ge detector with 106% relative efficiency. This detector has extremely low background characteristics. The Ge-crystal is built in a ultra low-background U-style cryostat made from selected radiopure materials. It is shielded using 11 cm of freshly produced electrolytic copper and 15 cm of ultra low-background lead. The lead is divided into 2 layers. The innermost 5 cm contains less than 3 Bq/kg of ^{210}Pb and the outer 10 cm contains less than 20 Bq/kg of ^{210}Pb. The sample volume is flushed with N_2 boiling off the liquid nitrogen dewar in order to minimise the contribution of Rn to the measurement. For other recent measurements done at HADES see Ref. [75].

For this measurement the 7 cubic samples, which were exposed to the same neutron field, were placed next to each other on top of the cryostat window of a HPGe detector and counted for a period of 2 and 4 weeks, respectively. A 2 mm thick teflon sheet protected the corbon composite window of the detector. For a detailed view of the irradiating and counting geometry see Figure 3.1. A Mo sample of the same material batch, but not irradiated, was also measured at HADES, in order to indentify background peaks. An overview over the performed measurements in HADES is given in Table 3.8. The result of the measurement done for the front disk above ground is also given for completeness.

The detector efficiency was modeled using the EGS4 Monte Carlo program approximating the irregular sample shape with a cylinder shape. The code further takes into account the activity gradient in the sample obtained from monitor foils and manufacturer's information on measurable detector dimensions. The values of Ge dead-layer and crystal position were derived from experimental mesurements using standard point sources (see Table 3.7). The decay scheme of ^{94}Nb was used in EGS4 in order to calculate the full peak efficiency taking into account summing coicidences.

3.5 Low Level β Counting

For the determination of the activity via low level beta counting a thin sample is needed, so that self absorption of the β^-particles in the sample is minimised. In the case of the ^{204}Tl measurement thick Pb samples were irradiated, thus requiring a chemical separation of the product and thin sample preparation prior to counting. The method used in this case is described below (see Section 3.7.1). ^{204}Tl has a half-life of 3.78 years and a β^- endpoint energy of 764 keV (cf. Table 3.6, page 31).

3.5.1 Counting System

The β^--detecting system is composed of the main electronics unit, the detector, a guard detector and a Pb shielding cavity. The electronics unit consists of preamplifier, amplifier, discriminator, anticoincidence circuit, high voltage supply, scaler and timer. The low background given by the Pb shielding is further reduced by the anticoincidence shielding system. A guard counter surrounds the detector, and any counts coincident with the counts in the guard detector are rejected by the electronics.

Since the intensities of the ^{204}Tl samples were expected to be low, a 2π geometry counter was used to be able to obtain maximum couting statistics. The 2π counter was a thin window gas flow counter. The samples were placed in aluminum planchets, which were mounted on a sample holder. The sample holder could hold a maximum of 10 samples at a time and could be slided into the counter. A continuos flow of 90% methane and 10% argon (P10 gas) was used to remove the air inside the counter. In order to obtain a stable background the detector has to be flushed with P10 gas for several hours before the actual measurement. Before the measurement the beta plateau had also to be determined, i. e

Table 3.8: Overview of the Mo measurements in HADES and the van de Graaff laboratory (VdG).

Sample	Detector	Cooling time (d)	Live time (d)	Activity (mBq/g)
blank disk	HADES	n.a.	7.0	0.0
1^{st} ring	HADES	726	6.8	0.048(5)
	HADES	891	28.4	
2^{nd} ring	HADES	1077	6.8	0.0216(25)
	HADES	930	14.5	
front disk	VdG	234	12.8	0.068(16)

the operating voltage, at which the count rate is independent of the applied high voltage.

3.5.2 Efficiency

In principal the determination of the detector efficiency is done in the same way as for a Ge γ-ray detector. A list of suitable beta emitting standard sources is given in Table 3.9.

Table 3.9: Decay properties[a] of standard beta sources

Standard Source	$T_{1/2}$ (years)	$E_{\beta^-}^{max}$ (keV)	Intensity (%)
^{14}C	5730(40)	156	100
^{210}Bi	22.3	1161	100
^{36}Cl	$3.0 \cdot 10^5$	709	98.1
^{99}Tc	$2.1 \cdot 10^5$	292	100
^{147}Pm	2.623(1)	225	100

[a] given by the supplier: New England Nuclear, 549 Albany Street, Boston, Mass. 02118, USA

3.5.3 Corrections

In general, several corrections have to be applied to the measured count rate obtained by the low level beta counting of thin samples. These are scattering and backscattering effects, absorption and self absorption.

Scattering and backscattering effects strongly depend on the geometry and the materials used in the measuring apparatus, since scattering takes place on the source holder, internal walls of the detector, etc. It can be significantly reduced by the use of light elements. The sample holder used in the measurements was a thin walled Al planchet.

Further corrections are necessary for absorption in the air between the sample and the window, but this is only a minor effect for β^--energies above 300 keV. Absorption also occurs in the detector window, for which Mylar is the recommended material.

The biggest problem in the determination of ^{204}Tl activity is the self absorption in the sample itself [76]. It also limits the use of $4\pi\beta$-counting of solid sources, emphasising the importance of the source preparation. It was tried to minimise the self-absorption by adding as less carrier as possible in the chemical separation procedure and subsequent thin sample preparation, but due to the relative inhomogeneity of the prepared sample it was not possible to correct for this effect in a reliable way. It was thus decided to measure the ^{204}Tl activity via Liquid Scintillation Counting (LSC), where self absorption does not play a role.

3.6 Liquid Scintillation Counting (LSC)

The ^{204}Tl measurements using Liquid Scintillation Counting (LSC) were performed at the Radionuclides Group of the Institute for Reference Materials ans Measurements.

3.6.1 Apparatus and Measurement

Measurements were performed with the Wallac Quantulus 1220 ultra low level Liquid Scintillation Counter, operated at about 12–13 °C. The thin samples, previously prepared for measurements with proportional counter, were dissolved in HCl and the solution was evaporated to about 2 ml in a Packart vial. A precipitate was formed, which required adding 7 ml of 1 M HCl and heating, before 10 ml of the scintillation cocktail could be added. Insta Gel Plus supplied by Packart Instruments was used as scintillation cocktail. On inserting the liquid sample into the cooled apparatus the solution became an almost solid gel. Each sample was counted three times for 300 min and the individual measurements combined. The results were corrected for background by couting a sample containing only 7 ml 1 M HCl and 10 ml Insta Gel. The filter paper, that carried the thin samples before, was also measured, in order to check that the sample was completely dissolved. Only negligible traces of ^{204}Tl were detected. For this measurement the cocktail Ultima Gold^{TM} was used, also supplied by Packart Instruments.

3.6.2 Efficiency

The efficiency versus quench parameter (Tranformed Spectral Index, tSIE) curve was established using the CIEMAT/NIST ^{3}H efficiency tracing method described by GRAU MALONDA and GARCIA-TORAÑO [77,78]. It is a combination of theoretical calculation of the counting efficiency and an experimental determination of correction factors with the help of a tracer nuclide, e. g. ^{3}H, sensitive to quenching effects due to its low β-particle energy.

Due to the rather high acidity of the Tl-samples, a dedicated ^{3}H calibration had to be done, in order to compensate for the large quenching effects. For the calibration several standard solutions were prepared, using 7 ml 1M HCl and 10 ml of Insta Gel Plus under the same conditions as for the Tl measurements. A known activity of a ^{3}H standard solution was added and varying amounts of CCl_4 to obtain different quenching factors. Using the theoretical calculations for ^{3}H and ^{204}Tl it was thus possible to establish a calibration curve for ^{204}Tl.

3.7 Radiochemical Separation and Sample Preparation

3.7.1 Pb/Tl separation

The separation was done using a MnO_2 co-precipitation method described by Luke [79–81]. The separation yield was determined photometrically by the rhodamine B method.

Reagents A standard thallium solution was prepared by dissolving 0.2606 g $Tl(I)NO_3$ in 1 l water. 50 ml of this solution was diluted to 1 l, giving the final concentration of 10 μg Tl per ml. A manganese chloride solution was made by diluting 2 ml of a 50% $MnCl_2$ solution to 100 ml. A 1% $KMnO_4$ solution was also prepared. The butyl cellosolve

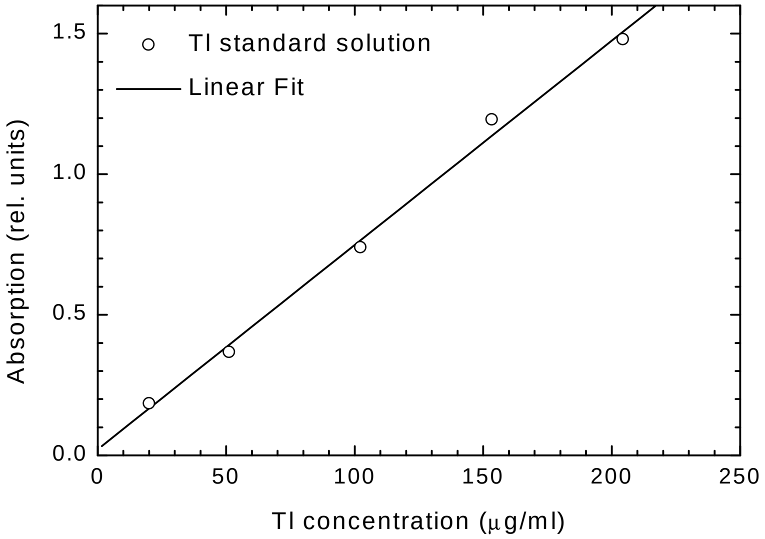

Figure 3.14: UV-VIS Calibration curve for the determination of the chemical yield of the Pb/Tl separation

solution was made my mixing 100 ml of ethylene glycol monobutyl ether with 200 ml of water. The rhodamine B solution was of 0.1% concentration.

Calibration Curve for Thallium 2 to 20 ml of the Tl standard solution was transfered to a 125 ml conical flask. 2 ml sulfuric acid and about 100 mg hydrazine sulfate were added and evaporated to about 1 ml volume. After cooling down to room temperature 10 ml of diluted hydrochloric acid were added together with 1 ml of water saturated with bromine, to oxidize Tl(I) to Tl(III). The mixture was heated uncovered for a few minutes until all bromine had been expelled. Finally the solution was cooled down to 25° C and poured into a 125 ml separatory funnel. The inside of the flask was washed with further 10 ml of diluted hydrochloric acid. 2 ml of the rhodamine B solution, 1 ml of butyl cellosolve solution and 15 ml of benzene were added. After extraction and centrifugation to free the decanted benzene from water droplets, the extract was immeadiatly measured photometrically with the UV-VISIBLE Recording Spectrometer UV-160A from Shimadzu. The calibration curve and some absorption spectra are shown in Figures 3.14 and 3.15.

Separation and thin sample preparation The Pb samples, each about 10 g, were dissolved separately in about 50 ml diluted nitric acid. The mixture was heated gently until all Pb was dissolved and finally boiled vigorously to expel brown fumes. 500 ml water, 1 mg Tl tracer and 5 ml of the 1% $KMnO_4$ solution were added and heated to gentle boiling using a magnetic stirrer. Two successive 1-ml portions of $MnNO_3$ were added and the mixture boiled for 2 minutes after each addition. The solution was cooled down and the precipitate zentrifuged off. The MnO_2 was washed with water to remove remaining lead salts. The Tl containing precipitate was dissolved in hydrochloric acid and heated until all chlorine is expelled. The solution was pipetted dropwise on a filterpaper and after drying ready for the beta counting.

After the counting the precipitate was dissolved again in hydrochloric acid, and diluted to 100 ml in a volumetric flask. 5 ml of this solution were then used to check the yield

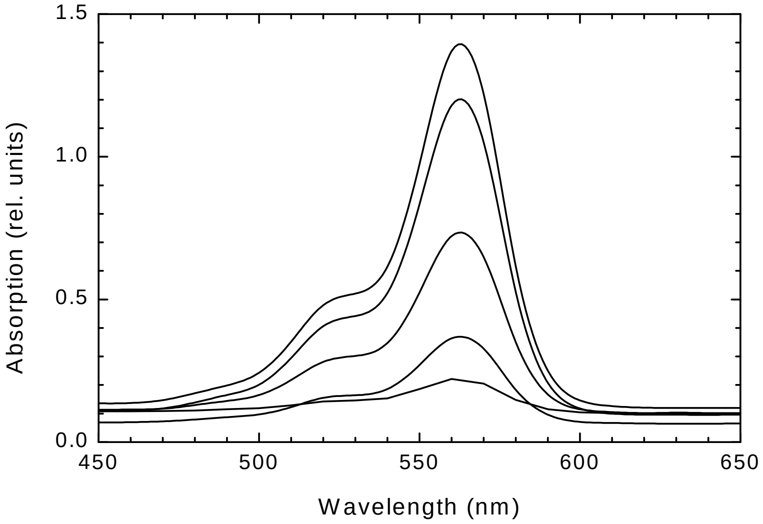

Figure 3.15: UV-VIS absorption spectra for Tl concentrations between 20 and 200 μg/ml

of the chemical separation. The procedure was the same as described for the calibration curve.

The remaining 95 ml were evaporated to about 3 ml for further Liquid Scintilation Counting (LSC). The measured activity had to be corrected accordingly.

3.7.2 Mo/Nb separation

Only the front disk of the large Mo sample was foreseen for chemical separation of Nb from the bulk of Mo and the matrix activities, since it contained the highest amount of ^{88}Y, produced via the ^{92}Nb(n,αp)^{88}Y reaction and the ^{92}Nb(n,αn)^{88}Zr reaction with its subsequent decay to ^{88}Y, which was the main source of the high Compton background. A Fe(OH)$_3$ coprecipitation method was used for the separation, and γ-ray-spectroscopy for checking the chemical yield of the separation.

Development of the Method A non activated metallic Mo sample of 12 g was dissolved in 200 ml hot aqua regia, adding 10 ml of Fe solution. This solution was prepared by dissolving 1209.2 mg FeCl$_3$·6H$_2$O in 250 ml water. 1 ml of the solution thus contained 1 mg Fe. In order to check the chemical yield, a known activity of $^{92\mathrm{m}}$Nb was added. The solution was heated until all brown fumes were expelled and then it was diluted to 400 ml. NH$_3$ was then added while heating the solution. On neutralisation and the precipitate Fe(OH)$_3$ was formed which carried the Nb activities. The precipitate was centrifuged off and dissolved in hydrochloric acid. The iron was extracted from the solution with several 50 ml portions of diethylether saturated with HCl. The aquous phase contained the desired Nb activities and still some disturbing ^{88}Y. A further puryfication step was done by extracting the Nb with diisopropylketone (DIPK). The organic phase was washed twice with 10 M HCl and the Nb finally backextracted with 6 M HNO$_3$/1 M H$_2$O$_2$. The solution was then evaporated to dryness and measured γ-ray-spectrometrically. The overall yield of the separation was 80%.

Processing of the front disk The front disk consists of seven individual disks of about 42 g each. Each disk was measured via γ-ray-spectroscopy in order to identify longer lived radioactive Nb isotopes (^{91}Nb(62 d) and ^{95}Nb(35 d)), which were used to calculate the chemical yield of the separation. No additional $^{92\mathrm{m}}$Nb tracer was needed. Each disk was dissolved in hot aqua regia and the resulting solution was heated until all brown fumes have been expelled. After the sample was completly dissolved the solution was divided in three parts. The coprecipitation procedure was done for each of the 21 individual portions. The dissolved Fe(OH)$_3$ precipitates were merged and further processed as described above. The final extract was evaporated to dryness and measured via γ-ray-spectroscopy in the underground laboratory hades.

The chemical separation was very clean but the overall chemical yield of the multistep process was too low. The result was therefore not taken into account and the activity determined from a counting done before the chemical processing was used to calculate the cross section.

3.8 Data Analysis

3.8.1 Calculation of Experimental Cross Sections

Since no attempt was made to determine the absolute neutron flux, all cross sections σ_x were measured relative to the standard cross section of the ^{27}Al(n,α)^{24}Na reaction. For each given neutron energy the cross section value σ_s was obtained by linear interpolation of the tabulated data given in [62]. Thus, when sufficient ^{24}Na activity was induced in the Al monitor foils, the cross section was calculated with the basic formula:

$$\sigma_x = \sigma_s \left(\frac{F_x}{F_s} \right) \tag{3-24}$$

where F_s and F_x denote the measured molar reaction rates of the standard reaction and the reaction under investigation. The measured molar reaction rate F_i for each sample and monitor foil at a certain distance from the target is given by

$$F_i = \frac{\lambda_i \; Y_i \; A_i}{b_i \; \epsilon_i \; m_i \; a_i} \cdot \frac{1}{1 - e^{-\lambda_i t_e}} \cdot \frac{1}{e^{-\lambda_i t_c}} \cdot \frac{1}{1 - e^{-\lambda_i t_m}} \cdot \prod_k c_{ik}, \tag{3-25}$$

where

λ_i = decay constant
Y_i = number of measured γ-ray counts
A_i = molar mass
b_i = γ-ray branching factor
ϵ_i = full-energy-peak detection efficiency of the Ge detector
a_i = isotopic abundance of the target nuclide
t_e = irradiation (exposure) time
t_c = cooling time
t_m = sample measurement (counting) time
c_{ik} = correction factors.

The values for λ_i and b_i were taken from PcNuDat [67], for A_i from Audi and Wapstra [12], and for a_i from Rosman and Taylor [51]. In case of the enriched Mo and Pb samples the values given by the supplier were adopted and for natural lead from an isotopic measurement (cf. Tables 3.2 and 3.1). The calculation or measurement of the correction factors c_{back}, $c_{breakup}$, c_{flux}, c_{coin}, c_{scatt}, c_{disk}, c_{low}, and c_{abs} is described in the previous sections. In case of the solid Ti/T target the breakup correction is not needed and thus $c_{breakup}$ sets to unity.

At least two monitor foils were always attached to the sample, one in the back and the other in front. In cases, where several samples were irradiated as stack, additional monitor foils were inserted to monitor the flux gradient within this stack. The molar reaction rates F_{foil}, measured for each individual monitor foil at a certain distance d_{foil} from the neutron source had to be corrected for the flux gradient within the sample stack and were normalized for a reference distance, i. e. the center of the stack:

$$F_{center} = \frac{d_{foil}^2}{d_{center}^2} \cdot F_{foil}. \tag{3-26}$$

The distances were measured from the inside of the Ag backing of the Ti/T target to the middle of the foil under consideration. An average was taken of the thus corrected molar reaction rates and used in Eq. 3-24.

When a measurement was made with the Bonner sphere or the long counter as standard alone, a further calibration step was needed. The reaction rate of the monitor was replaced by following expression:

$$F_s = F_{cal} \cdot \frac{d_{cal}^2}{d_s^2} \cdot \frac{N_s^{BS}}{N_{cal}^{BS}}. \tag{3-27}$$

Here N^{BS} denotes either the count rate in the Bonner sphere or the long counter of the calibration run or the actual measurement. F_{cal} is the reaction rate in the monitor foil of the calibration, again corrected for possible variations of the distance.

In cases were two reactions on different isotopes led to the same activity in the sample, the above approach was not valid. An example is the ^{96}Nb production in a Mo sample via the ^{96}Mo(n,p) and ^{97}Mo(n,np) reactions. The cross section can be determined by irradiating two samples with different isotopic compositions, e.g. natural Mo and enriched ^{97}Mo, and measuring the cross section $\sigma_{n,x}$ for the production of ^{96}Mo characteristic for the specific sample. The cross section for the natural sample is given by the following equation:

$$\sigma^n_{n,x} = a^n_{96}\sigma_{n,p} + a^n_{97}\sigma_{n,np}, \tag{3-28}$$

and for the enriched sample by

$$\sigma^e_{n,x} = a^e_{96}\sigma_{n,p} + a^e_{97}\sigma_{n,np}, \tag{3-29}$$

where a denotes the isotopic abundance in the natural (n) and the enriched (e) sample. Solving these two equations leads to expressions for the desired cross sections:

$$\sigma_{n,p} = \frac{a^n_{97}\sigma^e_{n,x} - a^e_{97}\sigma^n_{n,x}}{a^e_{96}a^n_{97} - a^n_{96}a^e_{97}}, \tag{3-30}$$

$$\sigma_{n,np} = \frac{a^e_{96}\sigma^n_{n,x} - a^n_{96}\sigma^e_{n,x}}{a^e_{96}a^n_{97} - a^n_{96}a^e_{97}}. \tag{3-31}$$

3.8.2 Uncertainties

Table 3.10 summarizes the sources of uncertainties and their estimated magnitudes. The large error for the background neutrons are mainly caused by the uncertainties of the involved excitation functions. The uncertainty of the reference monitor cross section was usually less than 5%, the value of 10% given here was for a measurement near the threshold of both the investigated ^{99}Tc(n,n'γ)^{99m}Tc and the ^{115}In(n,n'γ)^{115m}In reference cross sections. The total uncertainty for each cross section was obtained by combining the individual uncertainties in quadrature according to the law of error propagation.

Table 3.10: Sources of uncertainties and their magnitudes

Source of uncertainty	Magnitude (%)
Count rate (statistics and background)	1−25
Detector efficiency	2−3
γ-ray-emission probability	0.01−8
Half-life	0.01−8
Coincidence summing	0−7
γ-ray absorption	0.1−3
Sample mass	<1
Counting time	<1
Cooling time	<1
Background neutrons	
a) gas-in / gas-out	0.2−6
b) breakup	0−16
c) low energy	0−12
Neutron flux fluctuation	0.1−0.5
Reference monitor cross section	0.5−10
Total uncertainty	6−26

Chapter 4

Nuclear Model calculations

Neutron, charged particle and γ-ray emission cross sections, both as a function of energy and angle, play an important role in fusion and fast reactor development, especially in calculations on decay heat, gas production, activation and radiation transport. Nuclear model calculations are an important tool for evaluators to reliably interpolate the existing data or even extrapolate the data to energy ranges and angles, where no data exist or in cases where a measurement is simply not feasible. Due to this importance, extensive efforts have been devoted to development and improvement of codes. Some of the recent improvements include:

- ⇨ a unified description of the equilibrium and pre-equilibrium (PE) processes,
- ⇨ use of consistent input parameters, which are ideally based on experimental data,
- ⇨ choice of proper level density description,
- ⇨ consideration of systematics of particle induced reactions for an isotopic chain or neigbouring elements.

Some models of the HAUSER-FESHBACH type are HELGA [82], GNASH [83], EMPIRE [84], STAPRE [85] and STAPRE-H [86, 87]. In the present work the original STAPRE code was used for calculations of neutron induced reactions on the radioactive target nucleus ^{99}Tc as well as on lead. For the isotopes of molybdenum and vanadium, on the other hand, a modified version of the original STAPRE code was used: STAPRE-H. The calculations were performed in collaboration with the *National Institute for Physics and Nuclear Engineering* in Bucharest [1] and the *University of Debrecen* [2].

4.1 The codes STAPRE and STAPRE-H

The original STAPRE code by UHL and STROHMAIER [85] was designed to calculate the energy-averaged cross ections for particle induced reactions, assuming a sequential evaporation of the emitted particles and γ-rays. The code STAPRE-H by AVRIGEANU *et*

---

[1] "Horia Hulubei" National Institute for Physics and Nuclear Engineering, P.O. Box MG-6, 76900 Bucharest, Romania

[2] Institute of Experimental Physics, Debrecen University, H-4001 Debrecen, Hungary

al. [86] is an extension of the original code. Both codes are written in FORTRAN and are available from the NEA Data Bank[3].
The original STAPRE code takes into account:

- ⇨ equilibration of the compound system formed in the first stage of the reaction by means of the particle precompound emission exciton model (EM),
- ⇨ statistical de-excitation in the frame of the Hauser-Feshbach-Moldauer (HFM) model with consideration of angular momentum and parity conservation,
- ⇨ intermediary γ-ray cascades,
- ⇨ fission mechanism.

The extensions in STAPRE-H are mainly:

- ⇨ calculation of particle transmission coefficients by means of the spherical optical model code SCAT 2 [88] as a subroutine,
- ⇨ inclusion of the pre-equilibrium emission geometry-dependent hybrid (GDH) model code HYBRID as a subroutine with a version including the angular momentum, parity conservation and α-particle emission
- ⇨ computation of the nuclear level densities taking into account the formulas of Ignatyuk and Schmidt and back-shifted Fermi-gas (BSFG) model,
- ⇨ inclusion of the energy-dependent Breit-Wigner model (EDBW).

The code is then able to calculate the activation cross section, the population of isomeric states, the production cross section for γ-rays from low level excited levels, the energy spectra for all emitted particles and the γ-ray production spectra.

4.2 Input Parameter

The necessary input parameters are passed to the STAPRE code via an input file that contains ...

...the Optical Model Potential (OMP) parameters that are required to calculate the transmission coefficients and inverse reaction cross sections. The OMP parameters are checked for their predictive power by calculating total and nonelastic cross sections and comparing the results to experimental values, when available.

...Preequilibrium Emission (PE) parameters

...Reduction factor, in order to account for the fraction of the total cross section, that is not related to Compund Nucleus and PE mechanisms, which are mainly direct reactions.

---

[3] Nuclear Energy Agency, Issy-les Moulineaux, France `http://www.nea.fr/html/dbprog`

...Separation energies, calculated from the masses given by the atomic mass evaluation of Audi and Wapstra [12].

...Discrete levels and level density parameters, including information about energy, spin, parity and γ-ray branching, available from various sources [67, 74]

4.3 Formalism

The incident particle and the target nucleus are assumed to form a composite system, called the first compound nucleus 1^{st} CN, even if not yet in equilibrium. The particle emission in a specific order is regarded as leading to the next compound nucleus, which goes through de-excitation processes via emission of particles, i. e. neutrons, protons, α-particles, deuterons, γ-rays or via fission. PE particle emission is taken into account in the first step of the evaporation cascade either uing the Excition Model (EM), geometry dependent-hybrid model (GDH) or the modified GDH model including angular momentum and parity conservation. The Hauser-Feshbach-Moldauer (HFM) formula is applied for the fraction of the population of the composite system that did not undergo PE decay. All further evaporations are treated within the conventional evaporation model, giving the primary populations combined with a γ-ray cascade model.

4.4 Scope of the Present Calculation

Nuclear model calculatios were performed for all experimental investigated reactions on V, Mo, Tc and Pb. Neutron, proton, α-particle and γ-ray emissions are considered from threshold to 20 MeV. Not taken into account are cluster emissions like deuteron,triton and ^{3}He emission, which are known to have small cross section. In order to allow a direct comparsion with experimental results obtained with the activation technique, the cross sections for (n,np) and (n,pn) and (n,d) reactions are summed together.

Chapter 5

Results and Discussion

5.1 Vanadium

Three neutron induced reactions on vanadium, namely $^{\mathrm{nat}}$V(n,xα)^{47}Sc, ^{51}V(n,α)^{48}Sc and ^{51}V(n,p)^{51}Ti have been investigated in the energy range 11.7–20.5 MeV. The numerical data are summarised in Table 5.1. A detailed discussion of the three reactions in comparison to evaluations and STAPRE-H95 model calculations is given in the following sections.

Table 5.1: Measured cross sections on natural vandium

Neutron energy (MeV)	Cross section (mb) $^{\mathrm{nat}}$V(n,xα)^{47}Sc	^{51}V(n,α)^{48}Sc	^{51}V(n,p)^{51}Ti
11.7±0.2	0.055±0.005	8.3±0.8	
13.4±0.1	0.094±0.010	14.1±1.2	
13.9±0.2	0.086±0.005	15.4±1.1	
14.3±0.2	0.089±0.006	14.2±1.2	
15.0±0.2	0.14±0.01	18.2±1.7	26±2
16.1±0.2			25±2
16.2±0.2	0.40±0.02	19.8±1.8	
18.0±0.1	4.0±0.2	21.1±1.8	
19.3±0.1	10.8±0.6	19.8±1.8	
20.5±0.1	17.3±1.3	14.6±1.6	

5.1.1 $^{\mathrm{nat}}$V(n,xα)^{47}Sc reaction

As outlined in Chapter 2, the main motivation for the vanadium irradiation was the measurement of the $^{\mathrm{nat}}$V(n,xα)^{47}Sc cross section, which consists of contributions from the ^{51}V(n,n'α)^{47}Sc and ^{50}V(n,α)^{47}Sc processes. An excitation curve is established for the first time and it is in agreement with the good quality data recently measured around 14 MeV [33,35,89,90], as can be seen in Figure 5.1. It also shows the appropriate threshold behavior of the dominant reaction channel. This work is at variance with the earlier data of Ref. [32]. Over the whole energy range studied here, the cross section for the production

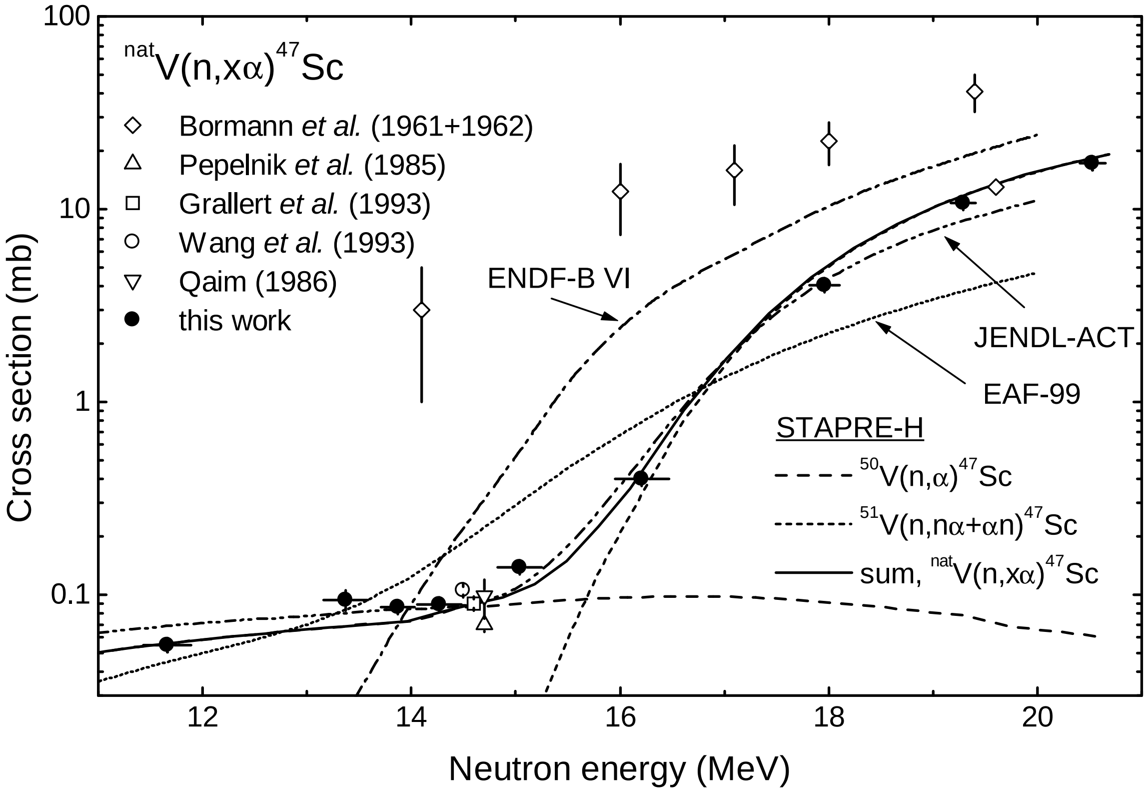

Figure 5.1: Comparison of the measured cross sections for the ^{nat}V(n,xα)^{47}Sc reaction with existing experimental data [31–33,35,89,90], evaluations and STAPRE-H calculations

of ^{47}Sc from ^{nat}V is much lower than that suggested by this earlier measurement above 15 MeV [31,32].

Clearly the trend of this new measurement for the ^{nat}V(n,xα)^{47}Sc cross section is rather well described by the model calculation. The calculation shows that the contribution of the ^{51}V(n,n'α)^{47}Sc reaction to the formation of ^{47}Sc dominates above incident energies of 15 MeV, where it is an order of magnitude higher than the cross section of the ^{50}V(n,α)^{47}Sc reaction multiplied by the natural abundance of ^{50}V. Therefore, both the previous data around 14.8 MeV [33, 35, 89] and the measurements carried out in this work at energies below 15 MeV, correspond to the latter reaction. This conclusion is supported by the ^{50}V(n,α)^{47}Sc cross section value deduced from the systematics at 14.8 MeV [91]. The model estimate for the ^{50}V(n,α)^{47}Sc reaction is somewhat lower than the data between 13 and 15 MeV.

5.1.2 ^{51}V(n,α)^{48}Sc reaction

From the irradiation performed for the determination of the ^{nat}V(n,xα)^{47}Sc reaction also the cross sections for the ^{51}V(n,α)^{48}Sc reaction were obtained. They are shown in Figure 5.2 together with the existing data and model calculations. Above 18 MeV this measurement provides the second dataset of this cross section. In that energy range our measurements suggest values slightly higher than those reported in Ref. [92]. This is probably due to improvements in the standard (reference) cross sections. In general, the

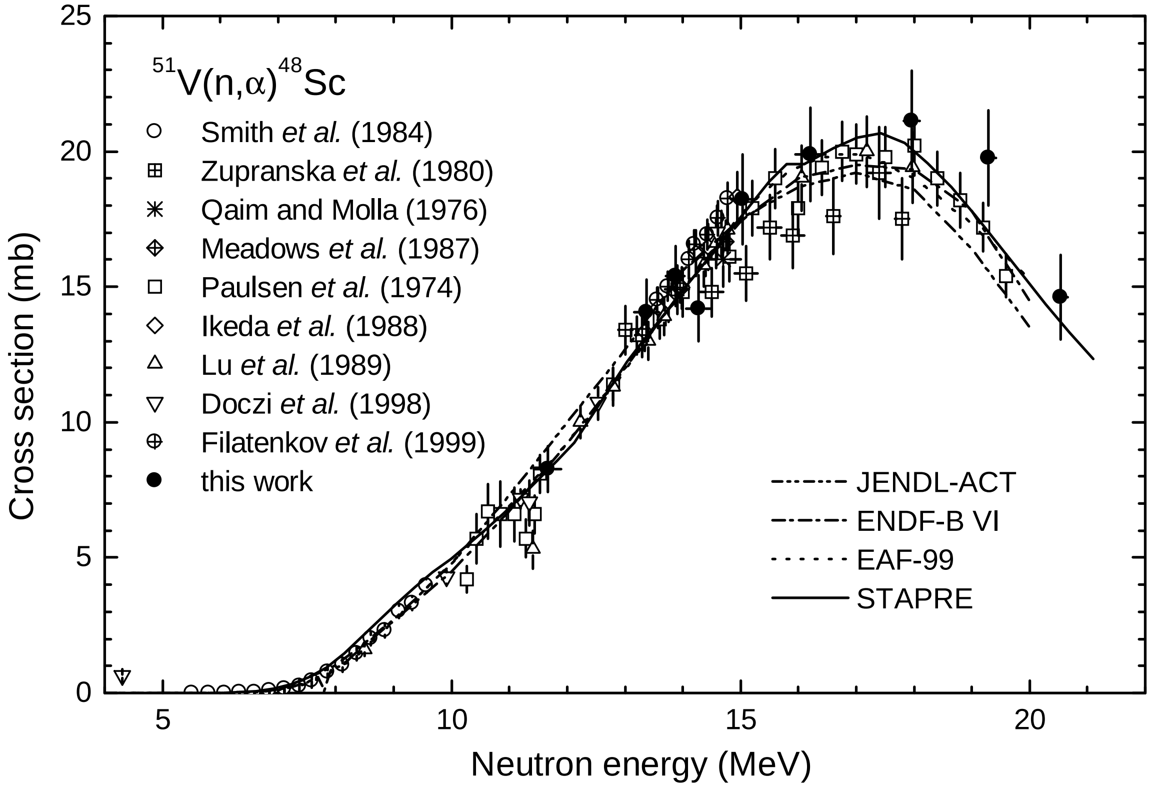

Figure 5.2: Comparison of the measured cross sections for the ^{51}V(n,α)^{48}Sc reaction with existing experimental data [92–99], evaluations and STAPRE-H calculations

agreement of the new measurement for the ^{51}V(n,α)^{48}Sc reaction with the existing data is good within the given uncertainties. Also the overall agreement between the model calculation and the experimental data is seen to be good.

5.1.3 ^{51}V(n,p)^{51}Ti reaction

Only two data points were added to the recent measurements by Fessler et al. [57] for the ^{51}V(n,p)^{51}Ti reaction. The energies were chosen to establish wether those recent measurements should be extrapolated to the higher or the lower set of cross sections determined previously at 14 MeV. The new data agree within the uncertainties both with the results of Fessler *et al.* [57] and with the measurements reported in Refs. [93–95, 100] A discrepancy is, however, observed with the higher cross section data of Ref. [101].

Fig. 5.3 shows that the excitation function of the ^{51}V(n,p)^{51}Ti reaction is described rather well by the model calculation. Slight discrepancies exist. Between 4.5 and 7 MeV the model estimate is below the measured data. Most likely this is due to some of the spin and parity assignments of the 22 discrete levels used for ^{51}Ti. Between 9 and 10 MeV the model has to make the best of the slight mismatch in the measured data of Refs. [93] and [100] and at 20.5 MeV the model estimate is slightly higher than the data of Ref. [57]. The energy dependence of the pre-equilibrium contribution is influenced by the successive openings of partial wave contributions, visible around 16 MeV, resulting in a sudden rise of the preequilibrium contribution. The calculated cross section had to be smoothed to

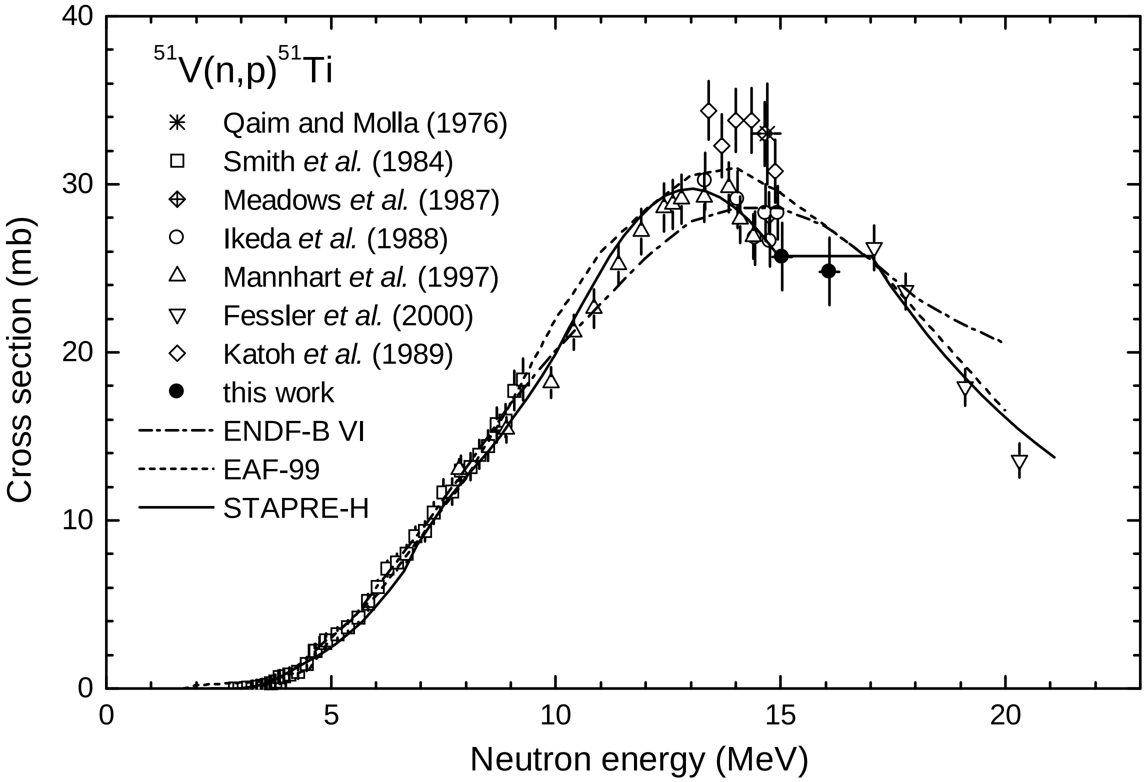

Figure 5.3: Comparison of the measured cross sections for the ^{51}V(n,p)^{51}Ti reaction with existing experimental data [57, 93–96, 100, 101], evaluations and STAPRE-H calculations

render the calculation physical.

5.2 Molybdenum

The main motivation for measurements on molybdenum was to determine the production cross section of ^{94}Nb from natural Mo. It is produced via the ^{94}Mo(n,p) and ^{95}Mo(n,np) reactions, which cannot be distinguished by irradiating Mo of natural isotopic composition. Since a complete set of enriched Mo isotpoes (except ^{95}Mo) was at our disposal, the formation of several Nb isotopes via competing (n,p) and (n,np) ractions on neighbouring isotopes was also studied and the results are described in Section 5.2.1. In addition some (n,2n) and (n,α) reaction were studied, which are presented in Section 5.2.2. The decay data of all studied reaction products are already given in Table 3.6, page 31. All measured cross sections are compared with nuclear model calculations done using the code STAPRE-H95. Whereever possible, a comparison with the EAF-99 and JENDL-3.2 evaluated data files is also given.

5.2.1 Some (n,p) and (n,np) cross sections

5.2.1.1 ^{nat}Mo(n,x)^{94}Nb reaction

The ^{nat}Mo(n,x)^{94}Nb reaction has previously been measured by GREENWOOD *et al.* [40] and IKEDA and KONNO [41] in the 14 MeV region using the activation technique. In both cases natural and enriched samples were irradiated using a high intensity neutron source. Extending the excitation function to higher energies was only possible with neutron sources of much lower intensity, like the ^{3}H(d,n)^{4}He reaction at the 7 MV Van de Graaff accelerator in Geel.

Our measured data are given in numerical form in Table 5.2 and are plotted together with the experimental literature values, evaluations and model calculations in Figure 5.4. Good agreement was found with the existing data from GREENWOOD *et al.* [40] and IKEDA and KONNO [41]. Even though the uncertainties of our results are somewhat larger due to a non-ideal irradiation geometry and low neutron flux, at least the two data points at 14.5 and 18.0 MeV met the demanded accuracy of 20% asked for in the *High Priority Request List*, request ID 3.C.10. [8]. The uncertainty of the highest energy point is larger, since it was derived from an early measurement, done at a time when the matrix activity and thus the Compton background was still very high. A subsequent attempt to separate the tracer amounts of Nb from the bulk of Mo showed a too low chemical yield, which gave reason to discard the result (cf. Section 3.7.2, page 43).

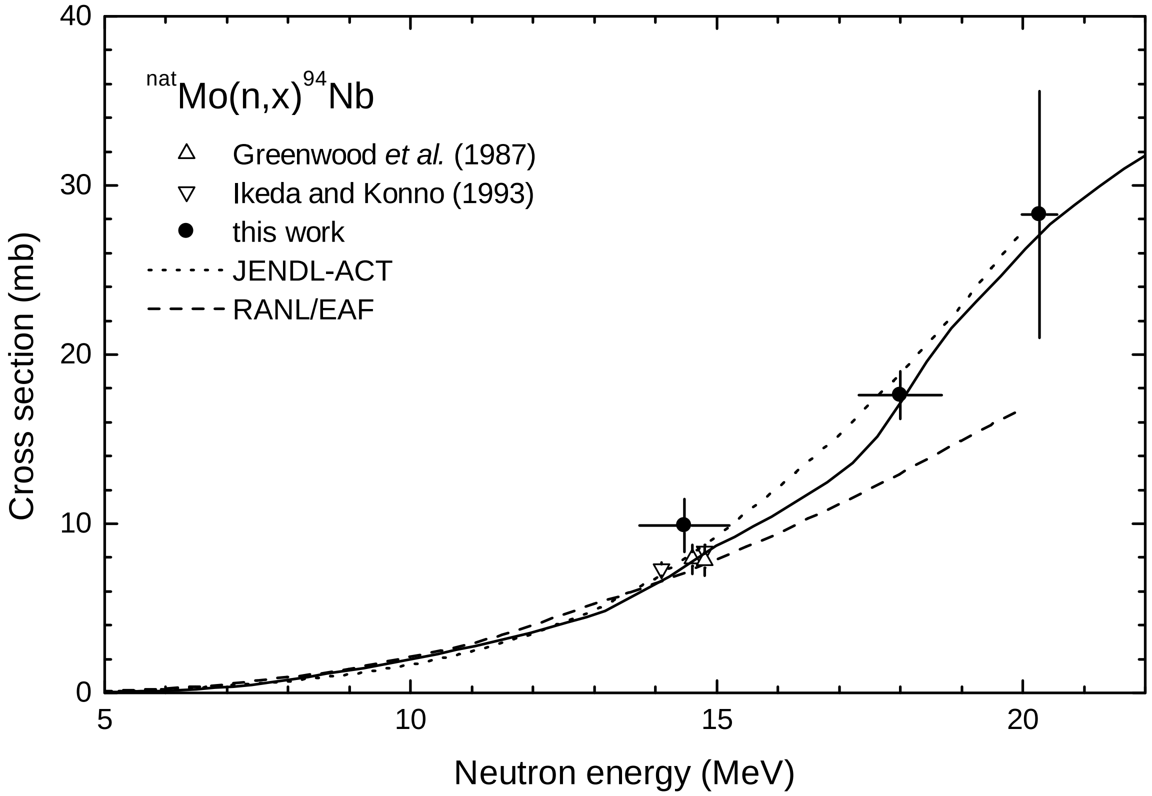

Figure 5.4: Comparison of the measured cross section for the ^{nat}Mo(n,x)^{94}Nb reaction with existing experimental data in the 14 MeV region [40, 41], evaluations and STAPRE-H calculations.

Table 5.2: Measured cross sections for the ^{nat}Mo(n,x)^{94}Nb reaction

Neutron energy (MeV)	Cross section (mb)
14.5±0.7	9.9±1.6
18.0±0.7	17.6±1.4
20.3±0.3	28.3±7.3

5.2.1.2 ^{92}Mo(n,p)^{92m}Nb and ^{98}Mo(n,p)^{98m}Nb reactions

The ^{92}Mo(n,p)^{92m}Nb and ^{98}Mo(n,p)^{98m}Nb reactions denote the only two cases in the chain of Mo isotopes for which no competing (n,np) reaction exists, that would lead to the same nuclide. The cross section could thus be measured from sample material with natural isotopic composition. The measured cross sections are given in Table 5.3.

Table 5.3: Measured cross sections for the ^{92}Mo(n,p)^{92m}Nb and ^{98}Mo(n,p)^{98m}Nb reactions

Neutron energy (MeV)	^{92}Mo(n,p)^{92m}Nb Cross section (mb)
16.22±0.26	43.1±2.9
18.00±0.13	24.3±3.1
19.27±0.12	40.9±5.5
20.51±0.13	39.7±6.7

Neutron energy (MeV)	^{98}Mo(n,p)^{98m}Nb Cross section (mb)
16.22±0.26	6.9±0.6
18.01±0.13	7.5±1.2
19.25±0.13	9.5±1.1
20.51±0.12	7.2±0.8

For the ^{92}Mo(n,p)^{92m}Nb reaction this measurement is only the second for energies higher than 16 MeV, shown in Figure 5.5. The only other dataset is from Liskien *et al.* [42], measured under a Geel-Jülich collaboration. The present data are somewhat lower compared to the older data, which were determined using an incident deuteron beam of 3 MeV and multiple samples arranged in a circular geometry. In our measurement the corrections for low energy neutrons were done thoroughly. They were up to 50%. Our data are confirmed by the STAPRE calculation, which describes the experimental results rather good. For the two lower energy points the calculated cross sections agree with the experiment within the error bars, while for the two higher energy values the model predicts lower cross sections.

Figure 5.6 shows the results for the ^{98}Mo(n,p)^{98m}Nb reaction, which are the first measurements in the energy range from 16 to 20.5 MeV. It is in good agreement with the existing data at 14 MeV and the only higher energy point from MARCINKOWSKI *et al.* [121]. The EAF-99 evaluation is slightly higher than our results. However, the STAPRE calculation describes the data very well over the whole energy range and is in good agreement with the experimental results.

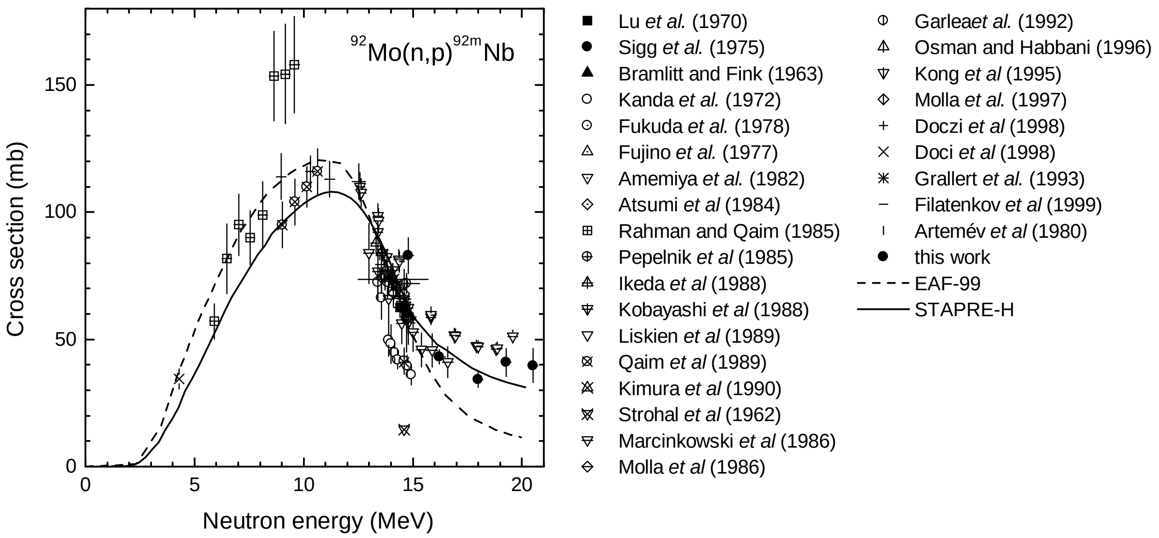

Figure 5.5: Comparison of the measured cross sections for the ^{92}Mo(n,p)^{92m}Nb reaction with existing experimental data [42, 89, 95, 98, 99, 102–122], evaluations and STAPRE-H calculation.

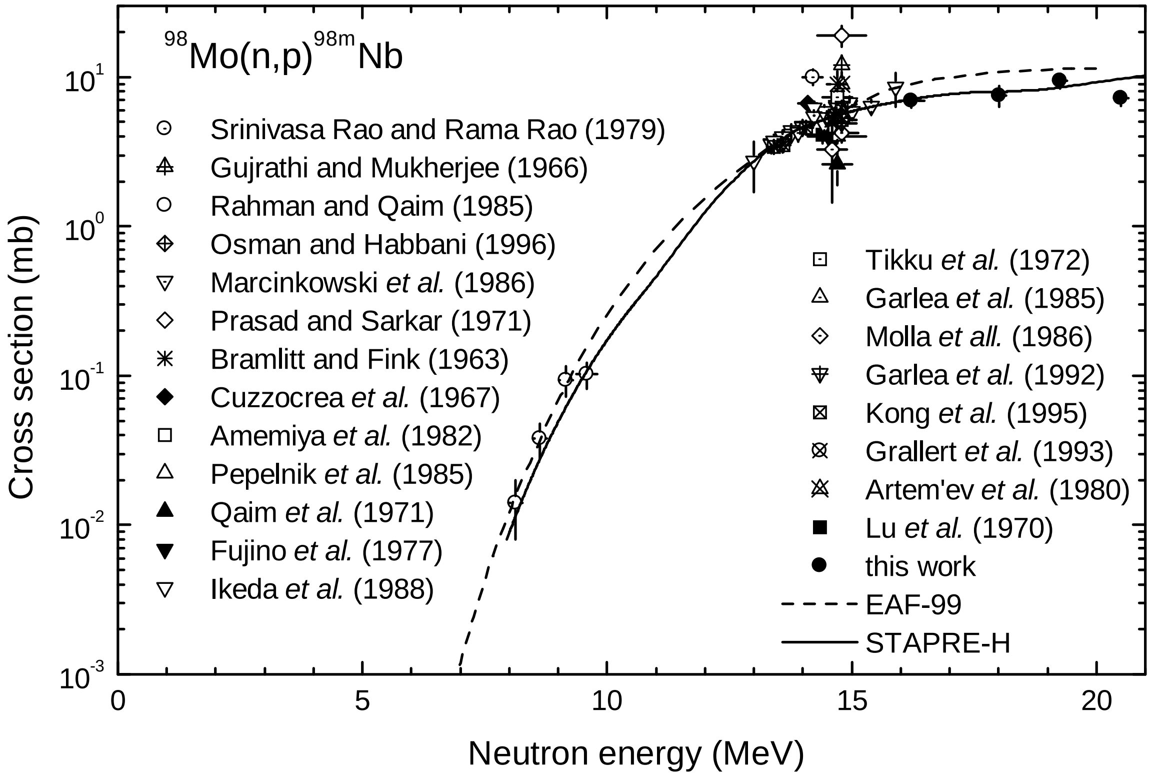

Figure 5.6: Comparison of the measured reaction cross sections for the ^{98}Mo(n,p)^{98m}Nb reaction with existing experimental data [89,95,102,103,107,112,113,115,115,116,121–127], evaluations and STAPRE-H calculation.

5.2.1.3 (n,p) and (n,np) reactions leading to ^{95m}Nb and ^{96}Nb

^{95}Mo(n,p)^{95m}Nb: ^{95m}Nb is produced via both the ^{95}Mo(n,p) and the ^{96}Mo(n,np) reactions. Enriched samples were thus used to measure the cross sections, which are given in Table 5.4. The data for the ^{95}Mo(n,p)^{95m}Nb reaction are plotted in the upper part of Figure 5.7 together with the existing data in the 14 MeV region. This measurement provides the first data above 16 MeV. The highest neutron energy measured so far was around 16 MeV by MARCINKOWSKI *et al.*. [121], which agrees with the present results within the given uncertainties. A comparison with the EAF-99 evaluation shows an overestimation of about 25–30% over the whole investigated energy range. A slightly better agreement can be observed with the STAPRE-H model calculation, which shows an overall flatter behaviour than the EAF-99 excitation function. Above 17 MeV the calculated curve is almost constant, which is confirmed by the measurement. However, the model overpredicts the cross section by 15 to 25%.

Table 5.4: (n,p) and (n,np) cross section for the formation of ^{95m}Nb

Neutron energy (MeV)	^{95}Mo(n,p)^{95m}Nb Cross section (mb)	Neutron energy (MeV)	^{96}Mo(n,np)^{95m}Nb Cross section (mb)
16.55±0.26	5.4±0.7	16.22±0.05	3.3±0.4
18.00±0.13	4.8±0.9		
19.27±0.13	5.0±1.3	19.31±0.11	12.0±1.0
20.51±0.13	5.1±0.9	20.6±0.08	14.2±2.1

^{96}Mo(n,np)^{95m}Nb: The other way of producing ^{95m}Nb is via the ^{96}Mo(n,np)^{95m}Nb reaction, shown in the lower part of Figure 5.7. Only two datasets exist so far for this reaction, namly from ATSUMI *et al.* [114] and IKEDA *et al.* [95], both in the 14 MeV region. The EAF-99 evaluation is too high over the whole energy range. For neutron energies up to 16 MeV the deviation is about 50%. For the two highest energy points of this work the deviation is only 10–20%. The STAPRE calculation, on the other hand, describes very well the existing data in the 14 MeV region, but for higher energies it predicts a too high cross section, which is about the same order of magnitude as the EAF-evaluation.

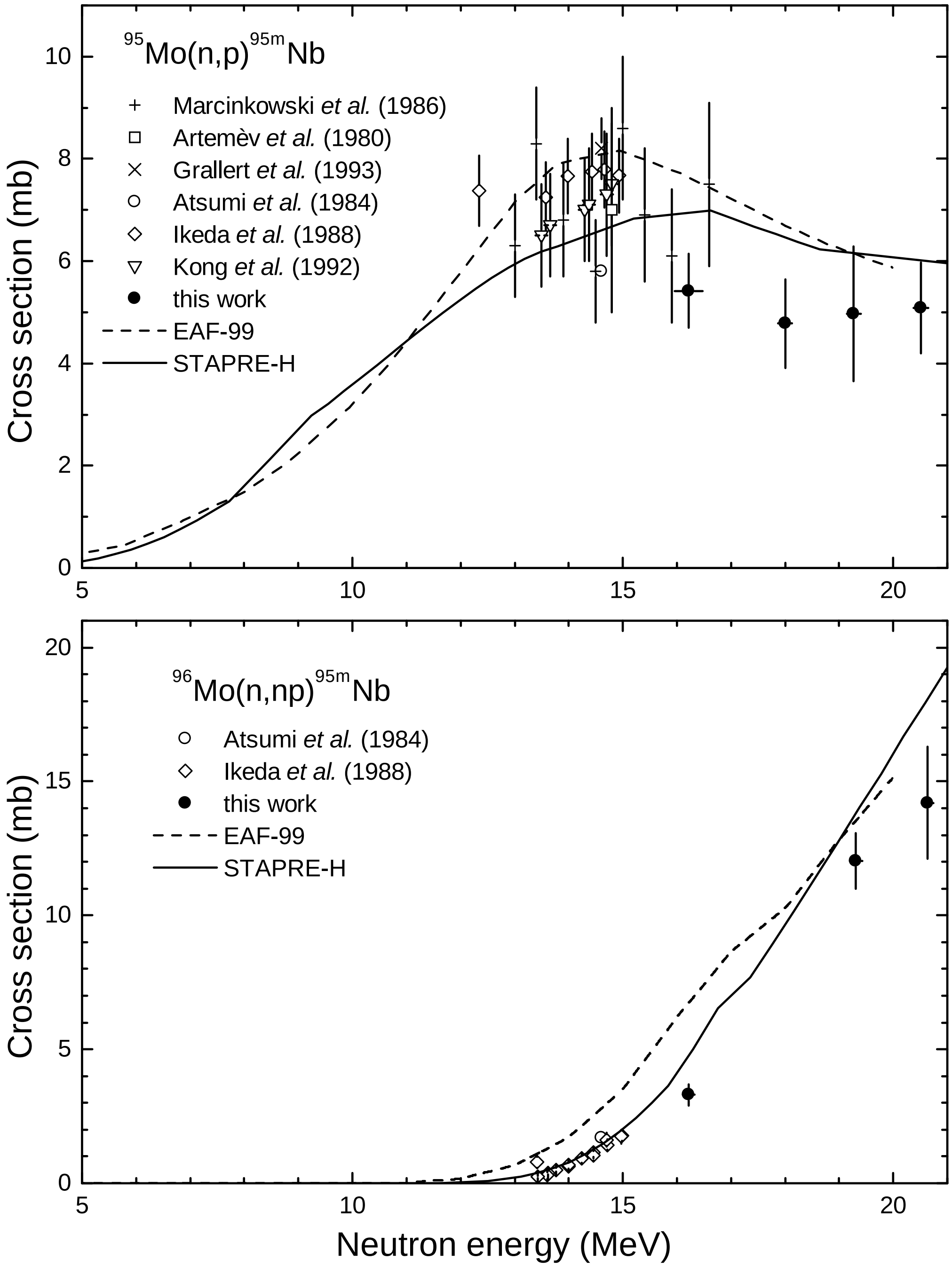

Figure 5.7: Comparison of the measured cross sections for the ^{95}Mo(n,p)^{95m}Nb and ^{96}Mo(n,np)^{95m}Nb reactions with existing experimental data [89, 95, 106, 114, 121, 128], evaluations and STAPRE-H calculations.

^{96}Mo(n,p)^{96}Nb This mesurement provides only the second data set for the ^{96}Mo(n,p)^{96}Nb reaction over the energy range of 16 to 20 MeV. The only other measurement to date was by Liskien *et al.* [42]. Table 5.5 shows the numerical values found in this work and Figure 5.8 presents the data in graphical form. Also shown are the extensive data base existing around 14 MeV and a single measurement done near the threshold of the reaction by Rahman and Qaim [115]. It should be noted that the measurement of Liskien *et al.* [42] was done with molybdenum of natural isotopic composition and thus the value is a composite of the (n,p) reaction on ^{96}Mo and the (n,np) reaction on ^{97}Mo, discussed in the next paragraph. Due the contribution from the latter reaction the cross section reported by Liskien *et al.* besides an older measurement, also done at this laboratory, is too high. The excitation function is well described by the EAF-99 evaluation from threshold up to about 18 MeV. For higher energies the cross sections given by this evaluation are somewhat higher than the measurements presented here; it was apparently oriented to the older measurements in this energy interval. The JENDL-3.2 file on the other hand is slightly higher than the experimental data close to threshold, but gives a better description of the data for energies above 18 MeV. The best description is obtaind with the STAPRE-H calculation, which gives good agreement over the whole energy range.

Table 5.5: (n,p) and (n,np) cross section for the formation of ^{96}Nb

Neutron energy (MeV)	^{96}Mo(n,p)^{96}Nb Cross section (mb)	Neutron energy (MeV)	^{97}Mo(n,np)^{96}Nb Cross section (mb)
16.22±0.05	19.9±1.8	16.23±0.04	8.1±0.7
19.33±0.07	25.1±2.5	19.28±0.13	30.6±4.2
20.63±0.08	25.3±2.7	20.64±0.13	37.6±4.1

^{97}Mo(n,np)^{96}Nb: Measurement of the ^{97}Mo(n,np)^{96}Nb reaction cross section was only possible using an isotopically enriched sample. The measured cross sections are given in Table 5.5 and are plotted together with two other existing data sets in the lower part of Figure 5.8. The two measurements by Atsumi *et al.* [114] and Ikeda *et al.* [95] were done only in the 14 MeV region and could thus only give the trend of the excitation function. The new mesurement presented here allows to establish an excitation function up to a maximum energy of 20.6 MeV. It can be seen that the data are not consistently described by the evaluation and the calculation. The STAPRE calculation, which was done without a knowledge of the new data, describes well the older data in the 14 MeV region, but heavily overpredicts the cross sections for energies higher than 15 MeV. In that energy region the JENDL-3.2 evaluation agrees with the measurements within the given uncertainties, but it is too low compared to the older data. The EAF-99 evaluation is about 50% too low over the whole energy range.

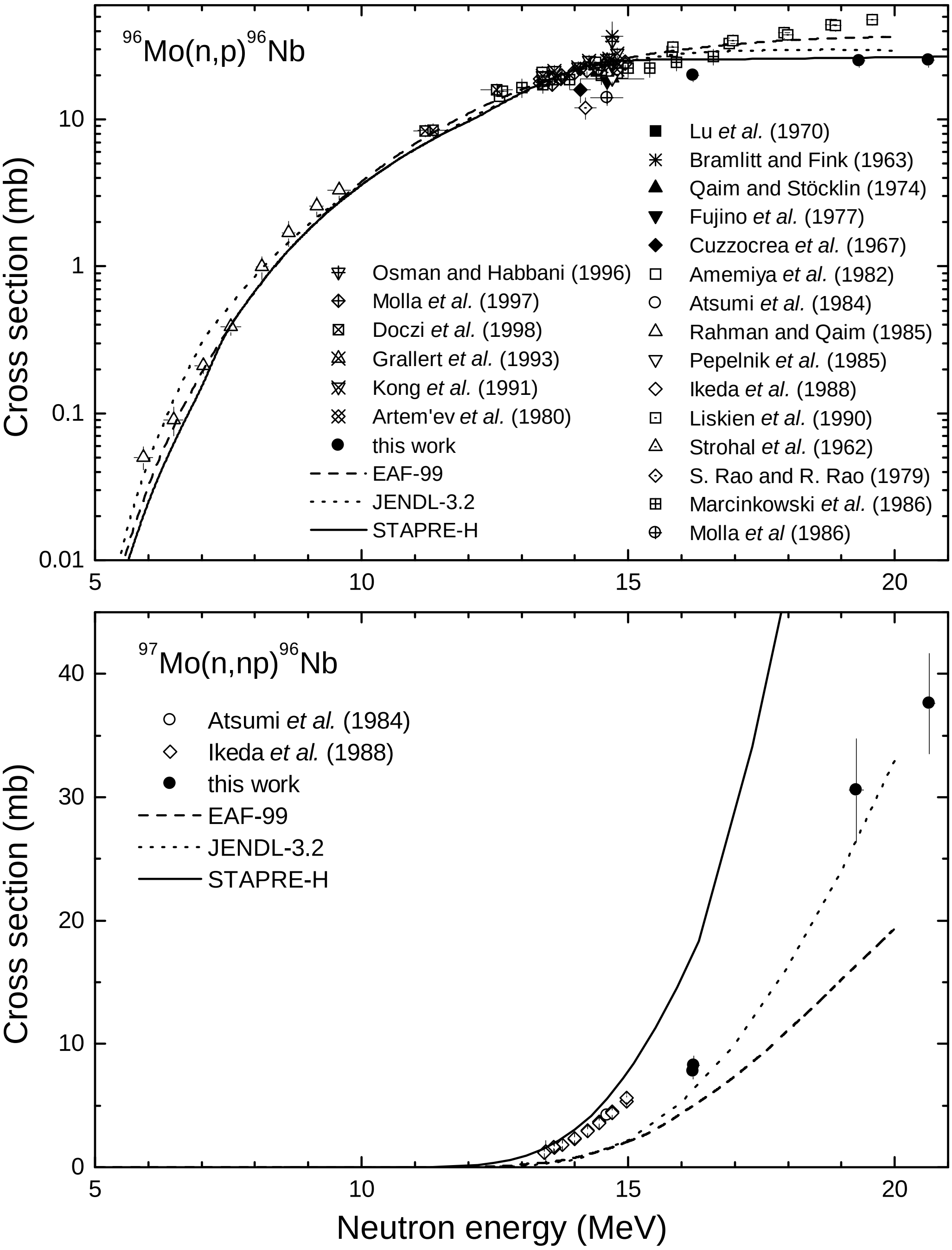

Figure 5.8: Comparison of the measured cross sections for the ^{96}Mo(n,p)^{96}Nb and ^{97}Mo(n,np)^{96}Nb reactions with existing experimental data [89, 95, 98, 103, 105–107, 109, 112–116, 120–123, 126, 128, 129], evaluations and STAPRE-H calculations.

5.2.1.4 (n,p) and (n,np) reactions lading to $^{97\mathrm{m}}$Nb and $^{97\mathrm{m+g}}$Nb

Using enriched ^{97}Mo and ^{98}Mo isotopes (for isotopic composition see Table 3.1, page 18), it was possible to distinguish the formation of both the ground and the metastable states of ^{97}Mo via the (n,p) and (n,np) reactions. The four involved reactions are dicussed in more detail in the following paragraphs. The measured reaction cross sections are given in Table 5.6.

Table 5.6: (n,p) and (n,np) cross sections for the formation of $^{97\mathrm{m}}$Nb and$^{97\mathrm{m+g}}$Nb

Neutron energy (MeV)	^{97}Mo(n,p)$^{97\mathrm{m}}$Nb Cross section (mb)
16.18±0.07	5.4±0.5
17.83±0.12	6.4±1.4
19.19±0.16	6.3±1.0
20.50±0.18	6.6±2.2

Neutron energy (MeV)	^{97}Mo(n,p)$^{97\mathrm{m+g}}$Nb Cross section (mb)
16.23±0.04	18.2±1.3
18.01±0.13	19.4±2.7
19.28±0.13	22.4±2.9
20.64±0.07	19.3±1.7

Neutron energy (MeV)	^{98}Mo(n,np)$^{97\mathrm{m}}$Nb Cross section (mb)
16.15±0.09	1.9±0.2
17.83±0.12	9.4±1.9
19.18±0.17	14.2±1.5
20.56±0.09	25.5±7.1

Neutron energy (MeV)	^{98}Mo(n,np)$^{97\mathrm{m+g}}$Nb Cross section (mb)
16.22±0.09	2.9±0.2
18.02±0.12	12.8±1.7

^{97}Mo(n,p)$^{97\mathrm{m}}$Nb: This cross section has been measured for four energies between 16 and 21 MeV and the results are shown in the upper part of Figure 5.9. Several measurements existed so far between 13 and 15 MeV, but there was only one dataset from MARCINKOWSKI *et al.* [121] at higher energies. However, this result for 16.6 MeV shows rather large uncertainties. Our results are in good agreement with these data and are well described by both the STAPRE calculations and the EAF-99 evaluation, which happen to be almost identical for neutron energies above 17 MeV.

^{98}Mo(n,np)$^{97\mathrm{m}}$Nb: Since this measurement is impossible to perform without enriched samples, only four datasets exist, all in the 14 MeV region [95, 101, 113, 130]. Our data are in good agreement with the trend of the excitation function, given by these older measurements. The STAPRE calculation describes very well the three highest datapoints, but it overpredicts our lowest datapoint at 16.1 MeV and underpredicts the old 14 MeV data. The EAF-99 evaluation is about one order of magnitude too low over the whole energy region.

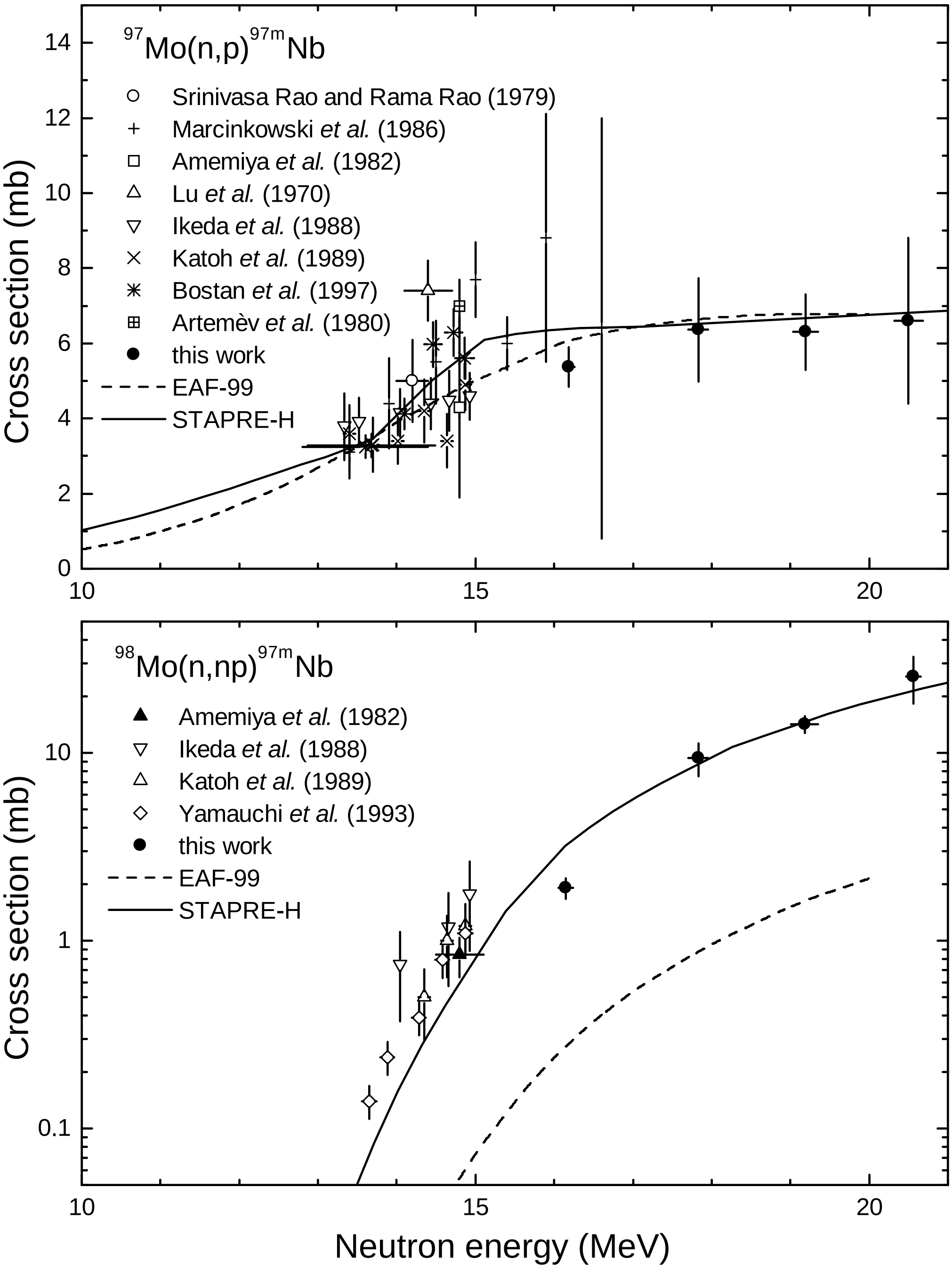

Figure 5.9: Comparison of the measured cross sections for the ^{97}Mo(n,p)^{97m}Nb and ^{98}Mo(n,np)^{97m}Nb reactions with existing experimental data [95, 101, 106, 107, 113, 121, 123, 130, 131], evaluations and STAPRE-H calculations.

^{97}Mo(n,p)$^{97m+g}$Nb: Measurements were done for the formation of $^{97m+g}$Nb, i. e. the couting of the activated sample was only started, when the metastable state with a half-life of 58.7 s (Table 3.6, page 31) had completly decayed. The results are presented graphically in the upper part of Figure 5.10 together with the cross sections found in the literature. This reaction has been studied extensivly, especially in the 14 MeV region, but also some data exist for the threshold region [106, 115]. However, no data existed up to now for energies above 17 MeV. Both the model calculation and the EAF-99 evaluation confirm our data and the flat behaviour of the excitation function above 16 MeV. In the threshold region on the other hand, the model describes the more recent data of Rahman and Qaim (1985) [115] better, while the EAF-99 curve follows more the older data of Artemev (1980) [106].

^{98}Mo(n,np)$^{97m+g}$Nb: Using an enriched ^{98}Mo sample it was possible to add two data-points to the existing two measurements of Ikeda *et al.* [95] and Amemiya *et al.* [113]. The data are compared with evaluations and a STAPRE calculation in Figure 5.10 (lower part). Our new results do not quite follow the trend given by the 14 MeV data, but they agree to some extent with the JENDL-3.2 evaluation, which is somewhat low compared to our 18 MeV data point. EAF-99 is even lower, but gives the same shape of the exitation function. The STAPRE calculation describes well only the older 14 MeV data, but it overpredicts our new results.

5.2.2 Some (n,α) and (n,2n) cross sections

In addition to the above discussed (n,p) and (n,np) reactions some (n,α) and (n,2n) reactions relevant to gas production and neutron transport habe been studied as well. In the following paragraphs we will discuss the (n,α) reactions on ^{92}Mo and ^{100}Mo and the (n,2n) reactions on ^{92}Mo, ^{94}Mo and ^{100}Mo in a bit more detail.

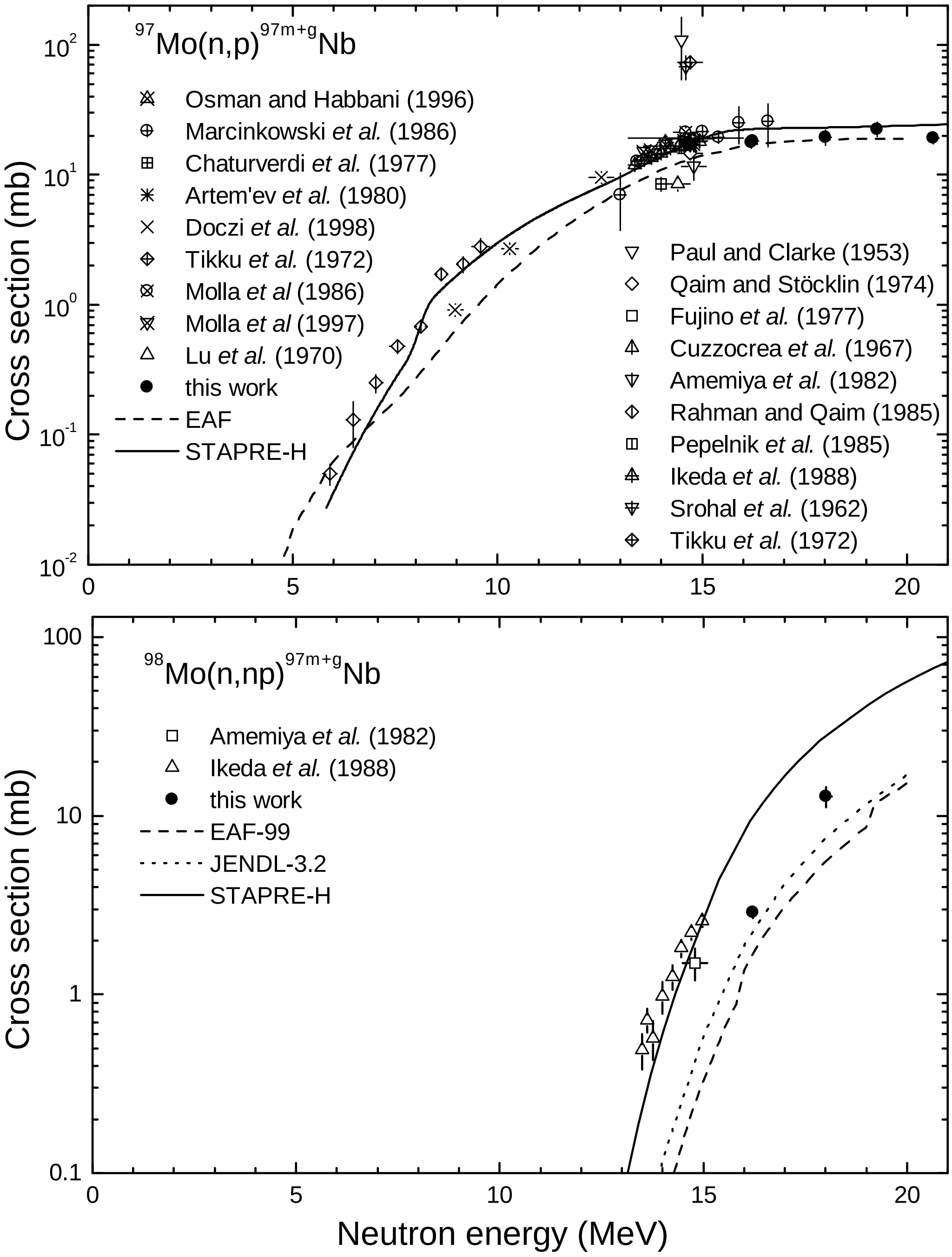

Figure 5.10: Comparison of the measured cross sections for the ^{97}Mo(n,p)$^{97m+g}$Nb and ^{98}Mo(n,np)$^{97m+g}$Nb reactions with existing experimental data [95,98,103,105–107,112,113,115, 116,120–122,126,129,132–134],evaluations and STAPRE-H calculations.

5.2.2.1 ^{92}Mo(n,α)^{89m}Zr reaction

The present data for the ^{92}Mo(n,α)^{89m}Zr reaction are given in Table 5.7 and plotted in Figure 5.11 together with existing data, evaluations and model calculation. The majority of the existing data were measured with 14 MeV neutrons, but the scatter in the data is large. One data set exists for energies up to 17 MeV by MARCINKOWSKI *et al.* [121], but their results are much higher than our values. The data of MARCINKOWSKI *et al.* suggest a continous rise of the cross section, while our data propose an almost flat behaviour. The EAF-99 evaluation peaks at about 17 MeV, which is not confirmed by our data. The STAPRE calculation gives a slightly downward slope of the excitation function, which agrees with the new experimental result only within the uncertainties, which are rather large for the highest energy point.

Table 5.7: Measured cross sections for the ^{92}Mo(n,α)^{89m}Zr reaction

Neutron energy (MeV)	Cross section (mb)
16.1±0.1	6.3±0.7
17.8±0.2	6.7±1.0
19.1±0.3	6.3±1.0
20.5±0.2	6.6±2.5

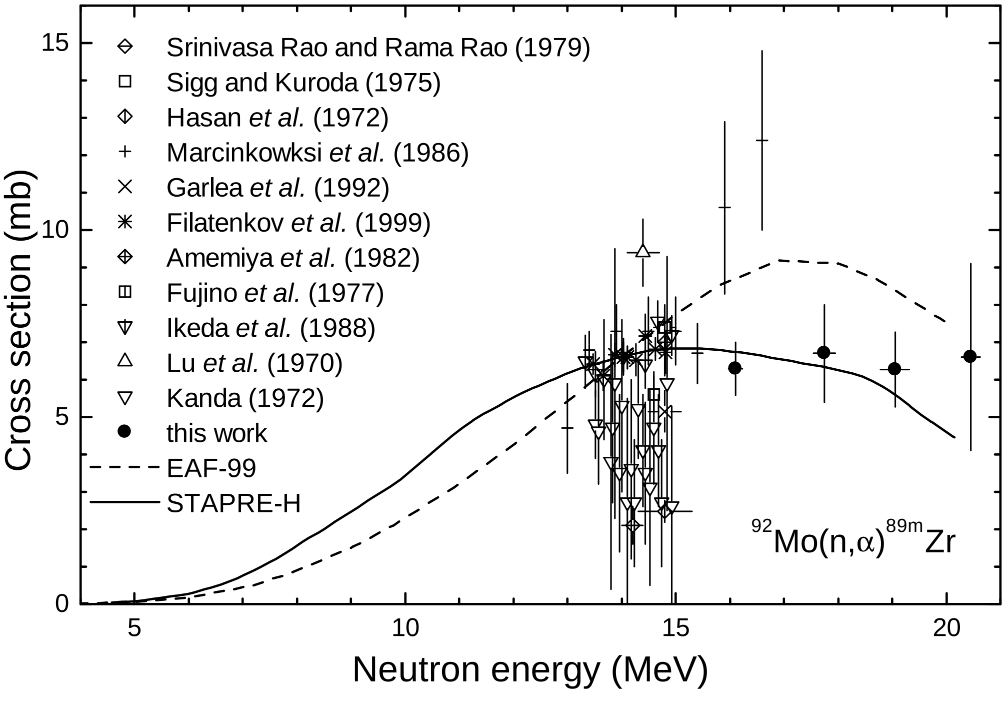

Figure 5.11: Comparison of the measured cross sections for the ^{92}Mo(n,α)^{89m}Zr and reaction with existing experimental data [95, 99, 102, 107, 108, 110, 112, 113, 121, 123, 135], evaluations and STAPRE-H calculations.

5.2.2.2 ^{100}Mo(n,α)^{97}Zr reaction

The experimental results for the ^{100}Mo(n,α)^{97}Zr reaction are given in Table 5.8. From Figure 5.12 it can be seen that our new data are in good agreement with the only other dataset above 17 MeV, measured by LISKIEN *et al.* [42]. The evaluated data file EAF-99, which is identical to JENDL-3.2, is somewhat lower than our data, but gives the right shape of the excitation function. It agrees nicely with the 14 MeV data. The situation for the STAPRE calculation is almost the opposite: good agreement is observed with the data at higher energies, while the model underestimates the cross section at 14 MeV.

Table 5.8: Measured cross sections for the ^{100}Mo(n,α)^{97}Zr reaction

Neutron energy (MeV)	Cross section (mb)
16.2±0.3	3.4±0.2
18.0±0.1	4.6±0.4
19.3±0.1	5.3±0.5
20.5±0.1	5.2±0.5

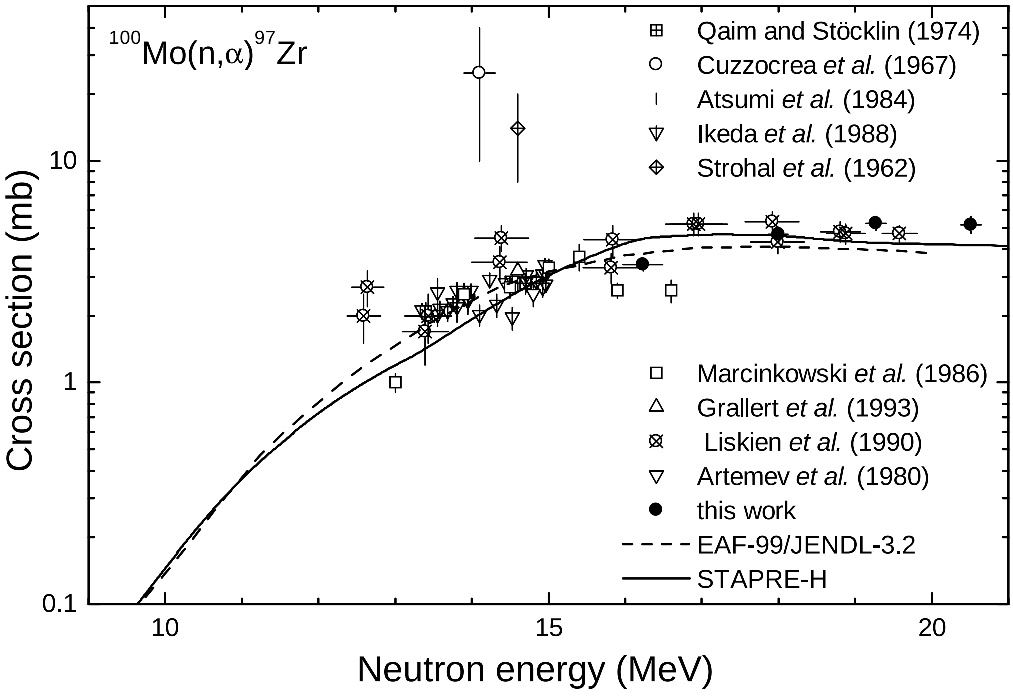

Figure 5.12: Comparison of the measured cross sections for the ^{100}Mo(n,α)^{97}Zr reaction with existing experimental data [42,89,95,106,114,120,121,129], evaluations and STAPRE-H calculations.

5.2.2.3 ^{92}Mo(n,2n)^{91m}Mo reaction

The measured cross sections for the ^{92}Mo(n,2n)^{91m}Mo reaction are given in Table 5.9 and are presented graphically in Figure 5.13. Most of the existing data were measured with 14 MeV neutrons. Some data are consistent while others and are rather discrepant. The only dataset above 14 MeV by MARCINKOWSKI *et al.* [121] is in good agreement with the present data. A good description of the data was obtained using the STAPRE code. It reproduces the present data nicely and also agrees with the most recent work by FILATENKOV *et al.* [99] in the 14 MeV region. The EAF-99 evaluation on the other hand underestimates the cross section for energies above 15 MeV and overestimates the cross sections for energies below 15 MeV.

Table 5.9: Measured cross sections for the ^{92}Mo(n,2n)^{91m}Mo reaction

Neutron energy (MeV)	Cross section (mb) (mb)
16.1±0.1	54.9±4.7
17.8±0.2	100±21
19.1±0.2	117±13
20.5±0.2	118±21

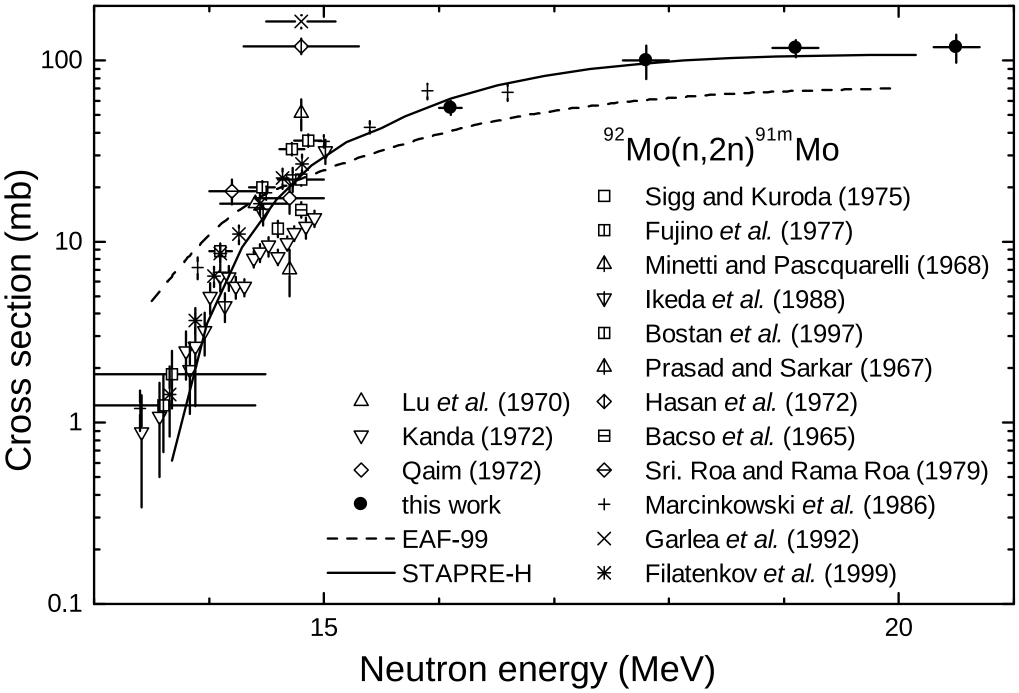

Figure 5.13: Comparison of the measured cross sections for the ^{92}Mo(n,2n)^{91m}Mo reaction with existing experimental data [95, 99, 102, 107, 108, 110, 112, 121, 123, 131, 135–139], evaluations and STAPRE-H calculations.

5.2.2.4 ^{94}Mo(n,2n)^{93m}Mo reaction

The numerical results for the ^{94}Mo(n,2n)^{93m}Mo reaction can be found in Table 5.10 while Figure 5.14 contains the graphical representation of the measured cross sections. Our lowest energy point at 16.2 MeV neutron energy is somewhat lower than the previous data by HERMAN and MARCINKOWSKI [84]. The three other data points, however, are in very good agreement with the trend of the experimental data in the 14 MeV region and the EAF-99 evaluation. A good description over the whole energy range was obtained by the nuclear model calculations done using the code STAPRE-H.

Table 5.10: Measured cross sections for the ^{94}Mo(n,2n)^{93m}Mo reaction

Neutron energy (MeV)	Cross section (mb) (mb)
16.2±0.3	9.6±0.8
18.0±0.1	22.0±1.8
19.3±0.1	28.7±2.4
20.5±0.1	35.9±3.7

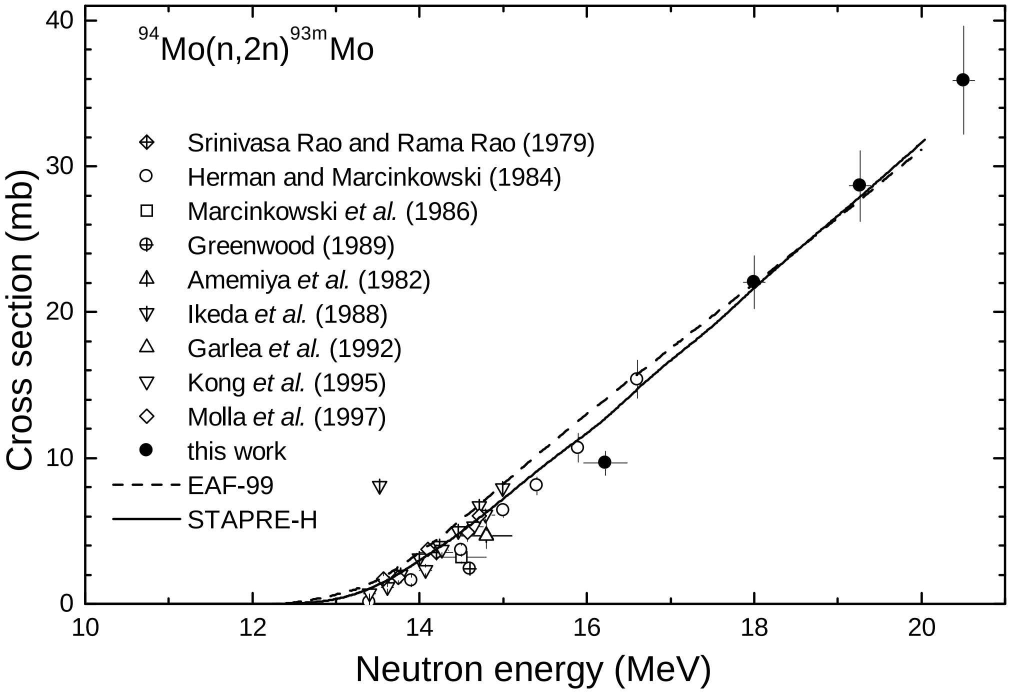

Figure 5.14: Comparison of the measured cross sections for the ^{94}Mo(n,2n)^{93m}Mo reaction with existing experimental data [84, 95, 102, 104, 105, 113, 121, 123, 140], evaluations and STAPRE-H calculations.

5.2.2.5 ^{100}Mo(n,2n)^{99}Mo reaction

The present data for the ^{100}Mo(n,2n)^{99}Mo reaction are given in Table 5.11 and are plotted in Figure 5.15. Only one measurement exists near the threshold, done by Rahman and Qaim [115], while around 14 MeV plenty of data exist. Above 15 MeV good agreement is observed with the only so ar existing results of Marcinkowski *et al.* [121]. Our two lowest data points also agree nicely with the EAF-99 and JENDL-3.2 evaluations, but the two data points at higher energies are somewhat too high, although the point at 19.3 MeV also agrees, taking into account the quite large uncertainties. The STAPRE-H calculation, on the other, hand agrees only with the two highest energy points and overestimates the two lower ones.

Table 5.11: Measured cross sections for the ^{100}Mo(n,2n)^{99}Mo reaction

Neutron energy (MeV)	Cross section (mb) (mb)
16.2±0.3	1272±127
18.0±0.1	980±78
19.3±0.1	1018±180
20.5±0.1	814±105

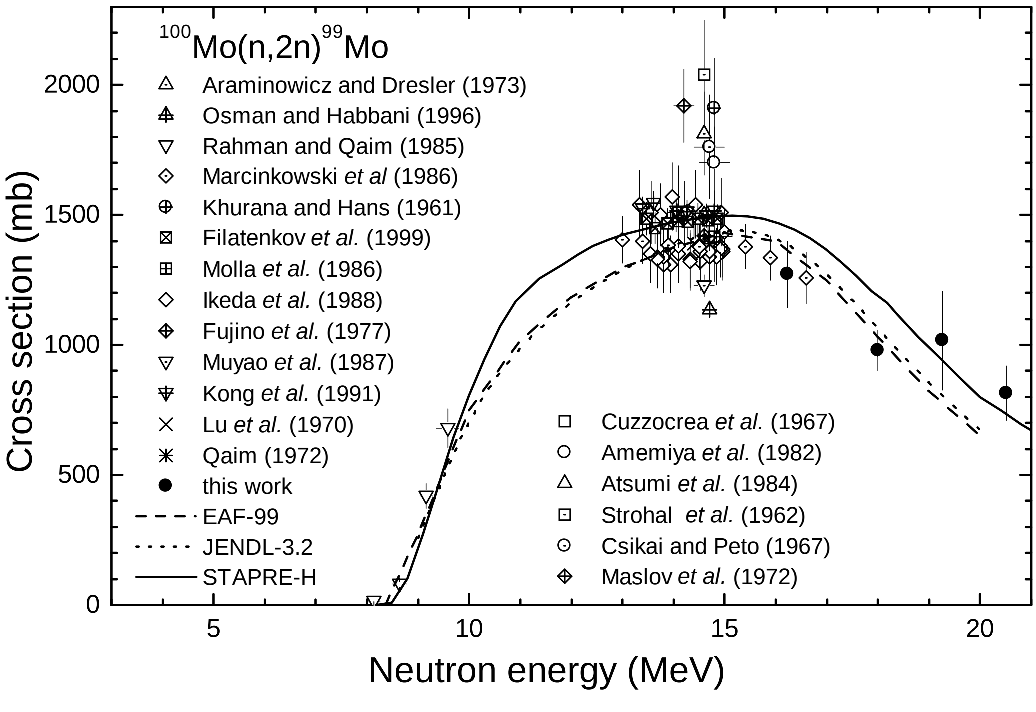

Figure 5.15: Comparison of the measured cross sections for the ^{100}Mo(n,2n)^{99}Mo reaction with existing experimental data [84, 95, 99, 103, 112–115, 120–122, 126, 131, 136, 141–145], evaluations and STAPRE-H calculations.

5.3 Technetium

5.3.1 ^{99}Tc(n,n'γ)^{99m}Tc reaction

The ^{99}Tc(n,n'γ)^{99m}Tc cross section was measured from threshold to 20.6 MeV using three different neutron producing reactions: PT for neutron energies from 0.48 to 5.91 MeV, DD from 7.47 to 12.42 MeV and DT from 13.88 to 20.59 MeV. All measurements above 6 MeV were done relative to the ^{27}Al(n,α)^{24}Na standard reaction, whereas for lower energies the ^{115}In(n,n'γ)^{115m}In reaction was used as reference. The numerical data are given in Table 5.12 and are plotted together with the results of a STAPRE model calculation in Figure 5.16.

Table 5.12: Cross sections for the ^{99}Tc(n,n'γ)^{99m}Tc reaction

Neutron energy (MeV)	Cross section (mb)
0.48±0.08	6.3±3.9
0.98±0.06	78.5±11.8
2.02±0.04	211.0±17.0
2.98±0.03	222.8±19.0
3.97±0.03	239.0±20.1
4.93±0.03	323.0±30.4
5.43±0.02	318.0±39.0
5.91±0.01	310.0±41.0
7.47±0.20	309.1±19.2
8.62±0.22	297.4±16.2
9.56±0.23	269.0±21.7
10.72±0.24	204.8±22.6
12.42±0.29	110.1±19.9
13.88±0.15	77.4±4.8
14.36±0.20	77.1±6.8
14.81±0.19	64.8±4.0
16.26±0.26	60.8±5.4
17.99±0.13	56.2±6.2
19.34±0.10	63.8±10.2
20.59±0.10	71.2±22.5

This measurement allows for the first time the establishment of an excitation function for the ^{99}Tc(n,n'γ)^{99m}Tc reaction from threshold to 20.6 MeV. So far only data around 14 MeV existed. Rather good agreement is observed with Goldstein [45] and one of the two data points of Ikeda *et al.* [46]. On the other hand, the differences to earlier works of Qaim [44] and Golchert *et al.* [43] are significant. The model calculation given in this work describes the data well in the energy range between 5 and 16 MeV. Below 5 MeV the model gives too high values and peaks at about 2 MeV. This peak appears unreal and this may have several explanations. First, the knowledge of the feeding of the isomeric state from the known discrete states may be incomplete. The isomeric state is fed by the negative parity discrete levels and the connection between the negative parity discrete

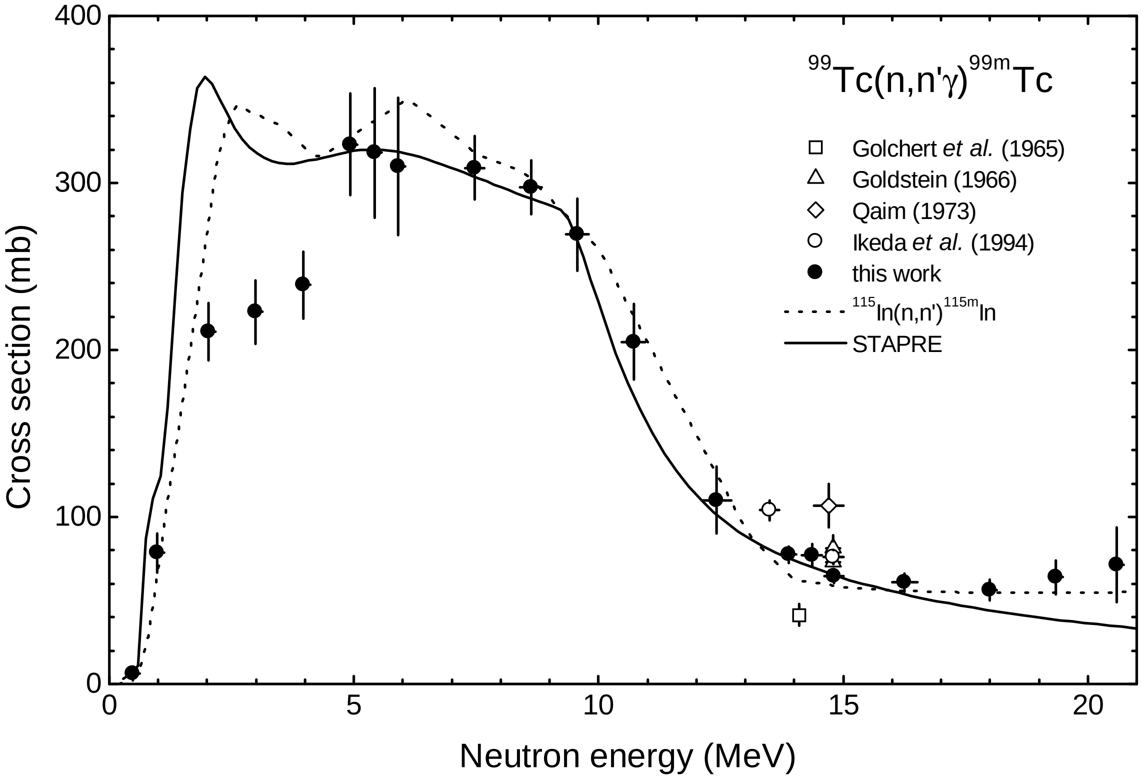

Figure 5.16: Comparison of the measured cross sections for the ^{99}Tc(n,n'γ)^{99m}Tc reaction with existing data in the 14 MeV region [43–46]and the STAPRE calculation.

levels and the continuum has a step while the number of the negative parity levels is 25% of the full number of discrete levels. In contrast, above 16 MeV the experimental cross section exceeds the model estimates. This is presently not well understood but may again be due to the level density model, the detailed feeding of the isomer and/or the pre-equilibrium model. One may note that the relative constancy of the measured isomer yield is rather similar to level yields obtained experimentally in other works such as those on (n,n'γ) and (n,xnγ) channels.

Inelastic scattering cross sections are difficult to measure with the acivation technique especially at higher energies. Low energy background neutrons and breakup neutrons play a significant role and contribute appreciably to the measured activity due to the generally low threshold of these reactions. So far only a few (n,n') reactions have been studied in detail, which are listed in Table 5.13. The present measurement thus strengthens the database to some extent.

5.3.2 ^{99}Tc(n,p)^{99}Mo and ^{99}Tc(n,α)^{96}Nb reaction

The measured cross sections for the ^{99}Tc(n,p)^{99}Mo and ^{99}Tc(n,α)^{96}Nb reactions are given in Table 5.14. The measured and calculated cross sections for the ^{99}Tc(n,p)^{99}Mo reaction are plotted together with the available literature values and evaluations in Figure 5.17. Good agreement was found with the recent measurement of Ikeda *et al.* [46] and Qaim [44]. However, large discrepancies can be observed with the results of Goldstein [45] and Golchert *et al.* [43]. The latter value is 50 % lower. Apparently both the

Table 5.13: Some inelastic scattering cross sections

Reaction	Reference	Energy (MeV)[a]	Half-life
^{89}Y(n,n'γ)^{89m}Y	[98]	0.909	16.03 s
^{99}Tc(n,n'γ)^{99m}Tc	this work	0.142	6.01 h
^{93}Nb(n,n'γ)^{93m}Nb	[146, 147]	0.031	16.13 y
^{115}In(n,n'γ)^{115m}In	[61]	0.336	4.486 h
^{103}Rh(n,n'γ)^{103m}Rh	[148]	0.040	56.12 min

[a] of the metastable state

JENDL-3.2 and the JEF 2.2 evaluations, the latter being identical to EAF and FENDL, have been normalised to the earlier 14-MeV data. While the JENDL evaluation slightly overestimates the excitation curve but otherwise shows the same shape, the JEF evaluation predicts a sharp maximum at about 13 MeV and a following steep decrease, in strong contrast to the data. Our model calculation describes the experimental values well over the whole energy range.

Also in the case of the ^{99}Tc(n,α)^{96}Nb reaction, which is shown in Fig. 5.18, good agreement was observed with the work of Ikeda *et al.* [46]. The value of Golchert *et al.* [43] is again about 50 % too low. Qaim [44] and Goldstein [45] report cross sections, which are 15–20 % higher than the present measured values. This also causes the overestimation of the JENDL-3.2 and JEF 2.2 evaluations, which are again normalised to those earlier 14 MeV data. Also in this case the JEF evaluation is identical to the FENDL and EAF evaluations. Up to about 19 MeV the present model calculations represent the experimental data very well. Only for higher energies does one observe a somewhat steeper decrease of the measured values that is not followed by the calculations.

Table 5.14: Cross sections for the ^{99}Tc(n,p)^{99}Mo and ^{99}Tc(n,α)^{96}Nb reactions

Neutron energy	Cross section (mb)	
(MeV)	^{99}Tc(n,p)^{99}Mo	^{99}Tc(n,α)^{96}Nb
8.62±0.22	1.1±0.2	0.6±0.1
9.75±0.23	2.5±0.1	1.1±0.1
10.55±0.24	4.2±0.3	1.7±0.1
11.62±0.27	5.9±0.5	2.5±0.2
12.42±0.28	9.0±0.8	3.4±0.3
13.88±0.16	11.3±0.6	4.5±0.3
14.36±0.20	13.6±1.2	5.7±0.5
14.81±0.18	14.6±1.1	6.1±0.6
16.16±0.26	14.3±0.9	6.3±0.3
17.82±0.19	15.0±0.8	6.3±0.3
19.14±0.21	14.3±0.9	5.8±0.4
20.43±0.18	16.1±1.3	5.3±0.4

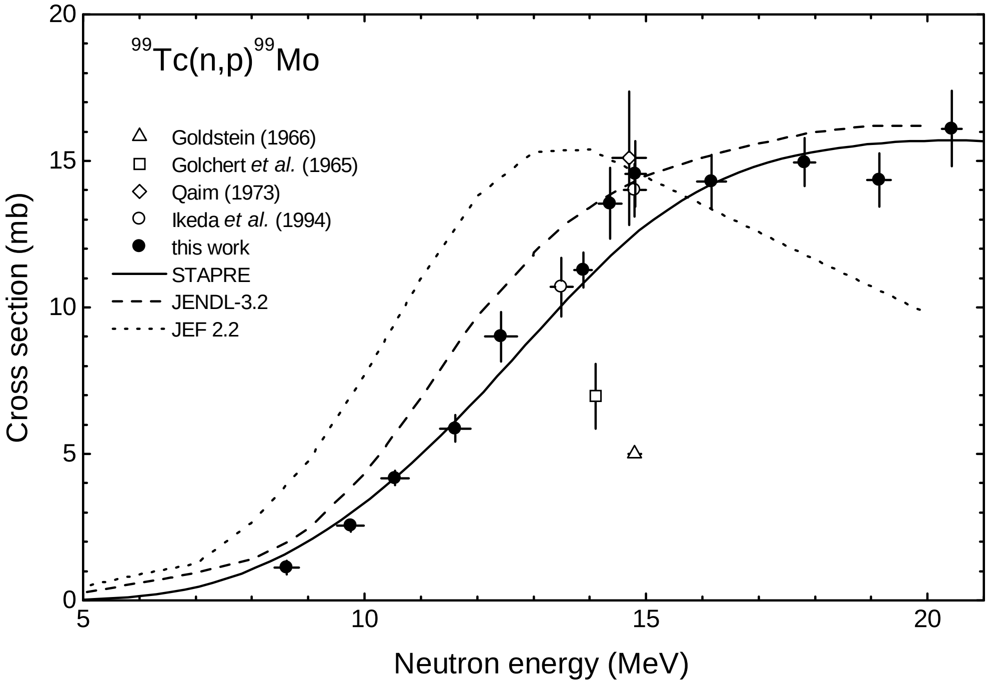

Figure 5.17: Comparison of the measured reaction cross sections for the ^{99}Tc(n,p)^{99}Mo reaction with existing data in the 14 MeV region [43–46], evaluations and a STAPRE calculation.

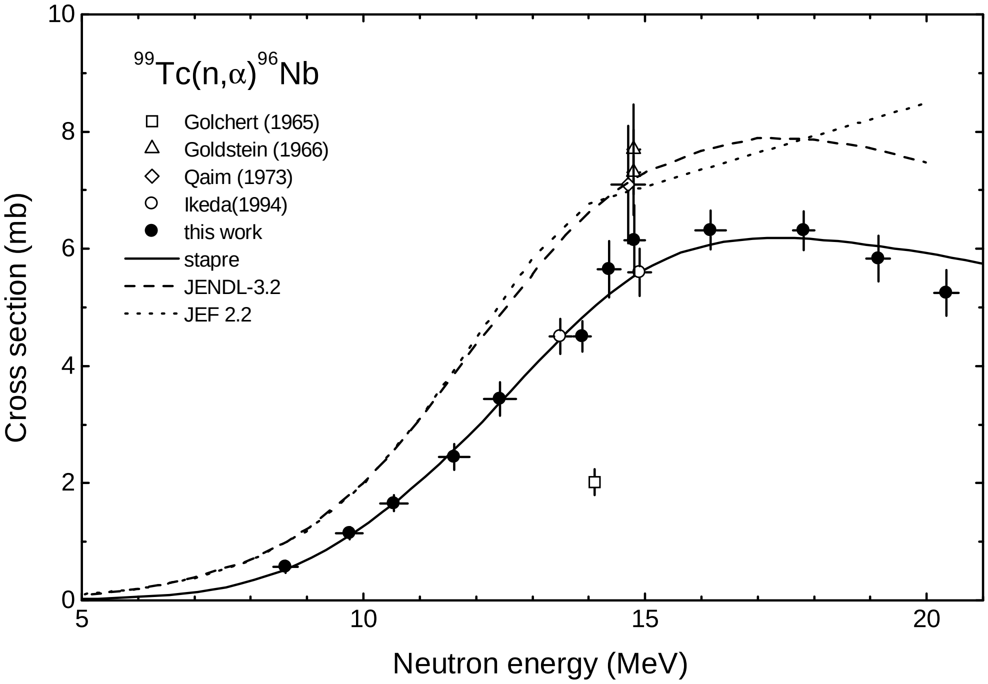

Figure 5.18: Comparison of the measured reaction cross sections for the ^{99}Tc(n,α)^{96}Nb reaction with existing data in the 14 MeV region [43–46], evaluations and a STAPRE calculation.

5.4 Lead

Both neutron emission and charged particle emission cross sections have been measured for ^{204}Pb and ^{206}Pb. The measured data are compared with the existing data from the literature and to the evaluated data files, wherever they exist. For some reactions the data are compared with the STAPRE calculations done using different optical model potentials, namely those of Bersillon-Cindro [88] and Koning [149] (see Section 4 on Model calculations).

5.4.1 ^{nat}Pb(n,x)^{204}Tl reaction

The investigations on the target material lead were mainly motivated by the determination of the formation cross section of ^{204}Tl. So far no data existed for this reaction and the existing evaluations are rather discrepant, as one can see from Figure 5.19. Measuring this cross section by the activation technique is only possible by combining a radiochemical separation method with low level beta counting. We determined the ^{204}Tl activity via Liquid Scintillation Counting. The final results are given in Table 5.15.

Our present results confirm to some extent the EAF-99 evaluation, which agrees within the error bars for two of the three lowest data points. The steep rise of the excitation function suggested by our data is not found in any evaluation. Also the nuclear model calculations performed with the code STAPRE do not predict the experimental values, they overestimate the cross sections by a factor of 2 to 3 and give an excitation function which is higher than all evaluations.

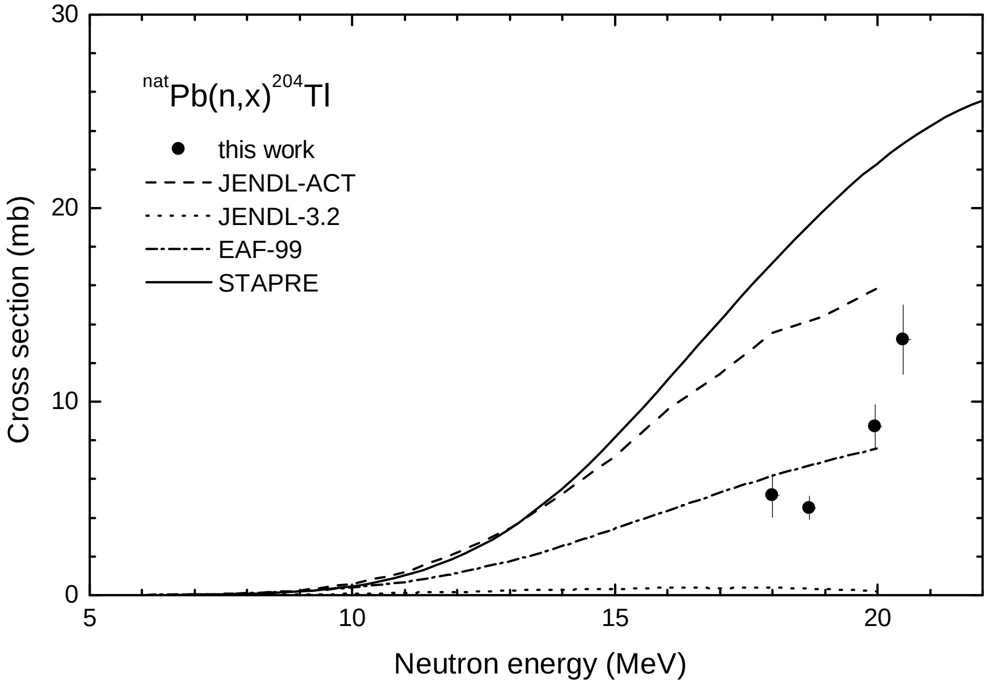

Figure 5.19: Comparison of the measured reaction cross sections for the ^{nat}Pb(n,x)^{204}Tl and ^{206}Pb(n,α)^{203}Hg reaction with existing data [89,99, 145,150], evaluations and STAPRE calculations.

^{204}Tl can be formed via several reactions, when a lead sample of natural isotopic composition is exposed to fast neutrons: The dominant reaction certainly is ^{204}Pb(n,p)^{204}Tl, but since the isotopic abundance of ^{206}Pb is about 18 times higher than that of ^{204}Pb, also the ^{206}Pb(n,t)^{204}Tl might play a role, although the cross section is expected to be rather small. Also possible are contributions from the (n,2n) reaction on ^{205}Tl, which is a frequent impurity in Pb samples. In this case special care was taken to use a very high purity lead sample in order to avoid contamination from the latter reaction, which has a high cross section. It is estimated that the total contribution to the formation of ^{204}Tl from the interfering reaction ^{205}Tl(n,2n)^{204}Tl is less than 5%.

Table 5.15: Cross sections for the ^{nat}Pb(n,x)^{204}Tl reaction

Neutron energy (MeV)	Cross section (mb)
20.5±0.1	13.2±1.8
20.0±0.1	8.7±1.1
18.7±0.1	4.5±0.6
18.0±0.1	5.1±1.1

5.4.2 ^{206}Pb(n,α)^{203}Hg reaction

Experiments were not devoted to the study of the ^{206}Pb(n,α)^{203}Hg reaction, but prior to the chemical processing of the Pb samples, γ-ray spectrometry was performed, allowing the calculation of the (n,α) cross section. Care was taken to guarantee a cooling time long enough to allow ^{203g}Pb to decay, which emits a γ-ray of the same energy as ^{203}Hg (279 keV). The numerical results of our measurments are given in Table 5.16 and are plotted in Figure 5.20 together with the existing experimental data in the 14 MeV region. Our Data are in good agreement with the trend provided by the older measurements, although the data point at 16 MeV seems to be rather low. JENDL-3.2 gives a good description of the shape of the excitation function, but is about 10% too high in the investigated energy range. Both JENDL-ACT and EAF-99 underestimate the cross section. The STAPRE calculation agrees very well with the measured data, except with the data point at 16 MeV.

Table 5.16: Cross sections for the ^{206}Pb(n,α)^{203}Hg reaction

Neutron energy (MeV)	Cross section (mb)
20.5±0.1	3.7±0.4
20.0±0.1	3.9±0.4
19.2±0.2	3.3±0.3
18.7±0.2	2.6±0.2
17.2±0.1	1.9±0.2
16.1±0.2	0.86±0.09

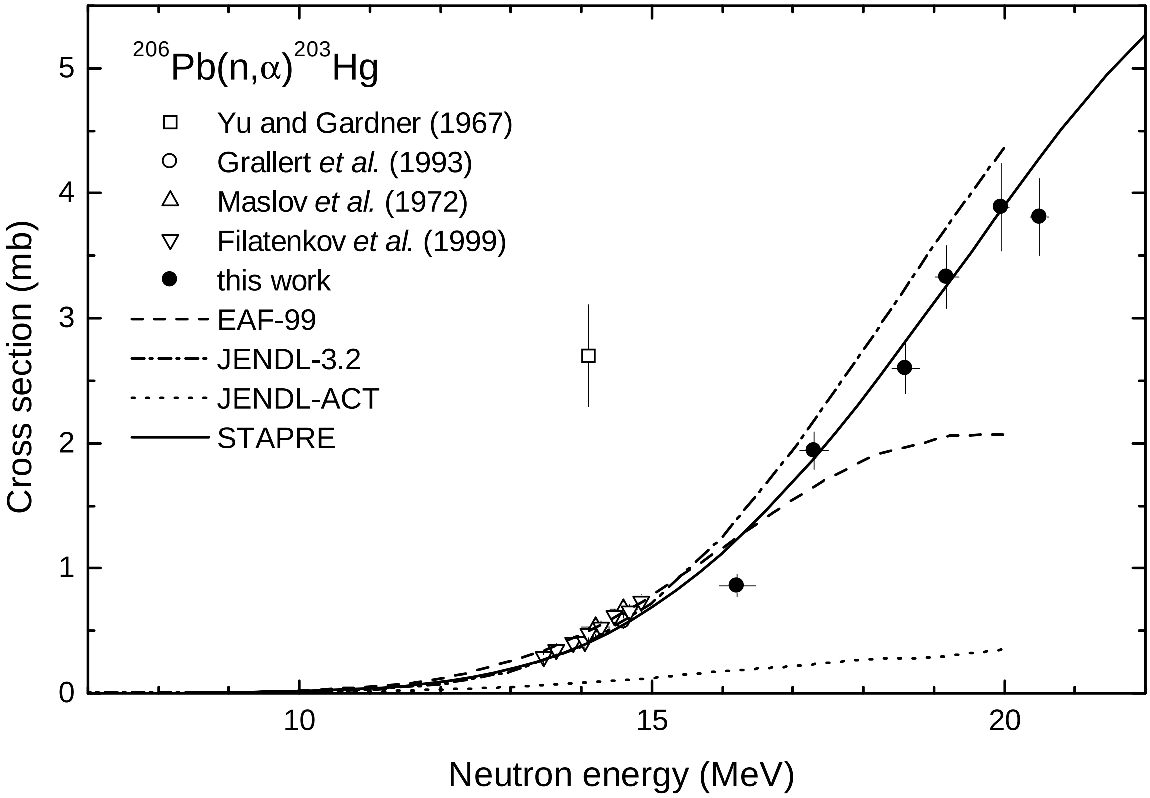

Figure 5.20: Comparison of the measured reaction cross sections for the ^{206}Pb(n,α)^{203}Hg reaction with existing experimental data [89, 99, 145, 150], evaluations and STAPRE calculations.

5.4.3 ^{204}Pb(n,2n)^{203}Pb reaction

An extensive database exists for the ^{204}Pb(n,2n)^{203}Pb reaction, which is shown in Figure 5.21 together with the present data. The numerical values can be found in Table 5.17. Our data are in good agreement with the only other measurement above 16 MeV of Vaughn [49], but our data have a much lower uncertainty. Good agreement was found with JENDL-3.2, which is only slightly higher than our values. EAF-99 on the other hand suggests a quite unusual slope of the excitation function, for which no explanation could be found: the curve shows a sudden downturn at 19 MeV and an even more remarkable peak at 10 MeV neutron energy. Nuclear model calculations have been performed using STAPRE and the Optical Model Potential of Bersillon-Cindro and Koning. Both approaches describe the data well, but the OMP of Bersillon-Cindro performs better in the here investigated energy range.

5.4.4 ^{204}Pb(n,3n)^{202m}Pb reaction

The results given in Table 5.18 are the first measurements reported for the ^{204}Pb(n,3n)^{202m}Pb reaction. It is shown graphically with the EAF-99 evaluation in Figure 5.22. Due to the lack of experimental data EAF-99 overestimates the cross section by more than an order of magnitude in some energy regions. Model calculations were again done using the STAPRE code with the OMP parameters given by Bersillon-Cindro [88] and Kon-

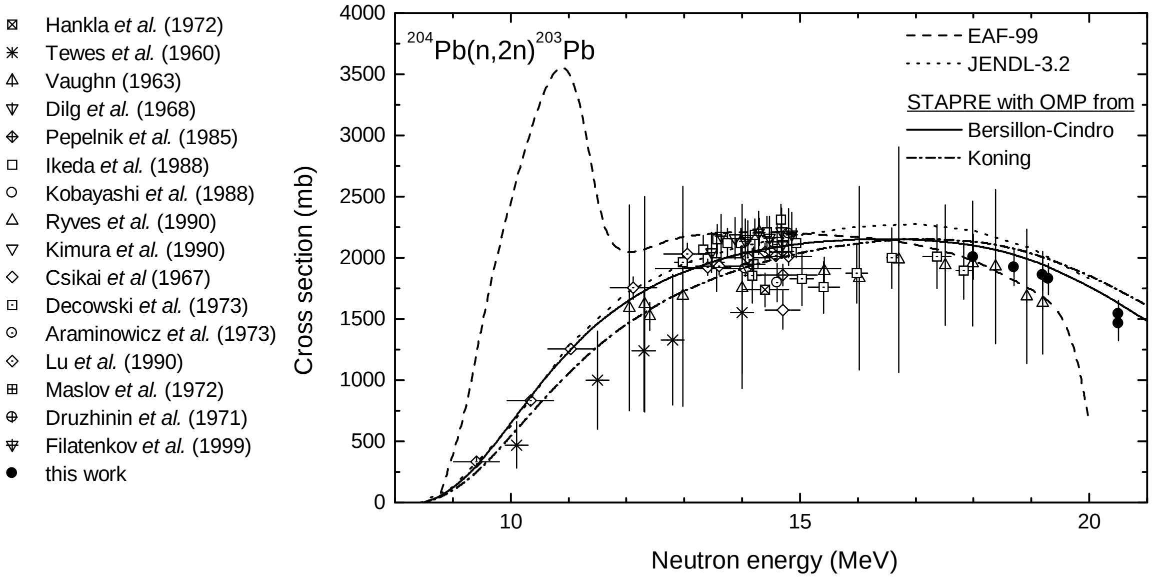

Figure 5.21: Comparison of the measured reaction cross sections for the ^{204}Pb(n,2n)^{203}Pb reaction with existing data [49, 50, 95, 99, 116, 117, 119, 141, 144, 145, 151–156], evaluations and STAPRE calculations.

Table 5.17: Cross sections for the ^{204}Pb(n,2n)^{203g}Pb reaction

Neutron energy (MeV)	Cross section (mb) (mb)
20.5±0.1	1461±140
19.4±0.1	1827±138
19.2±0.2	1852±132
18.7±0.2	1923±147
18.0±0.1	2007±185

ING [149]. Both the curves obtained using these parameters describe the experimenal data well. The parameters of BERSILLON-CINDRO result in a curve which is slightly too high, while KONINGs parameters lead to a slightly lower curve, but both calculations agree within the given uncertainties of the measurements.

Table 5.18: Cross sections for the ^{204}Pb(n,3n)^{202m}Pb reaction

Neutron energy (MeV)	Cross section (mb) (mb)
20.5±0.1	82.2±12.6
19.4±0.1	18.3±2.2
19.2±0.2	13.4±2.2
18.7±0.2	3.8±0.5
18.0±0.1	0.17±0.04

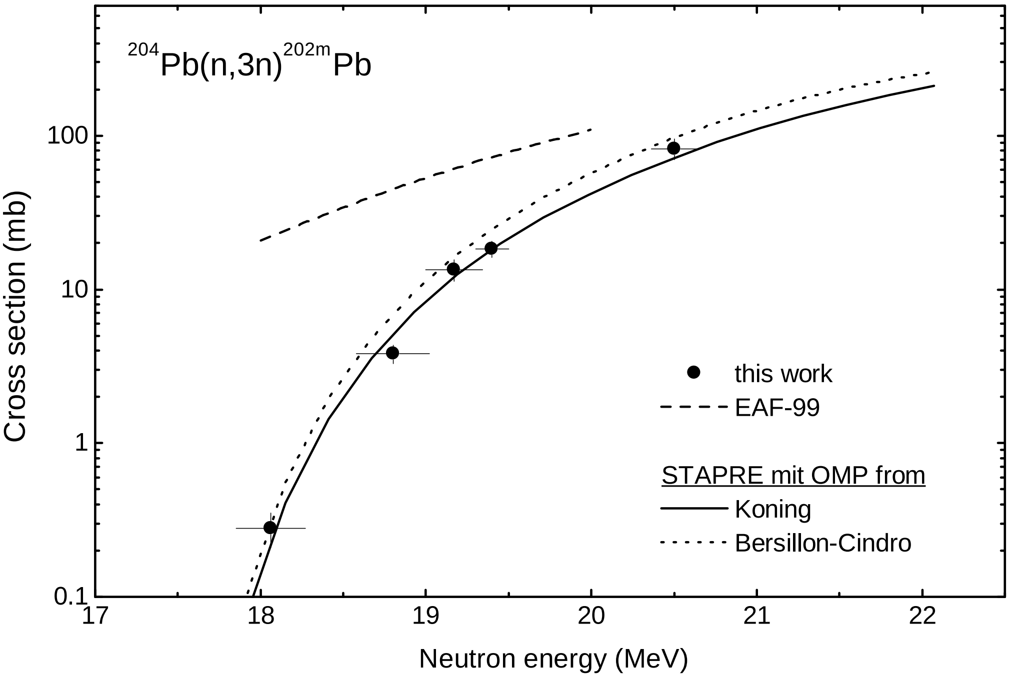

Figure 5.22: Comparison of the measured reaction cross sections for the ^{204}Pb(n,3n)^{202m}Pb reaction evaluations and STAPRE calculations.

5.4.5 ^{206}Pb(n,3n)^{204m}Pb reaction

The other (n,3n) process investigated is the ^{206}Pb(n,3n)^{204m}Pb reaction, for which already one measurement exists. It was done by WELCH *et al.* [48] for energies above 20 MeV. From Figure 5.23 it can be seen that there is a slight mismatch between the present data, given in numerical form in Table 5.19, and the previous data. The model calculation does not solve this problem, since it overestimates the data in the energy range above 22 MeV and underestimates at lower energies.

Table 5.19: Cross sections for the ^{206}Pb(n,3n)^{204m}Pb reaction

Neutron energy (MeV)	Cross section (mb)
20.7±0.1	292±31
19.4±0.1	92.1±6.4
18.1±0.1	4.2±0.3

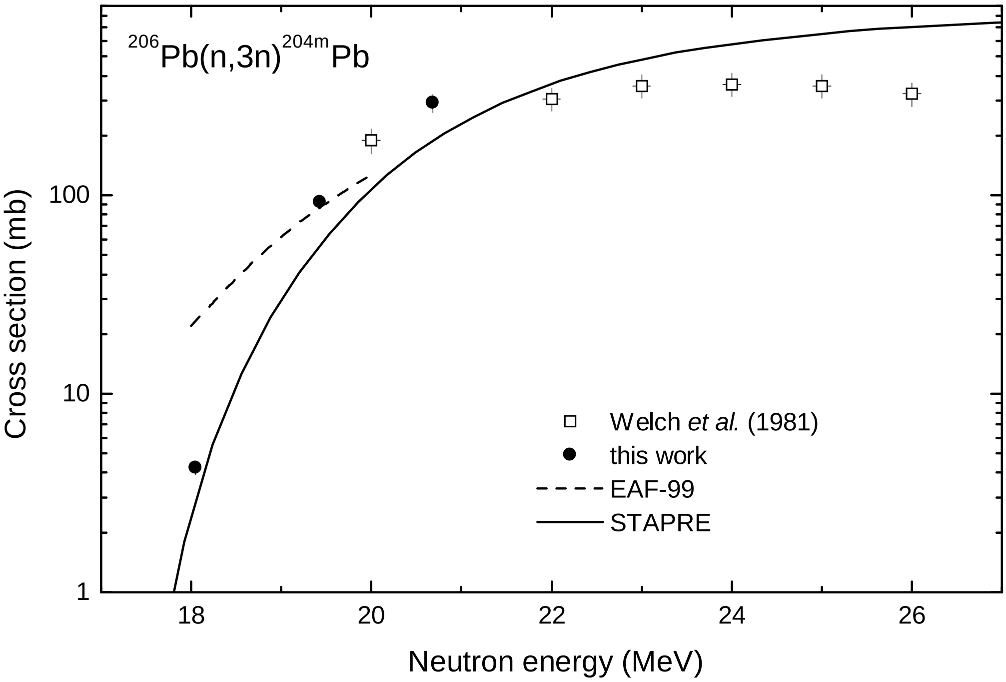

Figure 5.23: Comparison of the measured reaction cross sections for the ^{206}Pb(n,3n)^{204m}Pb reaction with existing data [48], evaluations and STAPRE calculations.

Chapter 6

Summary and Conclusions

A good knowledge of neutron induced reaction cross section data is required for testing nuclear models as well as for many practical applications, especially in the field of nuclear energy. The cross sections are needed, for example, to estimate the decay heat, activation of structural materials, gas production etc. in both present day fisson and future fusion reactors. Another field of application is transmutation of long-lived radioactive wastes in connection with Accelerator Driven Systems (ADS).

In this thesis work, excitation functions for neutron induced reactions on isotopes of V, Mo, Tc and Pb have been studied using the activation technique. In total 27 reactions have been measured in the energy range of 0.5 to 20.6 MeV. These included (n,p), (n,np), (n,α), (n,nα), (n,n'γ), (n,2n) and (n,3n) reactions on the above mentioned elements. The radioactive reaction products with half-lives between 58 seconds and 20300 years have been measured offline via high-resolution γ-ray-spectrometry and Liquid Scintillation Counting, the latter in combination with radiochemical separation. The ^{94}Nb activity was measured in the underground laboratory HADES, using ultra low-level γ-ray spectrometry.

Depending on the desired neutron energy three different neutron producing reactions and experimental setups were used. Irradiations with neutron energies in the range of 0.5 to 6 MeV were done using the ^{3}H(p,n)^{3}He reaction with a solid-state Ti/T target while energies between 7.4 and 12.5 MeV were covered with the ^{2}H(d,n)^{3}He reaction utilizing a D_2 gas target. Irradiations in the energy range from 13.4 to 20.6 MeV were performed using the ^{3}H(d,n)^{4}He reaction again with a solid Ti/T target. Most of the reactions were investigated using a specially designed low mass setup, consisting of an Al support ring, from which the samples were suspended using small Al rods. This system allows simultaneous irradiation of several samples at different angles and thus different neutron energies. The second setup was a pneumatic sample changing system, that was used to measure reactions leading to products with half-lives between 1 and 10 min. A third setup was developed for the measurement of the $^{\mathrm{nat}}$Mo(n,x)^{94}Nb reaction. The long half-life of 20300 years required a sample holder that was optimised for a maximum of sample mass, an acceptable self-absorbtion in the γ-ray spectrometry and an efficient use of required long beamtime.

Since the absolute neutron flux was not measured, all cross sections were determined relative to the ^{27}Al(n,α)^{24}Na standard cross section. The corrections applied to the data are either due to the irradiation process or due to the measurement of the induced activity. Corrections for background neutrons, breakup neutrons, flux fluctuations during the irradiation and multiple scattering belong to the first group, while corrections for coincidences, self-absorption and sample geometry belong to the second group.

Nuclear model calculations were performed for all investigated reactions. For reactions on ^{99}Tc and Pb the original STAPRE code was used, while a modified version STAPRE-H was used for reactions on V and Mo.

Measurements on vanadium were motivated by large discrepances in the production data for ^{47}Sc, compared to calculations based on EAF-97 and recent irradiations of V alloys. The $^{\mathrm{nat}}$V(n,xα)^{47}Sc cross section, which consists of contributions from the ^{51}V(n,n'α)^{47}Sc and ^{50}V(n,α)^{47}Sc processes, was measured from 11.7 to 20.5 MeV. The results show that above incident energies of 15 MeV the ^{51}V(n,n'α)^{47}Sc reaction is the main contributor, while for lower energies the ^{50}V(n,α)^{47}Sc reaction is dominant, ^{50}V having a natural isotopic abundance of 0.25%. The measurements nicely agree with the STAPRE-H calculations. In addition the ^{51}V(n,α)^{48}Sc reaction was also investigated, the measurement being only the second one above 18 MeV. The ^{51}V(n,p)^{51}Ti reaction was remeasured at two selected energies in order to fill a gap in the excitation function.

A total of 16 neutron induced reactions have been studied on the structural material Mo. The most challenging among these was the production of ^{94}Nb. It is formed via the ^{94}Mo(n,p) and ^{95}Mo(n,np) reactions. A large sample of about 1.5 kg Mo was irradiated in a specially developed sample holder for 100 h, giving three energy points. Two of the samples were measured in the underground laboratory HADES, while the third one was chemically processed with subsequent standard γ-ray spectrometry. It was possible to construct for the first time an excitation function for the $^{\mathrm{nat}}$Mo(n,x)^{94}Nb process, which is in good agreement with the two existing mesurements at 14 MeV. The use of enriched samples allowed the distinction between (n,p) and (n,np+pn+d) contributions to the same activity. The ^{94}Mo(n,2n)$^{93\mathrm{m}}$Mo and ^{100}Mo(n,2n)^{99}Mo reactions could also be advantageously studied through the use of enriched samples by suppressing the contributions from the (n,γ) process to the activity. A comparison with the EAF-99 library could be made for all the reactions studied, whereas in case of JENDL-3.2 comparisons are only for reactions with non-isomeric final states. A comparison with the model estimates shows that calculated values agree fairly well with the experimental data except for the ^{97}Mo(n,np)^{96}Nb and ^{98}Mo(n,np)$^{97\mathrm{m+g}}$Nb reactions and, to a lesser extent, the ^{100}Mo(n,α)^{97}Zr reaction. In most cases the model calculations agree more closely with the data than the EAF-99 evaluation. When available, the JENDL-3.2 evaluation gives a similar level of agreement except in the case of ^{97}Mo(n,np)^{96}Nb reaction where it agrees better, and in the case of ^{100}Mo(n,α)^{97}Zr reaction where it is slightly worse.

Three neutron induced reactions on the radioactive fission product ^{99}Tc have been measured from threshold to 20.6 MeV. These reactions are ^{99}Tc(n,n'γ)$^{99\mathrm{m}}$Tc, ^{99}Tc(n,p)^{99}Mo and ^{99}Tc(n,α)^{96}Nb. For all these reactions only four datasets could be found in the literature, all done in the 14 MeV region. The induced radioactivity was measured via γ-ray spectrometry using a Pb absorber between the sample and the detector in order to suppress the Bremsstrahlung. To date full excitation function of the (n,n'γ) process has been determined only for a few target nuclei. This measurements thus strengthens the database to some extent. The excitation curve is well described by the present STAPRE calculation in the energy range between 5 and 16 MeV, while some discrepancies remain below 5 and above 16 MeV. Also in case of the ^{99}Tc(n,p)^{99}Mo and ^{99}Tc(n,α)^{96}Nb reaction this measurement allows for the first time to establish an excitation function from threshold to 20.5 MeV. Good agreement is observed with model calculations.

The present measurements for lead add substantially to an otherwise poor database. The results on the $^{\mathrm{nat}}\mathrm{Pb}(\mathrm{n,x})^{204}\mathrm{Tl}$ and $^{204}\mathrm{Pb}(\mathrm{n,3n})^{202\mathrm{m}}\mathrm{Pb}$ reactions are unique, since no data exist so far. The first one was only possible to measure via Liquid Scintillation Counting (LSC) after chemical separation of the pure β^--emitter $^{204}\mathrm{Tl}$ from the irradiated Pb sample. A coprecipitation method was used together with UV spectroscopy to check the chemical yield of the separation. No agreement was obtaind with the STAPRE calculation, which gives far too high cross sections. For the other reactions studied, a good description was obtained with the nuclear model calculation, using OMP from both Bersillon-Cindro and Koning.

As a result of this thesis work an extended database for neutron induced cross sections on four elements was obtained. It was possible to establish first excitation functions for reactions on a radioactive target nucleus, one very long-lived product and one purely β^- emitting product. It was found that existing evaluations are not always reliable in the prediction of unknown cross sections. Although the experimental results of this work helped to considerably improve the calculations, some deficiencies still exist in case of complex particle emission (like d,t,α) and second chance emission (n,np) or (n,pn) etc. More experimental and theoretical work is thus still needed.

Chapter 7

Zusammenfassung

Eine gute Kenntnis von neutroneninduzierten Wirkungsquerschnitten ist sowohl zum Testen von Kernmodellen als auch für viele praktische Anwendungen erforderlich, besonders im Bereich der Kernenergie. Wirkungsquerschnitte werden beispielsweise benötigt, um Zerfallswärme, Aktivierung von Strukturmaterialien, Gasproduktion usw. sowohl in heutigen Spalt- als auch in zukünftigen Fusionsreaktoren abzuschätzen. Ein weiteres Anwendungsgebiet ist die Transmutation von langlebigen Abfällen in Verbindung mit beschleunigergestützten Systemen (Accelerator Driven Systems, ADS).

In dieser Arbeit wurden Anregungsfunktionen für neutroneninduzierte Reaktionen an Isotopen des V, Mo, Tc und Pb mittels der Aktivierungstechnik studiert. Insgesamt wurden 27 Reaktionen im Energiebereich von 0,5 bis 20,6 MeV gemessen. Diese beinhalteten (n,p), (n,np), (n,α), (n,nα), (n,n'γ), (n,2n) und (n,3n) Reaktionen an obigen Elementen. Die radioaktiven Reaktionsprodukte mit Halbwertzeiten zwischen 58 Sekunden und 20300 Jahren wurden offline mittels hochauflösender γ-Spektrometrie und Flüssigszintillationszählung bestimmt, letztere in Kombination mit radiochemischen Trennverfahren. Die ^{94}Nb-Aktivität wurde im Untergrundlabor HADES mittels "ultra low-level" γ-Spektrometrie gemessen.

Abhängig von der gewünschten Neutronenenergie wurden drei verschiedene neutronenproduzierende Reaktionen und Bestrahlungseinrichtungen verwendet. Bestrahlungen mit Neutronenenergien im Bereich von 0,5 bis 6 MeV wurden unter Verwendung der ^{3}H(p,n)^{3}He Reaktion und eines Ti/T Festkörpertargets durchgeführt, während Energien zwischen 7,4 und 12,5 MeV mit der ^{2}H(d,n)^{3}He Reaktion an einem D_2 Gastarget abgedeckt wurden. Bestrahlungen im Energiebereich von 13,4 bis 20,6 MeV wurden unter Verwendung der ^{3}H(d,n)^{4}He Reaktion wieder mit einem Ti/T Festkörpertarget durchgeführt. Die meisten Reaktionen wurden unter Benutzung eines speziell entworfenen, leichten Probenhalters untersucht, der aus einem Aluminiumring bestand, unter dem die Proben mit kleinen Aluminiumstangen befestigt wurden. Dieses System gestattete die gleichzeitige Bestrahlung mehrerer Proben unter verschiedenen Winkeln und somit unter verschiedenen Neutronenenergien. Außerdem wurde ein pneumatisches Probentransportsystem verwendet, um Reaktionen zu messen, die zu Produkten mit Halbwertzeiten zwischen 1 und 10 Minuten führen. Als drittes wurde ein spezieller Probenhalter zur Messung der ^{nat}Mo(n,x)^{94}Nb-Reaktion entwickelt. Die lange Halbwertzeit von 20300 Jahren erforderte einen Probenhalter, der für maximale Probenmasse, annehmbare Selbstabsorption bei der

γ-Spektrometrie und effiziente Ausnutzung der Strahlzeit optimiert war.

Da der absolute Neutronenfluß nicht gemessen wurde, wurden alle Wirkungsquerschnitte relativ zum ^{27}Al(n,α)^{24}NaStandard-Wirkungsquerschnitt bestimmt. Die Korrekturen, die auf die Daten angewandt wurden, wurden entweder durch den Bestrahlungsprozeß oder durch die Messung der induzierten Aktivität notwendig. Korrekturen für Untergrundneutronen, Breakupneutronen, Schwankungen des Flusses während der Bestrahlung und Mehrfachstreuung gehören zur ersten Gruppe, während Korrekturen für Koinzidenzen, Selbstabsorption und Probengeometrie zur zweiten Gruppe gehören.

Kernmodellrechnungen wurden für alle untersuchten Reaktionen durchgeführt. Für Reaktionen an ^{99}Tc und Pb wurde der original STAPRE Code verwendet, während für Reaktionen an V und Mo eine modifizierte Version STAPRE-H benutzt wurde.

Ein Vergleich von auf EAF-97 basierenden Berechnungen mit Bestrahlungen von V Legierungen zeigte große Diskrepanzen in den Produktionsdaten für ^{47}Sc, wodurch neue Messungen an Vanadium notwendig wurden. Der $^{\mathrm{nat}}$V(n,xα)^{47}Sc-Wirkungsquerschnitt, der aus Beträgen der ^{51}V(n,n'α)^{47}Sc- und ^{50}V(n,α)^{47}Sc-Prozesse besteht, wurde von 11,7 bis 20,5 MeV gemessen. Die Ergebnisse zeigen, daß oberhalb 15 MeV die ^{51}V(n,n'α)^{47}Sc-Reaktion am meisten beiträgt, während für niedrigere Energien die ^{50}V(n,α)^{47}ScReaktion dominiert, wobei ^{50}V eine natürliche Isotopenhäufigkeit von 0,25% besitzt. Die Messungen zeigen eine gute Übereinstimmung mit den STAPRE-H Berechnungen. Zusätzlich wurde die ^{51}V(n,α)^{48}Sc-Reaktion untersucht, für die bisher nur ein einziger Datensatz oberhalb 18 MeV vorlag. Die ^{51}V(n,p)^{51}Ti-Reaktion wurde für zwei ausgewählte Energien gemessen, um eine Lücke in der Anregungsfunktion zu füllen.

Insgesamt wurden 16 neutroneninduzierte Reaktionen am Strukturmaterial Mo studiert. Die größte Herausforderung unter diesen stellte die Produktion von ^{94}Nb dar. Es wird gebildet durch die ^{94}Mo(n,p)- und die ^{95}Mo(n,np)-Reaktion. Eine ca. 1,5 kg schwere Mo Probe wurde in einem speziell entwickelten Probenhalter für 100 h bestrahlt, resultierend in drei Datenpunkten. Zwei der Proben wurden im Untergrundlabor HADES gemessen, während die dritte chemisch aufgearbeitet und anschließend mittels Standard γ-Spektrometrie vermessen wurde. Es war zum ersten Mal möglich, eine Anregungsfunktion für den $^{\mathrm{nat}}$Mo(n,x)^{94}Nb Prozeß zu konstruieren, die in guter Übereinstimmung mit den zwei bereits existierenden Messungen bei 14 MeV ist. Die Verwendung von angereicherten Proben erlaubte die Unterscheidung zwischen (n,p)- und (n,np+pn+d)-Beiträgen zur gleichen Aktivität. Die Messungen der ^{94}Mo(n,2n)$^{93\mathrm{m}}$Mo- und ^{100}Mo(n,2n)^{99}Mo-Reaktionen profitierten ebenfalls von der Verwendung angereicherter Proben, da Aktivitätsbeiträge des (n,γ) Prozesses unterdrückt wurden. Alle untersuchten Reaktionen konnten zur EAF-99 Bibliothek verglichen werden, während dies im Falle von JENDL-3.2 nur für Reaktionen möglich war, die nicht zu isomeren Endzuständen führen. Ein Vergleich mit den Modellrechnungen zeigt eine recht gute Übereinstimmung der berechneten Werte mit den experimentellen Daten, außer für die ^{97}Mo(n,np)^{96}Nb- und ^{98}Mo(n,np)$^{97\mathrm{m+g}}$Nb-Reaktionen und, zu geringerem Ausmaße, der ^{100}Mo(n,α)^{97}Zr-Reaktion. In der Mehrheit der Fälle stimmen die Modellrechnungen besser mit den experimentellen Daten überein, als die EAF-99 Evaluation. Soweit vorhanden, gibt JEND-3.2 eine ähnlich gute Übereinstimmung, außer im Falle der ^{97}Mo(n,np)^{96}Nb-Reaktion, wo sie besser ist, und im Falle der ^{100}Mo(n,α)^{97}Zr-Reaktion, wo sie etwas schlechter ist.

Drei neutroneninduzierte Reaktionen am radioaktiven Spaltprodukt ^{99}Tc sind von der Schwelle bis 20.6 MeV gemessen worden. Diese Reaktionen sind ^{99}Tc(n,n'γ)^{99m}Tc, ^{99}Tc(n,p)^{99}Mo und ^{99}Tc(n,α)^{96}Nb. Für all diese Reaktionen konnten nur vier Datensätze in der Literatur gefunden werden, alle gemessen um 14 MeV. Die induzierte Radioaktivität wurde via γ-Spektrometrie gemessen, wobei ein Bleiabsorber zwischen Probe und Detektor verwendet wurde, um die Bremsstrahlung zu unterdrücken. Bisher wurden nur für wenige Nuklide komplette Anregungsfunktionen des (n,n'γ) Prozesses bestimmt. Die Messung erweitert also die Datenbank zu einem gewissen Maße. Die STAPRE Berechnung reproduziert die Anregungsfunktion gut im Energiebereich zwischen 5 und 16 MeV, allerdings bleiben gewisse Abweichungen unterhalb 5 MeV und oberhalb 16 MeV. Auch im Falle der ^{99}Tc(n,p)^{99}Mo- und ^{99}Tc(n,α)^{96}Nb- Reaktionen erlaubt diese Messung zum ersten Mal, eine Anregungsfunktion von der Schwelle bis 20,5 MeV aufzustellen. Die Modellrechnungen stimmen gut mit den experimentellen Daten überein.

Die hier präsentierten Messungen an Blei tragen wesentlich zu einer bislang unvollständigen Datenbank bei. Die Ergebnisse für die ^{nat}Pb(n,x)^{204}Tl- und ^{204}Pb(n,3n)^{202m}Pb-Reaktionen sind einmalig, da bis jetzt noch keine Daten existierten. Die Messung der ersten Reaktion war nur möglich mittels Flüssigszintillationszählung mit einer vorhergehenden chemischen Abtrennung des reinen β^--Emitters ^{204}Tl von der bestrahlten Bleiprobe. Eine Mitfällungsmethode wurde verwendet in Kombination mit UV-Spektrometrie zur Kontrolle der chemischen Ausbeute. Keine Übereinstimmung konnte mit der STAPRE-Berechnung erzielt werden, die wesentlich zu hohe Wirkungsquerschnitte ergab. Für die anderen untersuchten Reaktionen konnte ein gute Beschreibung erhalten werden, sowohl mit dem OMP von Bersillon-Cindro als auch dem von Koning.

Als Ergebnis dieser Arbeit wurde eine ausführliche Datenbank für neutroneninduzierte Wirkungsquerschnitte an vier Elementen erhalten. Es war möglich, die ersten Anregungsfunktionen für Reaktionen an einem radioaktiven Targetkern, für ein sehr langlebiges Reaktionprodukt und für ein nur β^--emittierendes Produkt aufzustellen. Es stellte sich heraus, daß existierende Evaluationen nicht immer verläßlich in der Lage sind, unbekannte Wirkungsquerschnitte vorherzusagen. Obwohl die experimentellen Ergebnisse dieser Arbeit erheblich dazu beigetragen haben, die Kernmodellrechnungen zu verbessern, existieren immer noch Abweichungen im Falle von Emissionen komplexer Teilchen (wie d, t, α) und “second chance” Emission (n,np) oder (n,pn) usw. Folglich sind noch mehr experimentelle und theoretische Arbeiten notwendig.

References

[1] H. Becquerel, Émission de radiation nouvelles par l'uranium métallique, C. R. Acad. Sci. **122**, 1086–1088 (1896).

[2] E. Rutherford, Collision of alpha particles with light atoms. IV. An anomalous effect in nitrogen, The London, Edinburgh and Dublin Philosophical Magazine and Journal of Science **37**, 581 (1919).

[3] J. Chadwick, Possible existence of a neutron, Nature **129**, 312 (1932).

[4] J. Chadwick, The existence of a neutron, Proc. Roy. Soc., A **A136**, 692–708 (1932).

[5] M. Salvatores, I. Slessarev, and A. Tchistiakov, The transmutation of long-lived fission products by neutron irradiation, Nucl. Sci. Eng. **130**, 309–319 (1998).

[6] M. Salvatores, A. Zaetta, C. Girard, M. Delpech, I. Slessarev, and J. Tomassi, Nuclear waste transmutation, Appl. Radiat. Isot. **46**(6), 681–687 (1995).

[7] C. Rubbia, J. A. Rubio, S. Buono, F. Carmine, N. Fieter, J. Galvez, C. Geles, Y. Kadi, R. Klapisch, P. Mandrillon, J. P. Revol, and C. Roche, Conceptual design of a fast neutron operated high power energy amplifier, Report CERN/AT/95-44(ET), 1995, available online at `http://cern.web.cern.ch/CERN/Divisions/SL/EET/Energy_Amplifier/PDF/95-4%4.pdf`.

[8] Working Party on International Evaluation Co-operation, *The NEA high priority nuclear data request list*, NEA Nuclear Science Commitee, 1998, available at `http://www.nea.fr/html/science/docs/pubs/hprl.pdf`.

[9] O. Hahn, Chem. Berichte **54**, 1131 (1921).

[10] C. F. von Weizsäcker, Metastabile Zustände der Atomkerne, Naturwissenschaften **24**, 813 (1936).

[11] Qtool: Calculation of reaction Q-values and thresholds, T-2 Nuclear Information Service, Los Alamos National Laboratory, USA, March 1997, available online at `http://t2.lanl.gov/data/qtool.html`.

[12] G. Audi and A. H. Wapstra, The 1995 update to the atomic mass evaluation, Nucl. Phys. A **595**, 409 (1995).

[13] E. Gadioli and P. E. Hodgson, *Pre-equilibrium nuclear reactions*, Clarendon Press, Oxford, 1992.

[14] N. Bohr, Neutron capture and nuclear constitution, Nature **137**, 344–348 (1936).

[15] S. M. Qaim, Radiochemical studies of complex particle emission in low and intermediate energy reactions, Radiochim. Acta **70/71**, 163–175 (1995).

[16] S. M. Qaim, C. H. Wu, and R. Wölfle, ^{3}He particle emission in fast neutron induced reactions, Nucl. Phys. A **410**, 421 (1983).

[17] J. Csikai, *Handbook of Fast Neutron Generators*, CRC Press, Inc., Boca Raton, Florida, USA, 1987.

[18] S. Cabral, G. Börker, H. Klein, and W. Mannhart, Neutron production from the deuteron breakup reaction on deuterium, Nucl. Sci. Eng. **106**, 308–317 (1990).

[19] A. Grallert, J. Csikai, and S. M. Qaim, Improved gas-cell D-D neutron sources, Nucl. Instrum. Methods Phys. Res. **A337**, 615–618 (1994).

[20] Nuclear data standards for nuclear measurements, NEANDC-311 "U", edited by H. Condé, NEA Nuclear Data Committee, Paris, 1992.

[21] C. M. Bartle and P. A. Quin, The production of a 2–10 MeV collimated neutron beam of known flux using the associated particle technique, Nucl. Instrum. Methods Phys. Res. **121**, 119–127 (1974).

[22] H. Liskien and A. Paulsen, Determination of 1 MeV neutron fluxes from the T(p,n)^{3}He reaction by the associated particle method, Nucl. Instrum. Methods Phys. Res. **69**, 70–76 (1969).

[23] A. Paulsen, R. Widera, A. Berlin, and A. Trapani, Neutron flux measurements by counting the associated ^{3}He particles from the T(p,n) reaction corresponding to 500 keV neutron energy, Nucl. Instrum. Methods Phys. Res. **91**, 581–593 (1971).

[24] G. Winkler, Prerequisites for accurate activation cross section measurements, in *Proceedings of the International Conference on Nuclear Data for Science and Technology*, edited by S. M. Qaim, pages 401–405, Jülich, Germany, 13–17 May 1991, Springer Verlag, Heidelberg.

[25] G. Winkler, V. E. Lewis, T. B. Ryves, and M. Wagner, The ^{238}U(n,f) cross section and its ratio to the ^{27}Al(n,α)^{24}Na and ^{56}Fe(n,p)^{56}Mn cross section in the 14 MeV region, in *Proceedings of the International Conference on Nuclear Data for Science and Technology*, edited by S. M. Qaim, pages 514–517, Jülich, Germany, 13–17 May 1991, Springer Verlag, Heidelberg.

[26] M. Wagner, G. Winkler, H. Vonach, and G. Peto, Measurement of the Cross Section for the Reaction ^{93}Nb(n,n')$^{93\mathrm{m}}$Nb at 2.8 MeV, Ann. Nucl. Energy **15**, 363 (1988).

[27] J.-C. Sublet, J. Kopecky, and R. Forrest, The european activation file: EAF-99 cross section library, UKAEA Report FUS 408, 1998.

[28] T. Nakagawa, K. Shibata, S. Chiba, T. Fukahori, Y. Nakajima, Y. Kikuchi, T. Kawano, Y. Kanda, T. Ohsawa, H. Matsunobu, M. Kawai, A. Zukeran, T. Watanabe, S. Igarasi, K. Kosako, and T. Asami, Japanese evaluated nuclear data library version 3, revision 2: JENDL-3.2, J. of Nucl. Sci. and Technol. **32**, 1259 (1995).

[29] C. Nordberg and M. Salvatores, Status of the JEF evaluated data library, in *Proceedings of the International Conference on Nuclear Data for Science and Techology*, edited by J. K. Dickens, pages 680–684, Gatlinburg, USA, 9–13 May 1984, online available at `http://t2.lanl.gov/data/ndviewer.html`.

[30] Evaluated nuclear data file, section B, version VI (ENDF/B-VI), National Nuclear Data Center, Brookhaven National Laboratory, 1998, available online at `http://www.nndc.bnl.gov/nndc/endf`.

[31] M. Bormann, S. Cierjacks, R. Langkau, H. Neuert, and H. Pollehn, Mesure de quelques sections efficaces (n,α) dans l'intervalle des énergies des neutrons 12 a 19.6 MeV, J. Phys. Rad. **22**, 602–604 (1961).

[32] M. Bormann, S. Cierjacks, R. Langkau, and H. Neuert, Über die Wirkungsquerschnitte einiger n,nα Reaktionen für Neutronenenergien zwischen 12 und 19 MeV, Z. Phys. **166**, 477–493 (1962).

[33] S. M. Qaim, A study of (n,nα) reaction cross sections at 14.7 MeV, Nucl. Phys. **A458**, 237–246 (1986).

[34] C. H. Wu, R. Wölfle, and S. M. Qaim, Activation and mass spectrometric study of ^{3}He particle emission in the interaction of fast neutrons with medium mass nuclei, Nucl. Phys. A **329**, 63–72 (1979).

[35] R. Pepelnik, B. Anders, and B. M. Bahal, Measurements of 14 MeV neutron activation cross sections, in *Proceedings of the International Conference on Nuclear Data for Basic and Applied Science*, edited by P. Young, R. Brown, G. Auchampaugh, P. Lisowski, and L. Stewart, pages 211–214, Santa Fe, New Mexico, USA, May 13-17 1985, Gordon and Breach Science Publishers, also published in [157].

[36] D. Richter, R. A. Forrest, H. Freiesleben, V. D. Kovalchuk, V. D. Kovalchuk, D. V. Markovskij, K. Seidel, V. I. Tereshkin, and S. Unholzer, Measurement and analysis of radioactivity induced in low-activation steels by 14-MeV neutrons, in *Proceedings of the 9th Conference on Fusion Nuclear Materials, ICFRM-9*, Colorado Springs, USA, 10-15 October 1999.

[37] U. von Möllendorf, H. Giese, and H. Tsige-Tamirat, Activation test of vanadium alloys with a deuterium-beryllium neutron source, EFFDOC-647, OECD Nuclear Energy Agency, 92130 Issy-les-Moulineaux, France, 1998.

[38] K. Seidel, R. A. Forrest, H. Freiesleben, V. D. Kovalchuk, D. V. Markovskij, D. Richter, V. I. Tereshkin, and S. Unholzer, Measurement and analysis of radioactivity induced in vanadium alloys by 14-MeV Neutrons, EFFDOC-683, OECD Nuclear Energy Agency, 92130 Issy-les-Moulineaux, France, 1999.

[39] M. Pillon, Irradiation of advanced vanadium alloy, V-4Cr-4Ti, EFFDOC-661, OECD Nuclear Energy Agency, 92130 Issy-les-Moulineaux, France, 1998.

[40] L. R. Greenwood, D. G. Doran, and H. L. Heinisch, Production of ^{91}Nb, ^{94}Nb, and ^{95}Nb from Mo by 14.5–14.8 MeV neutrons, Phys. Rev. C **35**(1), 76 (1987).

[41] Y. Ikeda and C. Konno, Measurements of the cross sections for ^{94}Mo(n,p) & ^{95}Mo(n,np)^{94}Nb, ^{158}Dy(n,p)^{158}Tb, ^{182}W(n,nα)^{178m2}Hf and ^{187}Re(n,2n)^{186m}Mo reactions at 14 MeV region, INDC(NDS)-286, 27-31, 1993.

[42] H. Liskien, R. Wölfle, R. Widera, and S. M. Qaim, Excitation functions of (n,p) and (n,α) reactions on molbydenum isotopes, Appl. Radiat. Isot. **41**(1), 83–90 (1990).

[43] N. W. Golchert, Cross section of some reactions of ^{99}Tc with 14.1 MeV neutrons, Nucl. Phys. **73**, 349–352 (1965).

[44] S. M. Qaim, Nuclear reaction cross-sections for 14.7 MeV neutrons on ^{99}Tc, J. Inorg. Nucl. Chem. **35**, 3669–3675 (1973).

[45] G. Goldstein, Activation cross sections for the reaction of 14·8-MeV neutrons with ^{99}Tc, J. Inorg. Nucl. Chem. **28**, 676–678 (1966).

[46] Y. Ikeda, E. T. Cheng, C. Konno, and H. Maekawa, Measurement of neutron activation cross sections for ^{99}Tc(n,p)^{99}Mo, ^{99}Tc(n,α)^{96}Nb, ^{99}Tc(n,n'α)^{95}Nb, and ^{99}Tc(n,n'γ)^{99m}Tc, Nucl. Sci. Eng. **116**, 28–34 (1994).

[47] J. Op de Beeck, A. Speecke, and J. Hoste, The ^{204}Pb(n,p)^{204}Tl reactor cross-section and the neutron activation analysis of thallium in lead, Radiochim. Acta **4**, 32–35 (1965).

[48] P. Welch, J. Johnson, G. Randers-Pehrson, and J. Rapaport, Neutron activation cross section on ^{12}C and Pb with 20-26 MeV monoenergetic neutrons, Bull. Am. Phys. Soc. **26**, 708 (1981).

[49] F. J. Vaughn, data taken from EXFOR, see [158], 1963.

[50] P. Decowski, W. Grochulski, A. Marcinkowski, J. Karolyi, J. Piotrowski, E. Saad, K. Siwek-Wilczynska, I. M. Turkiewicz, and Z. Wilhelmi, Cross sections for the (n,n') and (n,2n) Reactions on ^{113}In and ^{204}Pb, Nucl. Phys. A **204**, 121 (1973).

[51] K. J. R. Rosman and P. D. P. Taylor, Isotopic composition of the elements 1997, Pure & Appl. Chem. **70**, 217–235 (1998).

[52] R. D. Russell and R. M. Farquar, *Lead isotopes in geology*, Interscience Publisher INC., New York, 1960.

[53] S. M. Qaim, R. Wölfle, M. M. Rahman, and H. Ollig, Measurement of (n,p) and (n,α) reaction cross sections on some isotopes of nickel in the energy region of 5 to 10 MeV using a deuterium gas target at a compact cyclotron, Nucl. Sci. Eng. **88**, 143–153 (1984).

[54] Z. Kormány, A new method and apparatus for measuring the mean energy of cyclotron beams, Nucl. Instrum. Methods Phys. Res. **A337**, 258–264 (1994).

[55] I.-G. Birn and S. M. Qaim, Excitation functions of neutron threshold reactions on some isotopes of germanium, arsenic, and selenium in the 6.3- to 14.7-MeV energy range, Nucl. Sci. Eng. **116**, 125–137 (1994).

[56] A. Pavlik, G. Winkler, H. Vonach, A. Paulsen, and H. Liskien, Precise measurement of cross sections for the ^{90}Zr(n,2n)^{89}Zr reaction from threshold to 20 MeV, J. Phys. (London) **G8**, 1283–1299 (1982).

[57] A. Fessler, A. J. M. Plompen, D. L. Smith, J. W. Meadows, and Y. Ikeda, Neutron activation cross-section measurements from 16 to 20 MeV for isotopes of F, Na, Mg, Al, Si, P, Cl, Ti, V, Mn, Fe, Nb, Sn, and Ba, Nucl. Sci. Eng. **134**, 171–200 (2000).

[58] H. Liskien and A. Paulsen, Neutron production cross sections and energies for the reactions T(p,n)^{3}He, D(d,n)^{3}He, and T(d,n)^{4}He, Nucl. Data Tables **11**, 569–619 (1973).

[59] I.-G. Birn, NEUT–Ein Programm zur Berechnung von Neutronenspektren erzeugt durch die D(d,n)^{3}He-Reaktion in einem Gastarget am Zyklotron, KFA-Jülich, Internal Report No. INC-IB-1/92, 1992.

[60] I.-G. Birn, Calculation of the mean energy and the energy spread of neutrons produced by the D(d,n)^{3}He reaction in a gas target, CEC-JRC, IRMM, Geel, internal Report No. GE/R/VG/85/94, 1994.

[61] A. B. Smith, S. Chiba, D. L. Smith, J. W. Meadows, P. T. Guenther, R. D. Lawson, and R. J. Howerton, Evaluated neutronic file for indium, Argonne National Laboratory, Report No. ANL/NDM-115, 1990.

[62] M. Wagner, H. Vonach, A. Pavlik, B. Strohmaier, S. Tagesen, and J. Martinez-Rico, Evaluation of cross sections of 14 important neutron-dosimetry reactions, Physics Data **13-5**, 34 (1990), in [20].

[63] H. Klein, H. J. Brede, and B. R. L. Siebert, Energy and angle straggling effects in a D(d,n)^{3}He neutron source using a gas target, Nucl. Instrum. Methods Phys. Res. **193**, 635–644 (1982).

[64] H. H. Anderson and J. F. Ziegler, *Hydrogen stopping powers and ranges in all elements*, Pergamon Press, NewYork, 1977.

[65] J. F. Briesmeister, MCNP$^{\text{TM}}$–A general Monte Carlo n-particle transport code, report LA-13709, Los Alamos National Laboratory, April 2000, available online at `http://www-xdiv.lanl.gov/XCI/PROJECTS/MCNP/themanual.html`.

[66] D. L. Smith, A least-squares computational “Tool Kit”, Argonne National Laboratory, Report No. ANL/NDM-128, 1993.

[67] C. L. Dunford and R. R. Kinsey, NuDat system for access to nuclear data, IAEA-NDC-205 (BNL-NCS-65687), IAEA, Vienna, Austria, July 1998, Information extracted from the NuDat data base, version of 7-Sep-2000, using the PC version of the program NuDat.

[68] M. Wagner, , Report INDC(AUS)-D14, Vienna, 1991, in [20].

[69] W. Westmeier and J. VanAarle, PC-based high precision nuclear spectrometry, Nucl. Instrum. Methods Phys. Res. **A286**, 439 (1990).

[70] B. Jäckel, W. Westmeier, and P. Patzelt, On the photopeak efficiency of Germanium gamma-ray detectors, Nucl. Instrum. Methods Phys. Res. **A261**, 543–548 (1987).

[71] K. Debertin and R. G. Helmer, editors, *Gamma- and x-Ray spectrometry with semiconductor detectors*, Elsevier Science Publishers B. V., North Holland, Amsterdam, 1988.

[72] M. J. Berger, J. H. Hubbel, S. M. Seltzer, J. S. Coursey, and D. S. Smith, *XCOM: photon cross section database (version 1.2)*, National Institute of Standards and Technology, Gaithersburg, MD, 1999, available at `http://physics.nist.gov/PhysRefData/Xcom/Text/XCOM.html`.

[73] K. Debertin and U. Schötzig, Bedeutung von Summationskorrekturen bei der Gammastrahlen-Spektrometrie mit Germaniumdetektoren, Physikalisch Technische Bundesanstalt, PTB-Bericht, PTB-Ra-24, 1990.

[74] R. B. Firestone, *Table of Isotopes*, Wiley, New York, 8^{th} edition, 1996, also available on CD.

[75] M. Hult, M. J. Martínez Canet, M. Köhler, J. das Neves, and P. N. Johnston, Recent developments in ultra low-level γ-ray spectroscopy at IRMM, Appl. Radiat. Isot. **53**, 225 (2000).

[76] L. Johansson, G. Sibbens, T. Altzitzoglou, and B. Denecke, Self-absorbtion correction in standardisation of ^{204}Tl, Appl. Radiat. Isot. , to be published (2001).

[77] A. Grau Malonda and E. Garcia Toraño, Evaluation of counting efficiency in liquid scintillation counting of pure β-ray emitters, Int. J. Appl. Radiat. Isot. **33**, 249 (1982).

[78] A. Grau Malonda, E. Garcia Toraño, and J. M. Los Arcos, Liquid Scintillation Counting efficiency as function of the figure of merit for pure β-ray emitters, Int. J. Appl. Radiat. Isot. **36**, 157 (1982).

[79] C. L. Luke, Photometric determination of antimony and thallium in lead, Anal. Chem. **31**(10), 1680–1682 (1959).

[80] C. L. Luke and M. E. Campbell, Determination of impurities in germanium and silicon, Anal. Chem. **25**(11), 1588–1593 (1953).

[81] R. E. Van Aman and J. H. Kanzelmeyer, Spectrophotometric determination of thallium in zinc and cadmium with rhodamine B, Anal. Chem. **33**(8), 1128–1129 (1961).

[82] S. M. Qaim, H. V. Klapdor, and H. Reiss, Statistical model analysis of cross sections of (n,t) and (n,^{3}He) reactions induced by 14.6 MeV neutrons on target nuclei with A=27–59, Phys. Rev. C **22**, 1371 (1980).

[83] P. G. Young and E. D. Arthur, GNASH: Preequilibrium statistical nuclear model code for calculations of cross sections and emission spectra, Report No. LA-6947, Los Alamos Scientific Laboratory, 1977.

[84] M. Herman and A. Marcinkowski, Measurements of (n,2n) cross sections on ^{90}Zr, ^{94}Mo and ^{197}Au at 14.7 MeV, data taken from EXFOR, see [158], 1984.

[85] M. Uhl and B. Strohmaier, Computer code for particle induced activation cross section and related quantities, IRK Report 76/01, Vienna, 1976.

[86] M. Avrigeanu, M. Ivascu, and V. Avrigeanu, A computer code for particle induced activation cross section and related quantities, IPNE Report NP-63-1997, 1987.

[87] M. Avrigeanu and V. Avrigeanu, Recent improvements of the STAPRE-H95 preequilibrium and statistical model code, IPNE Report NP-86-1995, 1995.

[88] O. Bersillon, SCAT2: Un programme de modèle optique sphérique, Note CEA-N-2227, CEN-Bruyeres-le-Chatel, 1981.

[89] A. Grallert, J. Csikai, C. M. Buczko, and I. Shaddad, Investigations on the systematics in (n,α) cross sections at 14.6 MeV, Technical Report 286, INDC(NDS), 1993.

[90] Y. Wang, J. Yang, J. Yuan, and X. Kong, Cross section measurements for (n,d*) (n,t) and (n,n'α) reactions, High Energy Physics and Nuclear Physics **17**(4), 289–293 (1993).

[91] A. D. Majdeddin, V. Semkova, R. Dóczi, C. M. Buczkó, and J. Csikai, Investigations on (n,α) cross sections in the 14 MeV region, IAEA Report INDC(HUN)-031, Vienna, 1993.

[92] A. Paulsen, R. Widera, and H. Liskien, Cross-sections for the reactions ^{51}V(n,α)^{48}Sc between 10 and 20 MeV, Atomkernenergie **22**(4), 291–291 (1974).

[93] D. L. Smith, J. W. Meadows, and I. Kanno, Measured activation cross sections below 10 MeV for the ^{51}V(n,p)^{51}Ti and ^{51}V(n,a)^{48}Sc reactions, Ann. Nucl. Energy **11**, 623 (1984).

[94] J. W. Meadows, D. L. Smith, M. M. Bretscher, and S. A. Cox, Measurement of 14.7 MeV neutron-activation cross sections for fusion, Ann. Nucl. Energy **14**, 489 (1987).

[95] Y. Ikeda, C. Konno, K. Oishi, T. Nakamura, H. Miyade, K. Kawade, H. Yamamoto, and T. Katoh, Activation cross section measurements for fusion reactor structural materials at energies from 13.3 to 15.0 MeV using FNS facility, JAERI-1312, 1988.

[96] S. M. Qaim and N. I. Molla, Nuclear data measurements for FR-wall and structural materials, in *Proceedings of the 9^{th} Symposium on Fusion Technology*, pages 589–595, Garmisch-Partenkirchen, 14-18 June 1976.

[97] H.-L. Lu, D.-H. Wang, Y.-J. Xiu, Y.-F. Cui, and P.-L. Chen, IAEA Report INDC(CPR)-16, Vienna, 1989.

[98] R. Dóczi, S. Sudár, J. Csikai, and S. M. Qaim, Excitation functions of the ^{89}Y(n,n'γ)^{89}Y^m and ^{89}Y(n,$\alpha\gamma$)^{86}Rb^m prozesses, Phys. Rev. C **58**(4), 2577–2580 (1998).

[99] A. A. Filatenkov, S. V. Chuvaev, V. N. Aksenov, V. A. Yakovlev, A. V. Malyshenkov, S. K. Vasil'ev, M. Avrigeanu, V. Avrigeanu, D. L. Smith, Y. Ikeda, A. Wallner, W. Kutschera, A. Priller, P. Steiner, H. Vonach, G. Mertens, and W. Rochow, Systematic Measurement of Activation Cross Sections at Neutron Energies from 13.4 to 14.9 MeV, Report RI-252, 1999.

[100] W. Mannhart, D. Schmidt, and D. L. Smith, Measurement of the ^{52}Cr(n,p)^{52}V, ^{52}Cr(n,2n)^{51}Cr, ^{51}V(n,p)^{51}Ti and ^{51}V(n,α)^{48}Sc cross setions between 7.9 and 14.4 MeV, in *Proceedings of the International Conference on Nuclear Data for Science and Technology*, edited by A. V. G. Reffo and C. Grandi, pages 505–507, Trieste, Italy, May 19-24 1997, Editrice Compositori, 40128 Bologna, Italy.

[101] T. Katoh, K. Kawade, and H. Yamamoto, Report JAERI-M-89-026, 293, 1989.

[102] I. Garlea, C. Miron-Garlea, H. N. Rosu, G. Fodor, and V. Raducu, Integral neutron cross sections measured around 14 MeV, Rev. Roum. Phys **37**, 19 (1992).

[103] K. T. Osman and F. I. Habbani, Measurement and study of (n,p) reaction cross sections for Cr, Ti, Ni, Co, Zr, and Mo isotopes using 14.7 MeV neutrons, Report INDC(SUD)-001, 1996.

[104] X. Kong, Y. Wang, J. Yang, and J. Yuan, Recent progress on 14 MeV neutron activation cross section measurements, report INDC(CPR)-036/L, 1995.

[105] N. I. Molla, R. U. Miah, S. Basunia, S. M. Hossain, and M. Rahman, Excitation functions of (n,p), (n,α) and (n,2n) processes on some isotopes of Cl, Cr, Ge, Mo, and Ce in the energy range 13.57 MeV–14.71 MeV, International Conference on Nuclear Data and Technology, edited by G. Reffo, A. Ventura and C. Grandi, Trieste, 19-24 May, 1997.

[106] O. I. Artemév, I. V. Kazachevskii, V. N. Levkovskii, V. L. Poznyak, and V. F. Reutov, Cross sections for (n,p) and (n,α) reactions on chromium, iron, copper, and molybdenum nuclei at a neutron energy of 14.8 MeV, At. Energ. **49**(3), 195 (1980).

[107] W. D. Lu, N. Ranakamur, and R. W. Fink, Activation cross sections for (n,2n) ractions at 14.4 MeV in the region Z=40-60. precision measurements and systematics, Phys. Rev. C **1**, 350 (1970).

[108] R. A. Sigg and P. K. Kuroda, 14.8 MeV neutron-induced (n,2n), (n,p), and (n,α) cross-sections for some closed shell nuclides, J. Inorg. Nucl. Chem. **37**, 631 (1975).

[109] E. T. Bramlitt and R. W. Fink, Rare nuclear reactions induced by 14.7-MeV neutrons, Phys. Rev. **131**(6), 2649–2662 (1963).

[110] Y. Kanda, The excitation functions and isomer ratios for neutron-induced reactions on ^{92}Mo and ^{90}Zr, Nucl. Phys. A **185**, 177–195 (1972).

[111] K. Fukuda, K. Matsuo, S. Shirahama, and I. Kumabe, Activation cross sections for Fe, Co, Ni, Zr and Mo, report NEANDC(J)-56/U, 1978.

[112] Y. Fujino, M. Hyakutake, and I. Kumabe, Activation cross sections on zirconium and molybdenum isotopes induced by 14.6 MeV neutrons, NEANDC(J)-51, 1977.

[113] S. Amemiya, K. Ishibashi, and T. Katoh, Neutron activation cross section of molybdenum isotopes at 14.8 MeV, J. of Nucl. Sci. and Technol. **19**(10), 781 (1982).

[114] H. Atsumi, H. Miyade, M. Yoshida, T. Ishii, H. Yamamoto, K. Kawade, T. Katoh, A. Takashida, and T. Iida, Measurement of neutron activation cross-section of fusion reactor materials at 14.6 MeV, Report NEANDC(J)-106/U, 1984.

[115] M. M. Rahman and S. M. Qaim, Excitation functions of some neutron threshold reactions on isotopes of molybdenum, Nucl. Phys. A **435**, 43 (1985).

[116] R. Pepelnik, B. Anders, B. M. Bahal, and M. Farooq, 14 MeV neutron activation cross sections, Report NEANDC(E)-262/U, (5), 1985.

[117] K. Kobayashi and I. Kimura, Application of a 6-LiD thermal 14 MeV neutron converter to the measurement of activation cross sections, in *Proceedings of the International Conference on Nuclear Data for Science and Technology*, edited by S. Igarasi, pages 261–265, Mito, Japan, 30 May – 3 June 1988.

[118] S. M. Qaim and R. Wölfle, First- and second-chance emission in the interaction of fast neutrons with ^{92}Mo, Phys. Rev. C **40**(5), 1993–1997 (1989).

[119] I. Kimura and K. Kobayashi, Calibrated fission and fusion neutron fields at the Kyoto Iniversity Reactor, Nucl. Sci. Eng. **106**, 332 (1990).

[120] F. Strohal, N. Cindro, and B. Eman, Reaction mechanisms and shell effects from the interaction of 14.6 MeV neutrons with nuclei, Nucl. Phys. **30**, 49 (1962).

[121] A. Marcinkowki, K. Stankiewicz, U. Garuska, and M. Herman, Cross section of fast neutron induced reactions on molybdenum isotopes, Z. Phys. A **323**, 91–96 (1986).

[122] N. I. Molla, M. M. Rahman, S. Kathun, A. K. M. F. Hoque, R. Miah, and A. A. Khan, Activation cross sections for some isotopes of Mg, Tl, V, Ni, Zr and Mo at 14 MeV neutrons, Report INDC(BAN)-003, 1986.

[123] C. V. Srinivasa Rao and J. Rama Rao, Neutron nuclear cross section data for fusion technology, in *Proceedings of the International Conference on Nuclear Cross Sections for Technology*, edited by J. L. Fowler, C. H. Johnson, and C. D. Johnson, pages 848–852, Knoxville, USA, 22-26 October 1979.

[124] S. C. Cujrathi and S. K. Mukherkjee, Decay of ^{98}Mo and the energy levels of ^{98}Mo, Nucl. Phys. **85**, 288 (1966).

[125] R. Prasad and D. C. Sarkar, Measured (n,p) reaction cross sections and their predicted values at 14.8 MeV, Nuovo Cimento A **3**, 467 (1971).

[126] P. Cuzzocrea, E. Perillo, and S. Notarrigo, Activation cross sections of Mo isotopes for 14.1 MeV neutrons, Nucl. Phys. A **103**, 616 (1967).

[127] S. M. Qaim, R. Wölfle, and G. Stöcklin, Activation cross sections of fast neutron induced nuclear reactions. Precision measurements and systematics, 71CANT, 1971.

[128] X. Kong, Y. Wang, J. Yang, J. Yuan, and X. Wang, Cross section measurements for Mo-98(n,α)Zr-95, Mo-95(n,p)Nb-95m and Mo-95(n,p)Nb-95g and Ta-181(n,p)Hf-181 reaction, Chin. J. Nucl. Phys. **14**(3), 239 (1992).

[129] S. M. Qaim, R. Wölfle, and G. Stöcklin, Fast neutron induced [(n,t)+(n,n't)] reaction cross-sections in the medium and heavy mass regions, J. Inorg. Nucl. Chem. **36**, 3639–3642 (1974).

[130] K. Yamauchi, Y. Kasugai, H. Yamamoto, T. Iida, A. Takahashi, and K. Kawade, Measurement of formation cross cection producing short-lived nuclei by 14 MeV neutrons – Mg, S, Ga, Y, Mo, Pd, Sn, Report INDC(JPN)-169/L, 1993.

[131] V. Bostan, M. N. Erduran, E. Gültekin, M. M. Subaşi, and M. Şirin, Measurement of formation cross sections for very short lived isotopes at the neutron energies from 13.6 to 14.9 MeV, in *Proceedings of the International Conference on Nuclear Data for Science and Technology*, edited by A. V. G. Reffo and C. Grandi, pages 598–602, Trieste, Italy, May 19-24 1997, Editrice Compositori, 40128 Bologna, Italy.

[132] L. Chaturverdi, C. N. Pandy, and S. K. Bose, Activation cross section for (n,2n), (n,p) and (n,α) reactions at 14 MeV, INDC(SEC)-61, 1977.

[133] V. K. Tikku, H. Singh, and B. Sethi, Nuclear activation cross sections of (n,p) reactions at 14.7 MeV, CHANDG, 2, 1972.

[134] E. B. Paul and R. L. Clarke, Cross-section measurements of reactions induced by neutrons of 14.5 MeV energy, Can. J. Phys. **31**, 267–276 (1953).

[135] S. S. Hasan, R. Prasad, and M. L. Sehgal, The 14.8 MeV neutron cross sections for enriched isotopes of ^{82}Se, ^{92}Mo, ^{117}Sn, ^{128}Te and ^{130}Te.

[136] S. M. Qaim, Activation cross section, isomeric cross-section ratios and systematics of (n,2n) reactions at 14-15 MeV, Nucl. Phys. A **185**, 614 (1972).

[137] B. Minetti and A. Pasquarelli, Isomeric cross-section ratio for (n,2n) reactions induced by 14.7 MeV neutrons, Nucl. Phys. A **118**, 449 (1968).

[138] R. Prasad and D. C. Sarkar, Isomeric cross-section ratios for (n,2n) reactions at 14.8 MeV, Nucl. Phys. A **94**, 476 (1967).

[139] J. Bacso, J. Csikai, and A. Pazsit, Investigation of Mo^{92}(n,2n)$\mathrm{Mo}^{91,91m}$ reaction, Acta Phys. Hung. **18**, 295 (1965).

[140] L. R. Greenwood, Measurement of longlived isotopes and helium production in fusion materials, IAEA-TECDOC-572, 1989.

[141] J. Araminowicz and J. Dresler, Investigation of the (n,2n) Reaction with 14.6 MeV Neutrons, report INR-1494, data taken from EXFOR, see [158], 1972.

[142] C. S. Khurana and H. S. Hans, Cross sections for (n,2n) reactions at 14.8 MeV, Nucl. Phys. **28**, 560 (1961).

[143] Z. Muyao, Z. Yongfa, W. Chuanshan, Z. Lu, C. Yitai, and Z. Shukin, Shell effect from the cross section of the (n,2n) reaction produced by 14.6 MeV neutrons, Chin. J. Nucl. Phys. **9**, 34 (1987).

[144] J. Csikai and G. Peto, Influence of direct inelastic scattering on (n,2n) cross-sections, Acta Phys. Hun. **23**, 87 (1967).

[145] G. N. Maslov, F. Naseov, and N. F. Pashkin, The experimental cross sections of the nuclear reactions for 14 MeV neutrons, report YK-9, data taken from EXFOR [158], 1972.

[146] K. Randle, D. B. Gayther, M. F. Murphy, and C. A. Uttley, The determination of the ^{92}Nb(n,n')$^{93\mathrm{m}}$Nb cross-section in the neutron energy range 1–6 MeV, Ann. Nucl. Energy **18**(12), 677–688 (1991).

[147] M. Wagner, H. Vonach, and R. C. Haight, Measurement of the activation cross section for the reaction ^{93}Nb(n,n')$^{93\mathrm{m}}$Nb in the neutron energy range 6–9 MeV, Ann. Nucl. Energy **20**(1), 1–7 (1993).

[148] M. M. H. Miah, B. Strohmaier, H. Vonach, W. Mannhart, and D.Schmidt, Cross section for the ^{103}Rh(n,n')$^{103\mathrm{m}}$Rh reaction in the energy range 5.7–12 MeV, Phys. Rev. C **54**, 222 (1996).

[149] A. Koning, private communication.

[150] Y.-W. Yu and D. G. Gardner, The (n,2n) reaction cross sections for Tu, Ir, Tl and Pb isotopes at 14.8 MeV neutron energy, Nucl. Phys. A **98**, 451 (1967).

[151] A. K. Hankla, R. W. Fink, and J. H. Hamilton, Neutron activation cross sections at 14.4 MeV for some naturally occurring heavy elements in the region 76≦Z≦82, Nucl. Phys. **A180**, 157–176 (1972).

[152] H. A. Tewes, A. A. Caretto, A. E. Miller, and D. R. Nethaway, Excitation functions of neutron-induced reactions, UCRL-6028-T, 1960.

[153] W. Dilg, H.Vonach, G. Winkler, and P. Hille, Nucl. Phys. A **118**, 9 (1968).

[154] T. B. Ryves, P. Kolkowski, and A. C. Hooley, Ho, Pb and Bi cross sections for 14.3 MeV neutrons, Ann. Nucl. Energy **17**(2), 107–111 (1990).

[155] H. Lu, W. Zhao, W. Yu, and X. Yuan, Activation cross section for the Pb-204(n,2n)Pb-203 reaction, Chin. J. Nucl. Phys. **12**(3), 269 (1990).

[156] A. A. Druzhinin, N. I. Ivanova, and A. A. Lbov, The (n,2n) reaction cross sections for Tu, Ir, Tl and Pb isotopes at 14.8 MeV neutron energy, Yad. Fiz. **14**, 682 (1971).

[157] R. Pepelnik, B.Andres, and B.M.Bahal, Measurements of 14 MeV neutron activation cross sections, Radiat.Eff. **92**, 211 (1986).

[158] EXFOR, Nuclear reaction data, EXFOR was accessed on line at `http://www.nndc.bnl.gov/nndc/exfor,www.nea.frorwww-nds.iaea.or.at/exfor`, 2001.

Acknowledgements

First of all I would like to thank Prof. Dr. Dr. h. c. S. M. Qaim for suggesting the subject of this thesis and for establishing the contacts with the IRMM Geel. He was my supervisor during the work and showed steady interest and provided constant guidance and encouragement.

I had the pleasure to work with Dr. Arjan Plompen, who guided me at the Van de Graaff laboratory at Geel, where most of the work was done. He was more than just a scientific adviser. Dank u wel, Arjan!

At Jülich Prof. H. H. Coenen provided all the facilities for work and I am grateful to him. I also would like to thank the Director of IRMM Prof. M. Grasserbauer and the unit heads of the Neutron Physics group at IRMM, Dr. H. Weigmann und Dr. Rulhusen.

I am very grateful to Mikael Hult and Timos Altzitzoglou of the Radionuclides Group at Geel for the ultra low-level measurements in HADES and the liquid Scintillation counting.

The help of Stefan Spellerberg with the irradiations and low level beta counting in Jülich is gratefully acknowledged. I would also like to thank K.-H. Linse for preparing the Tc samples and Dr. B. Scholten for some advice on γ-ray-spectrometry of Tc-sample

The discussions and the cooperation with Dr. D. L. Smith from ANL in some activation experiments during his two visits to Geel are gratefully acknowledged.

I would like to thank also Dr. Vlad Avrigeanu from Bukarest and Dr. Sandor Súdar from Debrecen for performing the nuclear model calculations. My special thanks to Dr. Súdar for the kind hospitality during my visit in Debrecen.

This work would not have been possible without the efforts of the accelerator crews in both Geel and Jülich. They always tried to provide the best possible conditions.

I wish to express my appreciation to all colleagues in Geel and Jülich, especially Andreas Fessler and my two italian room mates Roberto Puglisi and Claudia Goddio.

The financial support from the European Community through the award of a fellowship is gratefully acknowledged.

Meiner Frau und meiner Familie bin ich zu großem Dank verpflichtet. Ohne ihre Unterstützung und ihr Verständnis wäre diese Arbeit nicht möglich gewesen.

Erklärung

Ich versichere, daß ich die von mir vorgelegte Dissertation selbständig angefertigt, die benutzten Quellen und Hilfsmittel vollständig angegeben und die Stellen der Arbeit—einschließlich Tabellen, Karten und Abbildungen—, die anderen Werken im Wortlaut oder dem Sinn nach entnommen sind, in jedem Einzelfall als Entlehnung kenntlich gemacht habe; daß diese Dissertation noch keiner anderen Fakultät oder Universität zur Prüfung vorgelegen hat; daß sie—abgesehen von unten angegebenen Teilpublikationen—noch nicht veröffentlicht worden ist sowie, daß ich eine solche Veröffentlichung vor Abschluß des Promotionsverfahrens nicht vornehmen werde. Die Bestimmungen dieser Promotionsordnung sind mir bekannt. Die von mir vorgelegte Dissertation ist von Prof. Dr. Dr. h. c. S. M. Qaim betreut worden.

Pete Reime

Peter Reimer

Teilveröffentlichungen

P. Reimer, V. Avrigeanu, A. J. M. Plompen and S. M. Qaim, Reaction mechanisms of fast neutrons on ^{51}V below 21 MeV, Phys. Rev. C **65**, 014664 (2002).

P. Reimer, M. Hult, A. J. M. Plompen, P. N. Johnston and V. Avrigeanu and S. M. Qaim, Measurement of the ^{nat}Mo(n,x)^{94}Nb cross section using ultra low-level γ-ray spectrometry at HADES, accepted for publication in Nucl. Phys. A (2002).